

NOTE TO USERS

This reproduction is the best copy available.

UMI[®]

High Velocity Impact and Fragmentation of Reactive Metallic Particles

Thesis by
Stephen Janidlo

Department of Mechanical Engineering
McGill University
Montreal, Quebec, Canada

Submitted October 2004

A thesis submitted to McGill University in partial fulfillment of the
requirements of the degree of Master of Engineering

© Stephen Janidlo, 2004



Library and
Archives Canada

Bibliothèque et
Archives Canada

Published Heritage
Branch

Direction du
Patrimoine de l'édition

395 Wellington Street
Ottawa ON K1A 0N4
Canada

395, rue Wellington
Ottawa ON K1A 0N4
Canada

Your file *Votre référence*
ISBN: 0-494-06559-1
Our file *Notre référence*
ISBN: 0-494-06559-1

NOTICE:

The author has granted a non-exclusive license allowing Library and Archives Canada to reproduce, publish, archive, preserve, conserve, communicate to the public by telecommunication or on the Internet, loan, distribute and sell theses worldwide, for commercial or non-commercial purposes, in microform, paper, electronic and/or any other formats.

The author retains copyright ownership and moral rights in this thesis. Neither the thesis nor substantial extracts from it may be printed or otherwise reproduced without the author's permission.

AVIS:

L'auteur a accordé une licence non exclusive permettant à la Bibliothèque et Archives Canada de reproduire, publier, archiver, sauvegarder, conserver, transmettre au public par télécommunication ou par l'Internet, prêter, distribuer et vendre des thèses partout dans le monde, à des fins commerciales ou autres, sur support microforme, papier, électronique et/ou autres formats.

L'auteur conserve la propriété du droit d'auteur et des droits moraux qui protègent cette thèse. Ni la thèse ni des extraits substantiels de celle-ci ne doivent être imprimés ou autrement reproduits sans son autorisation.

In compliance with the Canadian Privacy Act some supporting forms may have been removed from this thesis.

Conformément à la loi canadienne sur la protection de la vie privée, quelques formulaires secondaires ont été enlevés de cette thèse.

While these forms may be included in the document page count, their removal does not represent any loss of content from the thesis.

Bien que ces formulaires aient inclus dans la pagination, il n'y aura aucun contenu manquant.


Canada

Abstract

Near-field blast effects for centrally initiated spherical heterogeneous explosive charges have been investigated experimentally. The charges consisted of a packed bed of reactive particles saturated with a liquid explosive. Once the charge was detonated, the particles accelerated to high velocities and impacted a rigid plate or cantilever gauges. The positive phase pressure impulse at the rigid plate surface and the cantilever bend angles were measured at various distances. Comparison of the results for large diameter Zirconium (millimetre-sized) and small diameter Aluminum particles (sub-micron) suggested that the impact and fragmentation of the former contributed to the overall loading of the blast wave within the near field. Single particle acceleration experiments concluded that the impacting of burning particles with a rigid structure resulted in fragmentation at all impact velocities. This suggested that the fragmentation mechanism was an efficient means by which to increase the overall energy release rate from the particle combustion process. Non-burning impact experiments were also conducted. Results implied the importance of shear banding and thermal stressing within the blunt impact and fragmentation mechanisms. Critical impact velocities for fragmentation with Zirconium, Titanium and Aluminum particles were obtained above which fragmentation of the metallic spheres occurred.

Résumé

La détonation d'explosif hétérogène initié sphériquement a été investiguée par expériences. Les charges étaient composées de particules réactives saturées d'un explosif liquide. Une fois la détonation initiée, les particules étaient accélérées à haute vitesse et ont impacté une plaque rigide ou des récepteurs leviers. L'impulsion positive était enregistrée et les déflexions angulaires des leviers étaient mesurées à plusieurs distances différentes. La comparaison des résultats pour des grosses particules (Zirconium) et des petites particules (Aluminium) suggérait que la fragmentation du Zirconium sur impact avec des surfaces rigides contribue à l'impulsion totale de la détonation. Des expériences qui accélèrent une seule particule ont été complétées. Les résultats ont prouvé que la fragmentation des particules brûlantes se manifestait à toutes les vitesses d'impact investiguées. Cela a suggéré que la fragmentation soit un moyen efficace d'augmenter l'énergie de combustion associée avec la détonation et la dispersion de particules brûlantes. Des expériences avec des particules non-brûlantes ont été effectuées. Les vitesses critiques pour la fragmentation de particule en Zirconium, Titane et Aluminium ont été déterminées.

Acknowledgements

I would first like to thank my thesis advisor, Dr. David Frost. His understanding during the difficult times, sense of humour during the good times and support at all times in between were essential to the completion of my thesis. His guidance and experience were valuable tools in my development as an engineer.

Dr. Martin Brouillette's openness to my work in the lab and his experience with light gas gun technology were instrumental in the timely and safe completion of my degree. I thank him and the University of Sherbrooke for their unbelievable cooperation.

Special thanks must be given to Jason Pryszlak, Jeff Levine and Chayawat Ornthanalai. They all worked along side me for years in the classroom, lab and tomato can. I can't imagine surviving a single summer out at DRES without their entertainment, encouragement and support. Gary Savard and John Boisvert were also incredibly generous with their time, insight and craftsmanship.

I would also like to thank Dr. Steve Murray and Dr. Fan Zhang of Defence Research and Development Canada in Suffield, Alberta, for their continual support of my work at McGill. They, and their entire technical staff at DRES, made all of my work possible. Their openness and expertise made field trials an eventful and fruitful experience.

NSERC's contributions have supported me throughout my undergraduate and graduate years. The completion of my degree would not have been possible without their generous funding.

Last, but definitely not least, I would like to thank my wife and parents. Their undying support has been an inspiration, and they have pulled me through some of the more difficult times. I love and thank you all very much.

Table of Contents

Abstract	i
Résumé	ii
Acknowledgements	iii
Table of Contents	iv
List of Figures and Tables	v
List of Notation	vii
1.0 Brief History of Pyrotechnics and Explosives	1
2.0 Introduction	7
3.0 Literature Review	10
3.1 Inert Particle Dispersal	10
3.2 Reactive Particle Dispersal	13
3.3 Spall Strength	17
<i>Theoretical Spall Strength</i>	18
<i>Spall in Ductile Solids</i>	21
<i>Other Factors Influencing Spall Strength</i>	24
3.4 Impact Tests	26
<i>Fragmentation Regions</i>	26
<i>Shock Coupled Energy</i>	28
<i>Energy Balanced Approach</i>	30
3.5 Metal Particle Combustion	33
<i>Volatile Metals</i>	34
<i>Non-Volatile Metals</i>	37
<i>Combustion of High Velocity Spheres</i>	39
4.0 Experimental Results	41
4.1 Explosive Dispersal Test Apparatus	41
4.2 Explosive Dispersal Test Results	44
4.3 Explosive Gun-Barrel Test Apparatus	51
4.4 Explosive Gun-Barrel Test Results	52
4.5 Light-gas Gun Apparatus	59
4.6 Light-gas Gun Test Results	62
<i>Steel Particle Results</i>	62
<i>Aluminum Particle Results</i>	63
<i>Titanium Particle Results</i>	66
<i>Zirconium Particle Results</i>	68
5.0 Discussion	76
6.0 Conclusions	82
7.0 References	84
Appendix A	I
A.I Complete Data Tables for Dispersal Experiments	II
APPENDIX B	VI
B.I Light-gas Gun Design Specifications	VII
B.II Light-gas Gun Diagnostics Specifications	VIII

List of Figures and Tables

- Fig. 1.0-1, Greek fire being used at sea, a drawing from the tenth century Byzantine manuscript.
- Fig. 2.0-1; Explosive dispersal of Zirconium metal particles.
- Fig. 3.1-1, Overpressure comparison of heterogeneous and homogeneous charges.
- Fig. 3.1-2, Effect of particle addition on blast trajectory.
- Fig. 3.2-1, Critical conditions for prompt ignition of Magnesium metal particles.
- Fig. 3.2-2, No ignition (left columns), delayed ignition (centre columns) and prompt ignition (right column) of Magnesium metal particles.
- Fig. 3.2-3, Scaling effects for heterogeneous explosives.
- Fig. 3.3-1, Cold compression-tension behaviour of condensed matter.
- Fig. 3.3-2, Ductile spall energy versus time.
- Fig. 3.4-1, Fragmentation regions for spherical impact.
- Fig. 3.4-2, Radiograph of cluster fragmentation of a steel sphere with a glass impact plate.
- Fig. 3.4-3, Sphere-plate impact with expected pressure profile.
- Fig. 3.4-4, Impact circle.
- Fig. 3.4-5, Expansion velocity vs. impact velocity for bumper plate trials.
- Fig. 3.5-1, Equilibrium product concentration and temperature for Mg combustion.
- Fig. 3.5-2, Equilibrium product concentration and temperature for Boron combustion.
- Fig. 3.5-3, Shock and stagnation temperatures vs. Mach number.
- Fig. 4.1-1, Spherical charge consisting of NM+10%TEA with centrally located booster of DM-12.
- Fig. 4.1-2, Pressure stands and reflective plate set-up.
- Fig. 4.1-3, Cantilever gauge set-up. Photo taken after a trial with resultant deflection caused by centrally initiated charge.
- Fig. 4.2-1, Peak overpressure profiles for centrally initiated charge compositions.
- Fig. 4.2-2, Positive phase pressure impulse profiles for centrally initiated charge compositions.
- Fig. 4.2-3, Impact craters on cantilever gauges for 1mm steel (Top) and 725 μ m Zr (Bottom) particles.
- Fig. 4.2-4, Cantilever trial data for centrally initiated charge compositions.
- Fig. 4.3-1, Side-view for explosive acceleration of a single Zirconium particle.
- Fig. 4.3-2, Top view of experimental set-up for single particle impact tests using gun-barrel design.
- Fig. 4.4-1, Stripping-off of outer liquid layer and subsequent fragmentation and ignition of inner solid kernel.
- Fig. 4.4-2, Secondary impact event on perpendicular plate 17 ms (top), 19 ms (middle) and 30 ms (bottom) after the initial impact event.
- Fig. 4.4-3, Impact of Zr 6.4 mm diameter particle at 160 m/s.
- Fig. 4.4-4, Impact of Zr 6.4 mm diameter particle at 400 m/s.
- Fig. 4.4-5, Impact of Zr 6.4 mm diameter particle at 650 m/s.
- Fig. 4.4-6, Impact of Zr 6.4 mm diameter particle at 2500 m/s.
- Fig. 4.5-1, Schematic of light-gas gun apparatus at the University of Sherbrooke.
- Fig. 4.5-2, Driver section of light-gas gun facility including pneumatic plunger.
- Fig. 4.5-3, Driven section exit with laser diagnostics for light-gas gun facility.
- Fig. 4.5-4, Entrance of test section using Plexiglas ® tube instead of Steel.
- Fig. 4.5-5, Impact plate for the test section with a Plexiglass ® tube instead of Steel.
- Fig. 4.5-6, Non-dimensional plot of theoretical exit velocity for various mass and initial pressure conditions.
- Fig. 4.6-1, Steel particles (right) and resulting craters from impact (left).
- Fig. 4.6-2, Aluminum particle's back surface (top, right), impacting surface (bottom right) and impact crater (left) at a velocity of 391 m/s.
- Fig. 4.6-3, Aluminum particle's back surface (top, right), impacting surface (bottom right) and impact crater (left) at a velocity of 455 m/s.
- Fig. 4.6-4, Aluminum particle's back surface (top, right), impacting surface (bottom right) and impact crater (left) at a velocity of 588 m/s.
- Fig. 4.6-5, Aluminum particle fused to its impact crater at a velocity of 800 m/s.
- Fig. 4.6-6, Aluminum particle fused to its impact crater at a velocity of 926 m/s.

- Fig. 4.6-7**, Titanium particle deformation (right) and resultant impact crater (left) at a velocity of 360 m/s.
- Fig. 4.6-8**, Titanium particle deformation (right) and resultant impact crater (left) at a velocity of 434 m/s.
- Fig. 4.6-9**, Titanium particle deformation through adiabatic shear banding (right) and resultant impact crater (left) at a velocity of 599 m/s.
- Fig. 4.6-10**, Titanium particle fragmentation (right) and resultant impact crater with fragments fused within the crater itself (left) at a velocity of 772 m/s.
- Fig. 4.6-11**, Cluster fragmentation (Top) and diffuse fragmentation (Bottom) of 6.35 mm diameter Zirconium particles.
- Fig. 4.6-12**, Shear banding discoloration at 502 m/s (Top) and 571 m/s (bottom).
- Fig. 4.6-13**, Deformation timescale calculation based on initial impact (left), and final deformation distance, R (right).
- Fig. 4.6-14**, Impact crater (left) and particle deformation (right) for Zr particle impact at 55 m/s.
- Fig. 4.6-15**, Impact crater (left) and particle deformation (right) for Zr particle impact at 300 m/s.
- Fig. 4.6-16**, Impact crater (left) and particle deformation (right) for Zr particle impact at 325 m/s.
- Fig. 4.6-17**, Impact crater (left) and particle deformation (right) for Zr particle impact at 413 m/s.
- Fig. 4.6-18**, Impact crater (left) and particle deformation (right) for Zr particle impact at 418 m/s.
- Fig. 4.6-19**, Impact crater (left) and particle deformation (right) for Zr particle impact at 467 m/s.
- Fig. 4.6-20**, Impact crater (left) and particle deformation (right) for Zr particle impact at 472 m/s.
- Fig. 4.6-21**, Impact crater (left) and particle deformation (right) for Zr particle impact at 478 m/s.
- Fig. 4.6-22**, Impact crater (left) and particle deformation (right) for Zr particle impact at 502 m/s.
- Fig. 4.6-23**, Impact crater (left) and particle deformation (right) for Zr particle impact at 545m/s.
- Fig. 4.6-24**, Impact crater (left) and particle deformation (right) for Zr particle impact at 551 m/s.
- Fig. 4.6-25**, Impact crater (left), inside surface of fragmented particle (top, right) and back surface of particle (bottom, right) for Zr particle impact at 571 m/s.
- Fig. 4.6-26**, Impact crater (left) and particle fragmentation (right) for Zr particle impact at 683 m/s.
- Fig. 4.6-27**, Impact crater (left) and particle fragmentation (right) for Zr particle impact at 755 m/s.
- Fig. 4.6-28**, Impact crater (left) and particle fragmentation (right) for Zr particle impact at 833 m/s.
- Fig. 4.6-29**, Impact crater (left) and particle fragmentation (right) for Zr particle impact at 862 m/s.
- Fig. 4.6-30**, Impact crater (left) and particle fragmentation (right) for Zr particle impact at 881 m/s.
- Fig. 4.6-31**, Impact crater (left) and particle fragmentation (right) for Zr particle impact at approximately 900 m/s.
- Fig. 4.6-32**, Impact crater (left) and particle fragmentation (right) for Zr particle impact of greater than 900 m/s.
- Fig. 5.0-1**, Shear banding in Titanium at 599m/s (left) and Zirconium at 551 m/s (middle). Lack of such bands in Aluminum at 588 m/s (right).

Table 3.3-1, Theoretical spall strength of selected materials.

Table 3.3-2, Material characteristics for ductile spall.

Table 3.4-1, Summary of bumper plate results.

Table 3.5-1, Thermodynamic data for various metals.

Table 3.5-2, Summary of ignition conditions.

Table 4.2-1, Average Zirconium experimental pressure and impulse data.

Table 4.2-2, Average ALEX experimental pressure and impulse data.

Table 4.2-3, Average Nitromethane pressure and impulse data.

Table 4.2-4, Average Steel experimental pressure and impulse data.

Table 4.2-5, Experimental cantilever data.

Table 4.6-1, Steel light-gas gun impact results

Table 4.6-2, Aluminum light-gas gun impact results

Table 4.6-3, Titanium light-gas gun impact results

Table 4.6-4, Zirconium light-gas gun impact results

Table 5.0-1, Comparison of impact test results.

List of Notation

A_c	non-dimensional form of shock coupling area	T	kinetic energy
a	final parameter for determining cold pressure	T_{bp}	boiling point temperature
a_c	critical radius of impacting sphere	T_0	stagnation temperature
B_0	bulk modulus	T_{shock}	normal shock temperature
c	speed of sound	T_{vol}	volatilization temperature
c_0	speed of sound	T_{rad}	radial expansion kinetic energy
C_p	heat capacity	T_c	non-dimensional form of critical time
d_{diff}	diffusion distance	T_{sc}	non-dimensional form of shock coupling time
E_0	chemical energy release that supports propagation	U	elastic energy density
E_s	energy input for spherical particle failure	U_c	cohesive energy
ΔH_{avail}	change in available enthalpy	U_{coh}	specific cohesive energy
$\Delta H_{vap-dissoc}$	heat of vaporization-dissociation	U_{nd}	non-dimensional form of impact velocity
H_{298}^0	heat of formation at the reference state	U_{shock}	shock velocity
$H_{T,vol}^0$	heat of formation at the given volatilization temperature	V_I	impact velocity
m	mass	W	dissipative energy
P	mean tension within the body	W_p	plasticity dissipative energy
P_c	cold pressure	Y	flow stress in simple tension
P_h	hugoniot pressure	Y_{st}	yield strength
P_0	peak overpressure	Z_c	fracture toughness
P_s	calculated spall strength	Z_S	acoustic impedance of the sphere
P_{th}	theoretical spall strength	Z_T	acoustic impedance of the target
p_c	shock pressure at critical fracture velocity	ϵ_c	critical void volume fraction
Q	energy release per unit mass of explosive	ϵ_r	dilation strain rate
Q_R	heat of reaction at the reference state	κ	thermal conductivity
R	given radius of impacting sphere	K	thermal diffusivity
R_0	characteristic length scale for a spherical charge	γ	specific heat ratio
s	nominal fragment size	v	specific volume
t	time	v_c	critical velocity at fracture
t_c	critical time of impacting sphere	$v_{expansion}$	expansion velocity in the radial direction
t_{sc}	shock coupling time	v_0	specific volume at zero pressure
		ρ	density
		α	loading time constant

1.0 Brief History of Pyrotechnics and Explosives

Science has long played an important role in all aspects of social development. From astronomy to chemistry, the evolution of the sciences has progressed hand in hand with most social changes. However, few of science's inventions have had such a strong impact on societies around the world as explosives. In fact, almost no other scientific invention can claim as long lasting a relationship with the dominance and progression of individual societies.

The defence of cities using launched fire-pots dates as far back as 900 BC on the Assyrian bas-reliefs. Burning tip arrows were used in the capture of Athens in the year 450 BC. Bonfires devastated the fortified walls of Plataea in 429 BC causing the rulers of the time to fall. Primitive versions of the modern cannon were also used in attacks on Delium in 424 BC. Numerous concoctions were developed from year to year, each designed to out-burn the previous. It was not until 463 AD that the advent of Greek-fire, the first real pyrotechnic material, would dominate the fields of war, defence and intimidation (G.I. Brown, 1998). In fact, the Byzantine empire would safely defend the city of Constantinople and its surroundings against invasion for nearly 800 years

using this pyrotechnic material. The figure at right clearly illustrates the primitive battle technique that proved effective for many generations.

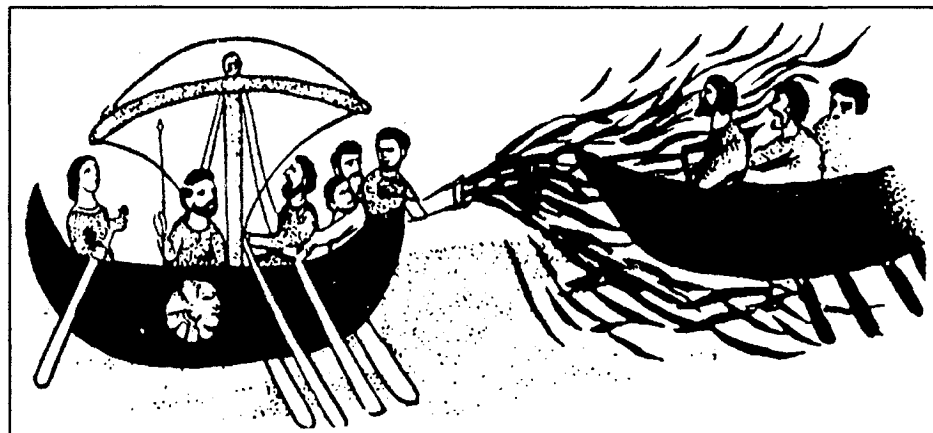


Fig. 1.0-1, Greek fire being used at sea, a drawing from the tenth century Byzantine manuscript. Corresponds to the figure on page 3 of G.I. Brown, 1998.

The actual composition of Greek-fire was so widely coveted that divulging the recipe was deemed an act of treason, sacrilegious and punishable by death. It is believed that the main ingredient was oil-rock, or naphtha, an oily residue commonly found near the Black sea and Caspian sea waters. A distilled variety of the residue would yield inflammable oil that could float on water and only be put out with sand, vinegar or urine. The obvious intimidation caused by such a devastating weapon allowed the region to thrive until the Turkish invasions of 1453. The empire fell because of a newly established weapon involving the use of the next revolutionary pyrotechnic material: gunpowder.

Gunpowder, or black powder as it is informally known, was believed to be invented by the Chinese nearly 400 years before the Turkish invasions. The first applications were for fireworks, small bombs and grenades. The Chinese state believed in the magic powder's potential so much that all production fell under government control by the year 1067. In fact, the state went so far as to make the sale of black powder illegal to all foreigners. Although the exact origins are still up for debate, the Franciscan friar Roger Bacon is accredited with the first written recipe for gunpowder. His concoction called for seven parts saltpetre, five parts young hazel wood and five parts sulphur. John Bate wrote that "Saltpetre is the Soule, Sulphur is the Life and Coales are the body" (Thucydides, 1954). The actual recipe for gunpowder remained relatively unchanged up until the 1700s. Past that date, the concentration of saltpetre increased to about 75%, with the remaining 25% equally split between sulphur and charcoal. Incredibly, the rise of gunpowder was relatively slow. The first primitive weapons were unreliable, dangerous, and grossly inaccurate. In fact, archers were more highly regarded for many centuries because of their speed of firing and accuracy. However, few kingdoms or empires doubted the potential of this black powder. Numerous advancements in both production and weapons technology made gunpowder the dominant pyrotechnic for hundreds of years.

The only thing that outshined the impact of gunpowder on the battlefield was its effect on civil engineering. The mining industry was introduced to gunpowder in the

early parts of the 17th century. Old-fashioned methods of hot-cold splitting and stone wedging were eclipsed by the high productivity of the powder. However, gunpowder was definitely a double-edged sword. Although mine productivity increased, employee safety was greatly reduced because of difficulties igniting the powder. In 1831, a Cornish miner by the name William Bickford invented the safety fuse by running gunpowder down the middle of a 12mm diameter rope. The new product swept throughout the industry and remained relatively unchanged until 1864. The debate continues as to whether or not gunpowder had a positive or negative effect on the mining industry. However, little debate exists as to the impact of gunpowder on canal building and railroad development. There is little doubt that the existence of society as it is today is indirectly linked to the canal building of the 17th century. The French were the first to use the modern powder to construct a canal 240 km long, with 100 locks, and a 165m tunnel linking the Mediterranean Sea to the Bay of Biscay. This unbelievable engineering exploit would have been impossible without the aid of gunpowder rock clearing. Canals spread throughout the civilizations of the globe, and along with the sprouting of railroads permitted the development of large cities away from major waterways. Gunpowder almost single-handedly allowed cities to grow larger than they ever had before. It marked the beginning of almost entirely urban societies.

With the incredible growth in popularity of gunpowder, it is not surprising that many claims of improved performance began to appear. Businessmen around the world were making unproven statements of having the “next best thing” and because of it many unqualified people began experimenting with explosives. Obviously the number of accidents increased dramatically, forcing the British Government to impose the Explosives Act of 1875. The act, which is still in place to today, controls all aspects of production, transportation, storage and use of any explosive material. American and Canadian governments (along with many others) have since implemented their own versions of the act.

However, not all the claims of improved performance were unfounded. Several advancements were made that not only made the explosives more powerful, but also safer to use. In fact, by the end of the 19th century, nitro-explosives almost completely eliminated the need for gunpowder. Eventually ANFO (Ammonium Nitrate Fuel Oil) explosives eclipsed all available pyrotechnic and explosive materials in both power and price. To this day, ANFO is a cheap and effective explosive. AN-based slurries and water-gel mixtures have overcome many of the original disadvantages making its use increasingly popular in the 21st century.

No discussion about explosives would be complete without at least a mention of nitroglycerine. The keystone to the development of this novel explosive was Fritz Haber's Nobel Prize winning method for making ammonia. The Germans, needing a more reliable way to produce explosives in times of war, quickly developed methods for producing ammonia and converting it into nitric acid. The method was so efficient that it was adopted around the world. However, it was not until 1864 that the true nitroglycerine era began. That date marks the invention of the detonator. Alfred Nobel successfully initiated a charge of pure nitroglycerine with a minute amount of gunpowder. Nitro-glycerine was the first real high-energy explosive, capable of generating overpressures over fifty times that of gunpowder in only microseconds. "It is the difference between being bumped into by a pedal cyclist or being knocked for six by an express train" (G.I. Brown, 1998). The difference is so dramatic between the high and low explosives that the term detonation first appeared to explain the overwhelming noise created with nitro-explosives (derived from *tonare*, to thunder in Latin).

Nobel's contribution to the world of explosives did not end with the detonator. He was also credited with the invention of "dynamite" (derived from *dynamis*, to power in Latin). Fearing further loss of life because of the unstable nature of nitro-glycerine, he began experimenting with ways of absorbing the explosive liquid into a paste or dough. He eventually succeeded with a mixture of three parts nitro-glycerine and one part kieselguhr (a soft, white, porous substance made from the skeletons of aquatic

plants). The resultant mixture was marginally less powerful, incredible easy to detonate and extremely safe to handle. In fact, the term dynamite is synonymous with the word explosive even to this day.

Advancements in the field of explosive materials led to the definition of two general forms: homogenous and heterogeneous explosives. Almost all modern forms of explosives can be categorized by one of these two general definitions. Homogeneous explosives are defined as ones with invariant composition. As seconded by the definition in the Random House College Dictionary (Revised Edition) homogenous means, “of the same kind or nature, having a common property throughout”. Heterogeneous explosives, on the other hand, may have inconsistent properties throughout their volumes. Within the context of this report, the heterogeneities are created by the saturation of liquid explosive within a spherically shaped packed bed of metallic particles.

The heterogeneous nature of an explosive and more specifically the addition of metal particles in a packed bed arrangement have some serious implications with regards to overall explosive performance. Firstly, adding metal particles will increase the energy density of the explosive mixture. The overall energy release will be augmented, increasing the work done by the expanding detonation products although the combustion of the particles occurs on a timescale that is much longer than the explosive itself. This phenomenon is particularly important for commercial explosives. However, the use of heterogeneous explosives is not without some drawbacks. For example, the detonation pressure, temperature and velocity are typically reduced due to the energy associated with the heating and acceleration of the added particles. The presence of heterogeneities within the explosive also adds to the complexity of the underlying detonation physics. One of the major issues still under investigation is the effect of the interaction of the particles with the blast wave. A lack of knowledge of the ignition and combustion timescales of the particles complicates the calculations that determine the total energy release of the detonation. The momentum flux of the gas and particles and their respective effects on the impulsive

loading of nearby structures is another mechanism that has yet to be properly explored.

Clearly there are many fundamental questions that require further scientific study in order to characterize the detonation physics of heterogeneous explosives. This report is an attempt at bridging the gap between the observed physical phenomena of a heterogeneous explosion and the understanding of its underlying mechanisms. Issues related to the detonation propagation in the multiphase mixture will not be addressed. Rather, the present study concentrates on the particles accelerated by the expanding combustion products and their effects on nearby structures.

2.0 Introduction

Zhang, *et al.* (2001) devised a simple experimental set-up for the detonation of heterogeneous explosives. The spherical charges consisted of solid inert particles placed in a packed bed arrangement saturated with liquid explosive. Upon detonation of the liquid explosive, the inert particles accelerated to speeds of well over 1 km/s. The acceleration and impact of these high-speed particles generated significant loading on nearby obstacles. Further experimentation showed that the near-field impulse applied to an obstacle was primarily influenced by the momentum-flux provided by the particles (Frost, *et al.* 2001). This naturally led to experimentation with reactive particles with a similar charge configuration in order to study the potential enhancement of blast characteristics caused by the energy release associated with the metal particle combustion process. The figure below is a clear example of the reactive nature of Zirconium metal particles.



Fig. 2.0-1, Explosive dispersal of Zirconium metal particles.

It is important to note that in the previously mentioned experiments with inert particles, the particle velocities were insufficient to cause fragmentation upon impact with solid structures. The question was raised whether or not explosively dispersed

reactive particles (instead of inert particles) with relatively large diameters could fragment upon impact. If partially molten projectiles did occur, this would result in a significant increase in surface area. A larger reactive surface area would yield a substantially greater energy release rate, which could lead to an increased loading on

nearby structures. This scenario is based on the assumptions that particle fragmentation occurs and that the energy release process occurs rapidly enough to influence the local thermodynamic conditions. The validation of these assumptions is the motivation for the present work and the objective of the recently performed experiments.

Frost, *et al.* (2002, 2003a) have thoroughly studied the explosive dispersal of inert and reactive particles. Particle fragmentation has also been studied at length over the past several decades. Many of these studies involved the hypervelocity impact of particles with either bumper plates or semi-infinite obstacles, particularly in the context of the impact of micrometeorites with space structures. Relatively little literature exists attempting to shed light on the impact fragmentation of reactive and burning metallic particles.

Experimental trials in both particle dispersion and impact fragmentation have been performed in order to mesh the understanding developed in each field over the years. An attempt to explain the associated enhancement of loading effects on near-field structures will also be made. Three independent sets of trials have been performed in order to evaluate the hypothesis proposed earlier. First, a set of particle dispersal trials was performed over several summers. Second, a series of single reactive sphere tests were conducted that accelerated a particle explosively. Third, a light-gas gun facility was utilized to determine the fragmentation characteristics of the particles themselves.

The field trials were carried out at the experimental test range at DRDC-Suffield in Alberta, Canada. The trials were a collaborative effort typically involving 3 or 4 students and staff from McGill University as well as technical staff from DRDC-Suffield. The contributions of the author of the present report are summarized in the following. I participated in the field trials during the summers of 2000-03. In July 2003, I worked with Jason Prysxlak on the design, construction and initial testing of the explosively driven particle accelerator. Following that, I modified the Light Gas

Gun located at the University of Sherbrooke by adding a test section and rebuilding the gas handling system. I then carried out the particle impact tests with the aid of technical staff from the University and Dr. Martin Brouillette.

The following section is a brief review of pertinent literature. It begins with a summary of inert and reactive particle dispersal experiments. The concept of spall strength and its importance with regards to impact fragmentation is then introduced. An overview of previous experiments involving impact testing is then presented, followed by a brief description of metal particle combustion.

After the literature review, an outline of the three experimental procedures is given. The results and discussion are then presented. Conclusions are made with all background information available in the appendices at end of this report.

3.0 Literature Review

3.1 Inert Particle Dispersal

Kurbangalina (1969) and Lee, *et al.* (1995a, 1995b) have experimentally studied the detonation characteristics of heterogeneous explosives consisting of a packed bed of spherical particles saturated with liquid explosive. They were able to determine the detonation velocities and critical diameters for propagation as functions of the liquid explosive sensitivity and particle diameter. They hypothesized a mechanism for the propagation of the detonation wave within the charge itself. Zhang, *et al.* (2001) used the same explosive mixture to systematically study the dynamics of the subsequent particle dispersion.

When a packed bed charge of inert spherical particles is detonated, a detonation wave propagates through the packed bed compacting the spheres. A large pressure gradient is immediately generated at the outer edge of the packed bed. This steep pressure gradient causes a large initial acceleration of the particles. When the wave reaches the outer edge of the charge, a blast wave is transmitted into the air. A subsequent rarefaction wave is reflected at the charge surface and the expanding detonation products drive the particles outwards. A large velocity difference between the expanding products and the particles themselves creates an aerodynamic drag force that accelerates the particles even faster. In fact, Zhang, *et al.* (2001) showed that the particles were accelerated to velocities between 1-2 km/s within the scale of only a couple charge diameters. Lanovets, *et al.* (1991) performed numerical simulations of a similar configuration and determined that the particles can in fact race ahead of the explosion products and penetrate the shock front. Once in front of the initial blast wave, the particles decelerate because of the aerodynamic drag. Eventually, the shock front may catch up to the particles and overtake them in the far-field.

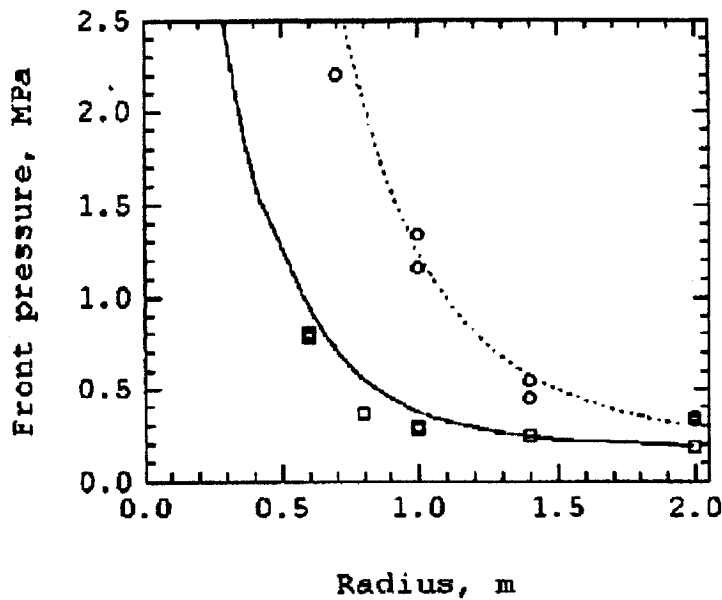


Fig. 3.1-1, Overpressure comparison of heterogeneous (□) and homogeneous (○) charges at varying distances. Corresponds to fig. 4 of Zhang, *et al.*, 2001.

Frost, *et al.* (2001) concluded that the exchange of momentum and energy between the surrounding flow field and the particles themselves actually changed the rate of decay of the blast wave when compared with homogeneous explosions of a similar configuration.

The figure at left demonstrates the previous statement. In tests looking

at the overall effect on the far-field pressure and impulse (i.e., time integral of pressure), it was determined that both could be augmented by the shock front penetration of particles. They determined that in the near-field, when comparing homogeneous and heterogeneous charges with the same mass of explosive, the heterogeneous charge developed significantly higher impulses. Although the peak overpressures were lower because of the energy losses associated with the acceleration of the particles, the particle momentum flux was up to 4 times greater than that for the results involving the gas alone. In fact, some analysis of the experimental results showed that for the heterogeneous charges the particle impacts contributed 70% of the total impulse applied to cantilever gauges.

Several important factors can affect the ability of the high velocity particles to overtake the shock front. The first and most obvious factor is that of charge geometry. As explained by Zhang, *et al.* (2001), a charge generating a planar shock front will never be overtaken by accelerated particles. This is explained by the relatively slow decay of the front caused by the Taylor expansion. For charge configurations yielding

curved shock fronts, over-taking of the blast wave by the particles is possible for certain ranges of particle mass and inertia. As explained in any literature describing shock wave fundamentals, the frontal curvature of a non-planar shock wave will cause the rapid deceleration of the front itself.

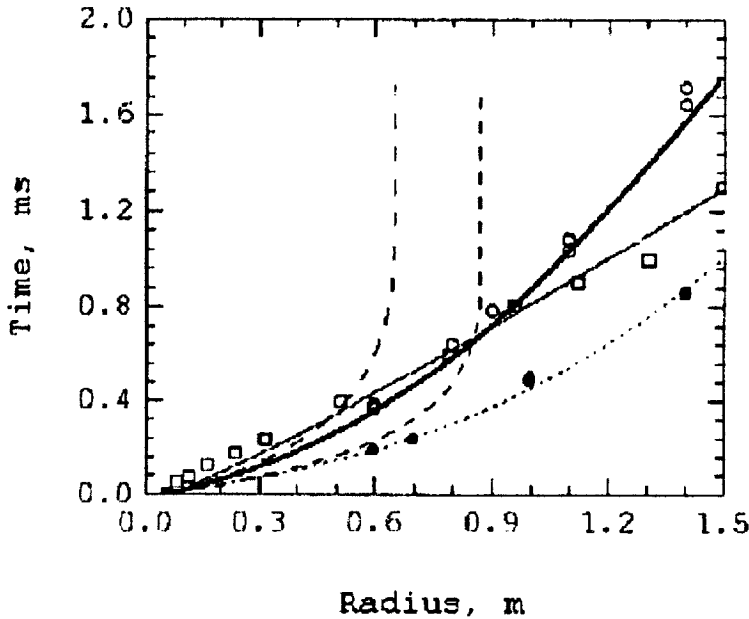


Fig. 3.1-2, Effect of Particle Addition on Blast Trajectory. ● Experimental Nitromethane (NM), ○ Experimental NM/Fe, □ Experimental cloud front, - - Explosion product front NM/Fe, · · · Explosion product front NM. Corresponds to fig. 5 from Zhang, *et al.*, 2001.

The next factor influencing the potential overtaking of the shock front is the inertia of the particles that are being dispersed. As determined previously (Zhang, *et al.*, 2001), the initial acceleration of inert particles is influenced most directly by the pressure gradient in the multiphase flow behind the shock front.

Following the initial acceleration, subsequent acceleration and/or deceleration of the particles is linked to the drag associated with velocity differences between the two phases. It is important to note that the pressure gradient of the multiphase flow is independent of the particle diameter. The time scale of the momentum relaxation controls the drag, which is proportional to the square of the particle diameter (This depends on the particle Reynolds number and the flow regime, e.g., Stokes flow). This means that for larger particle diameters, the pressure gradient is the dominant driving force yielding almost constant particle velocities. As the diameter is reduced, the drag force becomes a much more significant contributor to the particles' overall velocity. Again as explained in Zhang, *et al.* (2001), the reduction in particle diameter results in an overall reduction of the momentum relaxation time scale. As the particles

cross the shock front, the aerodynamic drag reduces their relative velocity, effectively pulling them back towards the shock front. Hence, if the diameter is reduced too much, the momentum relaxation time scale is such that the particles will equilibrate with the velocity of the expanding detonation products. This means that the particles will never penetrate the decelerating shock front. In other words, for small particles the inertial effects of the initial acceleration would be insufficient to allow the relative drag forces to be overcome. The particles would never reach a velocity greater than that of the expanding detonation products because the momentum relaxation time scale would be too short.

The solid mass fraction is also an important parameter in particle dispersal experiments. If the particle density is reduced (hence reducing the solid mass fraction), the overall loss of momentum is reduced in the energy transfer from the expanding detonation products to the particles themselves. This translates into having more energy expanding the detonation products with fewer particles to accelerate. This increase in driving impulse is predicted to have a significant effect on reducing the total overtaking distance for particles to penetrate the shock front (Zhang, *et al.*, 2001). The solid mass fraction effect has been studied extensively in the previous computational work. However, it has remained relatively untouched in the experimental world because of difficulties in developing appropriate explosive charges that conveniently vary the mass fraction of the inert particles.

3.2 Reactive Particle Dispersal

The dispersal mechanism of reactive particles is identical to that described previously for inert particles. It involves the development of a large pressure gradient and the subsequent expansion of the detonation products. The particles are accelerated rapidly in the near-field and depending on their inertial characteristics may or may not overtake the shock front.

The biggest difference when comparing reactive and inert particles is the potential for heat release associated with the combustion of the metal particles within and/or ahead of the detonation products. This release of even greater amounts of energy can further augment the overpressures and impulses associated with the blast wave. The penetration of the burning particles ahead of the shock front can also effectively preheat the surrounding air and minimize the decay of the decelerating blast. Filler (1976, 1985) observed in his tests with reactive casings that the shock attenuation was slowed because of the interaction between the reactive casing fragments and the flow field.

As described previously in the section on inert particle dispersal, work has been done to determine the detonation velocities and critical diameters of packed bed heterogeneous charges. As described by Frost, *et al.* (2002), variation of particle size within the packed bed configuration is a compromise between the desensitization of the explosive by the particles themselves and the sensitizing effect caused by hot-spot generation from the shock wave and particle interaction. These factors play crucial roles in the overall determination of the critical diameter and detonation velocity for specific configurations of both inert and reactive particles.

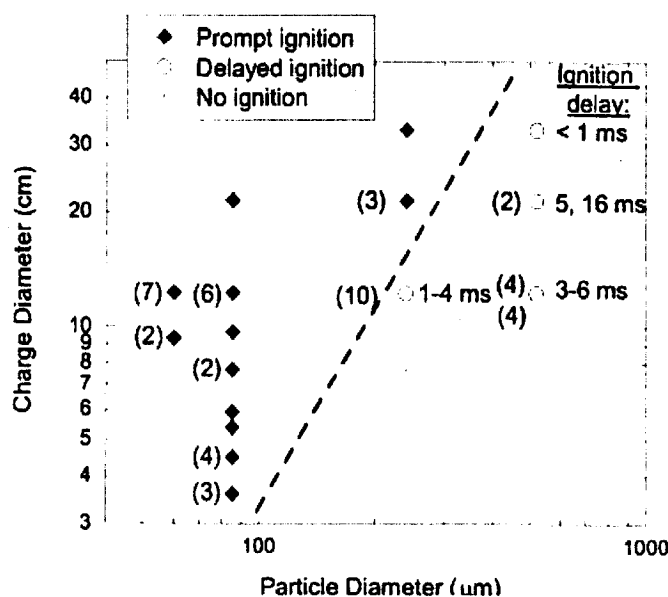


Fig. 3.2-1, Critical condition for prompt ignition of Magnesium metal particles. Corresponds to fig. 4 of Frost, *et al.*, 2002.

The reactive nature of some metal particles lends itself to a different definition of critical diameter. The normal definition for the critical diameter is that of the diameter below which the propagation of a detonation wave is not possible. However, with reactive particles a second critical diameter can be

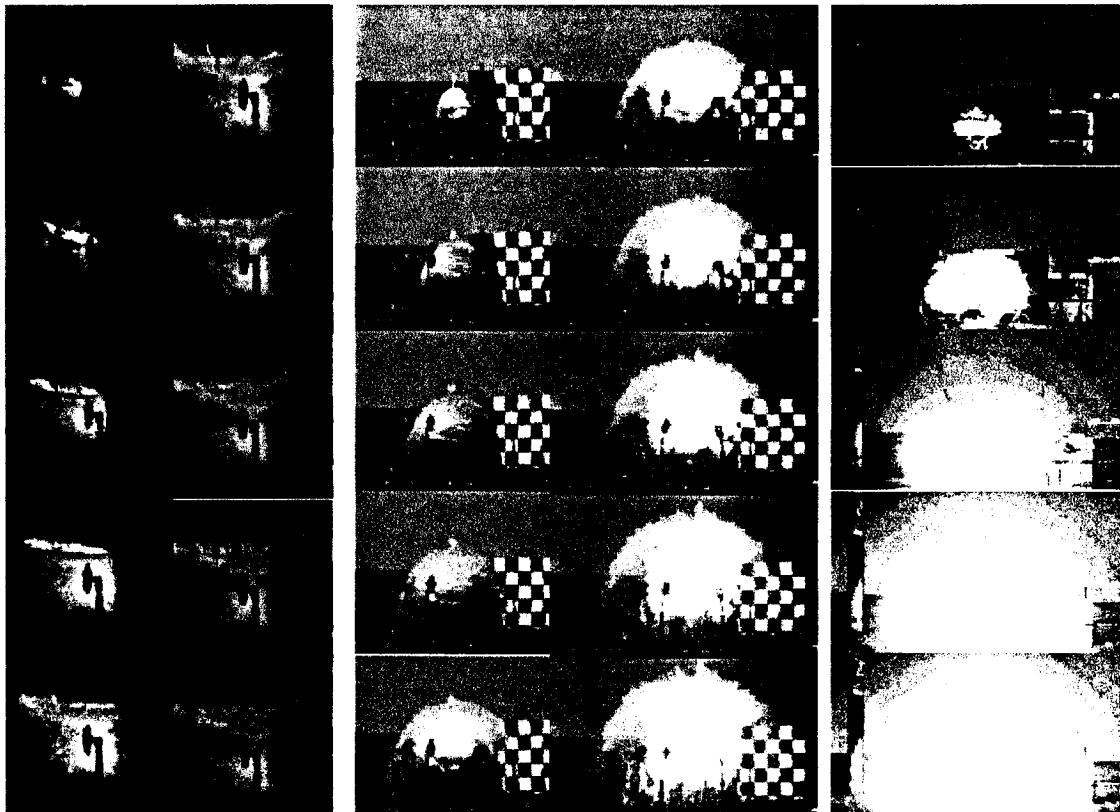


Fig. 3.2-2, No ignition (left columns), delayed ignition (centre columns) and prompt ignition (right column) of Magnesium metal particles. Time between frames is approximately 0.5 ms. Corresponds to fig. 2 of Frost , *et al.*, 2003a.

established below which the prompt ignition of the particles does not take place. The term “prompt” here is defined as a combustion energy release within a timescale that allows for the augmentation of the blast wave intensity. Frost, *et al.* (2002) performed numerous lab and field experiments on magnesium particles of varying diameter placed in a packed bed configuration of varying charge diameter. Figures 3.2-1 and 3.2-2 visually explain the above description of a second critical diameter for prompt ignition. One should notice the presence of three different regimes. The first is described previously as the prompt ignition of the particles. The second regime was that of delayed ignition where the particles burned but on a delayed timescale that did not allow for the augmentation of the blast wave intensity. A third regime was also observed within which the detonation itself succeeded but the reactive particles did not ignite.

The simplest way to compare the relative strength of a blast wave is by plotting the shock front trajectory on a time-distance graph. Experimentation has shown that the

trajectory is in fact the least sensitive parameter characterizing a blast (Frost, *et al.*, 2003a). Scaling of the blast wave parameters based on the energy value is commonly practiced with homogeneous explosives. The scaling procedure allows for the direct comparison of charges with similar composition but with varying mass and different energy release characteristics. The characteristic length scale of the explosion is labelled as R_0 and it is proportional to the cube root of the total energy release within the explosive blast. The single step energy release model is only valid when the propagation of the blast wave is of significantly longer duration than the time required for complete energy release of the explosion. Although heterogeneous explosives will not react in a single step manner because of the variation and number of reactive particles, it is still useful to develop this type of model. The model will allow for the comparison of the heterogeneous charge with the expected blast wave parameters for ideal behaviour. Bach and Lee (1970) defined R_0 , for spherical blast waves, as follows:

$$R_0 = \left(\frac{E_0}{4P_0\pi\gamma} \right)^{1/3} \quad (3.2-1)$$

E_0 is defined as the chemical energy release that supports the propagation of the blast wave and is given by the mass (m) of explosive material times the energy released per unit mass of explosive (Q). As mentioned previously in this section, the amount of energy released is directly proportional to the degree of reaction of the explosive. In other words, if prompt ignition is observed, then it is reasonable to assume that the complete metal particle mass and liquid explosive mass and their respective energies have contributed to the overall blast propagation. However, if delayed or no ignition of the particles is observed during the dispersal process, then only the energy release associated with the liquid explosive should be included. Frost, *et al* (2003a) noticed that even with the scaling of blast wave parameters, the homogeneous and heterogeneous trajectories did not collapse into a single curve. This divergence in results was explained by the complex exchange of mass, momentum and energy between the dispersing particles and the gas of the flow field. They also noticed that

the delayed-ignition mechanism produced significant scatter with regards to the scaling of the blast wave trajectories. This again points to the overly simplistic nature assumed in the characteristic scaling length R_0 that only required a single energy

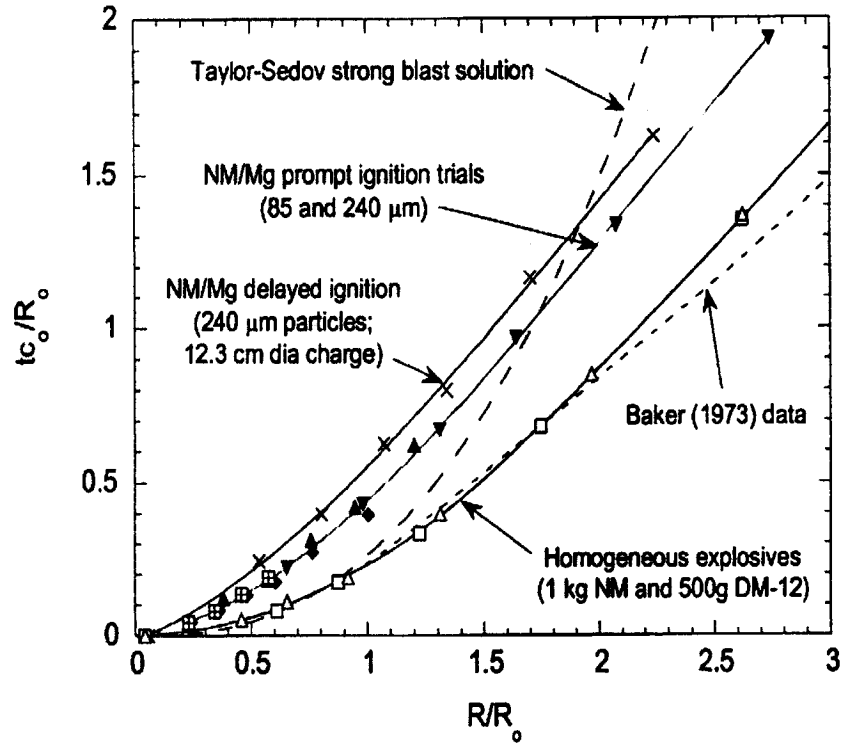


Fig. 3.2-3, Scaling effects for heterogeneous explosives. Corresponds to fig. 6 of Frost, *et al.*, 2003a.

parameter. They also concluded that the more sensitive blast parameters (like peak overpressure and positive phase pressure impulse) did not scale well in the near-field ($R/R_0 \leq 1$) but showed satisfactory convergence in the far-field ($R/R_0 \geq 1$). The complex nature of the dispersal process is again attributed to scatter in the scaling results. Figure 3.2-3 above is a graphical summary of the experimental results (Frost, *et al.*, 2003a) and the theoretical calculations developed by Baker (1973).

3.3 Spall Strength

Spall is defined as the internal failure of condensed matter induced by the transient states of tensile stress within the body. For particle impacts, these states of tensile stress are generated by the interaction of stress waves within the body causing dynamic failure or fragmentation.

Deformation within a spalling body can be elastic or plastic depending on the spall strength, yield strength and deformation path. Plastic deformation from compression is therefore an important factor in determining fragmentation properties because it can seriously alter the material properties of the impacting object (Shockey, *et al.*, 1973; Meyer and Aimone, 1983). Furthermore, the entire spalling process is intrinsically unstable because of the presence of micro-cracks and inclusions within the material itself. The static properties of the material are not adequate with regards to predicting dynamic behaviour. In fact, it has been shown that a material can withstand stresses well beyond those of yield because of the kinetics and inertia of dynamic nucleation and growth of cracks during spalling (Curran, *et al.*, 1977 and 1982; Davison and Graham, 1979; Meyer and Aimone, 1983).

Although dynamic spall events are dependent on the pre-existing or evolving microstructure of a material, the complete history of that material is not essential. Normally one is trying to determine the dynamic spall strength, time to failure and nominal fragment size. These primitive spall properties appear to be less sensitive to the materials microstructure and more intimately linked to the balance of the driving energy of the transient wave loading and a continuum measure of the fracture dissipation through fracture toughness, surface tension, flow stress or viscosity. (Englman, *et al.*, 1987; Glenn and Chudnovsky, 1896; Grady, 1982 and 1988; Grady and Kipp, 1985)

Theoretical Spall Strength

The theoretical spall strength is defined as the maximum or upper bound of spall strength for a condensed material. The maximum value is an important property for impact fragmentation because the highly dynamic mechanisms involved with rapid tensile loading actually yield values close to the upper limit of spall strength. Throughout the past half-century, several theories have been presented as ways to approximate the maximum spall strength. Orowan (1949) developed a strategy for predicting spall strength based on the intermolecular potential of a solid. His work was followed by that of Lawn and Wilshaw (1975) that used a sinusoidal

representation of the cohesive force to obtain the expression as follows, where B_0 is the bulk modulus of the material:

$$P_{th} \approx \frac{B_0}{\pi} \quad (3.3-1)$$

Several two-parameter models were then developed, followed by three-parameter models that provided reasonable depictions of the thermodynamic behaviour of solids. Examples of the latter are the Morse potential, exponential-six potential and a metallic model proposed by Rose, Guinea and Ferrante (1984). The three-parameter model, although slightly more complex in nature, is intuitively more satisfying than previous models because of the inherent energy balance required in its solution. As explained by Grady (1988), to derive an expression for the theoretical spall strength one can use the Morse potential model of the form:

$$U_c(v) = U_{coh} \left[\exp\left(\frac{-2(v-v_0)}{a}\right) - 2 \exp\left(\frac{-(v-v_0)}{a}\right) \right] \quad (3.3-2)$$

where $U_c(v)$ is the cohesive energy, U_{coh} is the specific cohesive energy, and v_0 is the specific volume at zero pressure. The final parameter “a” is constrained by requiring

$$v \frac{d^2U}{dv^2} = B_0 \text{ at } v=v_0, \quad (3.3-3)$$

which yields that

$$a = \sqrt{\frac{2v_0 U_{coh}}{B_0}} \quad (3.3-4)$$

Then using Equations (3.3-2, 3.3-3, 3.3-4) it follows directly that the cold pressure, which is defined as the derivative of the cohesive energy within the material, is given as:

$$P_c(v) = -\frac{dU(v)}{dv} = -\frac{2U_{coh}}{a} \left[\exp\left(\frac{-2(v-v_0)}{a}\right) - 2 \exp\left(\frac{-(v-v_0)}{a}\right) \right] \quad (3.3-5)$$

The theoretical spall strength is then represented by the minimum of Equation (3.3-5) from the previous page. The minimum value is obviously determined by the zero slope point on the cold compression-tension curve in Figure 3.3-1 at right or where the derivative of the previous equation is zero. Equation (3.3-6) below displays the expression for the derivative and Equation (3.3-7) represents the final solution for the theoretical spall strength of a condensed material:

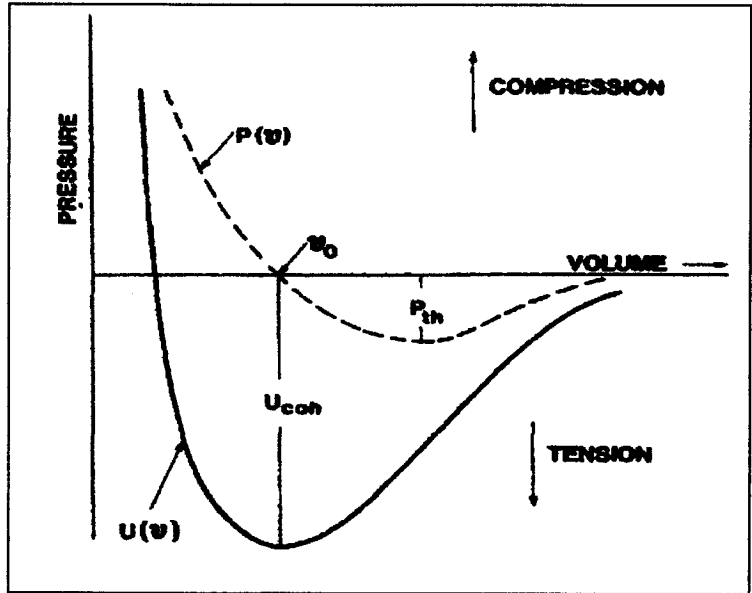


Fig. 3.3-1, Cold compression-tension behaviour of condensed matter. Corresponds to fig. 1 in Grady, 1988.

$$\frac{dP(v)}{dv} = -\frac{2U_{coh}}{a^2} \left[2 \exp\left(\frac{-2(v-v_0)}{a}\right) - 2 \exp\left(\frac{-(v-v_0)}{a}\right) \right] = 0 \quad (3.3-6)$$

$$P_{th} = \sqrt{\frac{U_{coh} B_0}{8v_0}} \quad (3.3-7)$$

Values calculated using this technique are displayed in Table 3.3-1 on the following page. The original source of the data can also be found in Grady's (1988) summary article on the spall strength of condensed matter.

Table 3.3-1, Theoretical spall strength of selected materials. Corresponds to table 1 of Grady, 1988.

Metal	B_0 (GPa)	ρ (kg m ⁻³)	U_{sp} (MJ kg ⁻¹)	P_{sp} (GPa)
Aluminum	72.2	2710	11.9	17.1
Beryllium	100	1820	35.7	28.5
Copper	137	8930	5.32	25.8
Titanium	105	4510	9.78	24.1
Iron	168	7870	7.41	35.0
Tantalum	200	16660	4.31	42.4
Tungsten	323	19250	4.55	59.5
Uranium	98.7	19050	2.19	22.7
Mercury	38.2	13530	0.33	4.6
Tin	111	7300	2.53	16.0

Spall in Ductile Solids

Calculated results for brittle material spall strength are adequately accurate because of the assumption that surface energy is characterized by the fracture toughness. The mechanism of crack link-up for an internal failure process seems reasonable. Ductile materials, however, react in a very different manner. The failure mechanism depends more intimately on the nucleation, growth and coalescence of holes. The energy methods developed for brittle spall still apply to ductile materials, with very simple yet essential changes. Firstly, the same uniform expansion of the mass element δM with a constant strain rate is assumed. This means that the mass element is submitted to a tensile force as given by Equation (3.3-8) and the horizon condition of Equation (3.3-9) still applies appropriately. Furthermore, the elastic and kinetic energies will continue to increase as the expansion occurs, allowing for the same application of Equations (3.3-10, 3.3-11)

$$P = \rho c_0^2 \epsilon_r \quad (3.3-8)$$

$$s \leq 2c_0 t \quad (3.3-9)$$

$$T = \rho s^2 \varepsilon_r^2 / 120 \quad (3.3-10)$$

$$U = \frac{1}{2} \frac{P^2}{\rho c_0^2} \quad (3.3-11)$$

The most significant difference in the spalling behaviour of ductile materials is the mechanisms of energy dissipation. For brittle materials, the dissipation was believed to be driven by the generation of surface energy within the cracks. However, for ductile materials, the surface energy component of the dissipation process can be neglected. The plastic deformation of the material during void growth is the main dissipative mechanism (Orowan, 1970). Work by Gurson (1977), as well as Tvergaard and Needleman (1984) established that stable void growth occurs until a critical void volume fraction (ε_c) is attained. Other independent experiments by Brown and Embury (1973), and Goods and Brown (1979) demonstrated that the critical void volume fraction was attained when the void diameter approached the void spacing. From all the available literature, it appears that a reasonable approximation of the critical void volume fraction is relatively constant at 0.15. Therefore the dissipative energy, W , can be approximated as follows, where Y is the flow stress in simple tension and is assumed to be independent of rate, temperature and scale.

$$W = Y \varepsilon_c \quad (3.3-12)$$

The previous expression is interesting in that it demonstrates the independence of fracture energy from fragment size for ductile materials. This means that the plastic deformation work is completely independent of the number of voids or void spacing. Now, re-establishing the energy condition for the ductile spall process one would obtain the following expression:

$$0.5P^2 / \rho c_0^2 + \rho s^2 \epsilon_r^2 \geq Y \epsilon_c \quad (3.3-13)$$

Obviously from the previous equation, the sum of the kinetic energy and elastic energy must at least equal the ductile fracture energy for spall to initiate. If the minimum criterion is attained, it is referred to as the “Energy-Limited Spall” and if it occurs beyond that point it is labelled “Flaw-Limited Spall”. See Figure

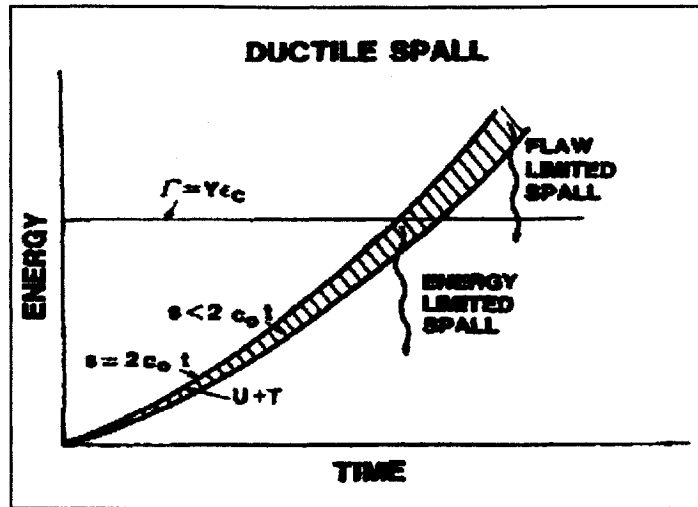


Fig. 3.3-2, Ductile spall energy versus Time. Corresponds to fig. 6 of Grady, 1988.

3.3-2 for a visual representation of the inequalities in Equations (3.3-8, 3.3-9, 3.3-13). Similar to brittle materials, if the smaller kinetic energy term in Equation (3.3-13) is ignored, then relations for the spall strength, fracture time and nominal fracture size can be expressed. They are written below as Equations (3.3-14, 3.3-15, 3.3-16), respectively. Table 3.3-3 also represents a quick summary of available experimental and theoretical data for a sampling of materials (Grady, 1988).

$$P_s = (2\rho c_0^2 Y \epsilon_c)^{1/2} \quad (3.3-14)$$

$$t_s = (2Y \epsilon_c)^{1/2} / (\rho c_0^2 \epsilon_r^2)^{1/2} \quad (3.3-15)$$

$$s = (8Y \epsilon_c)^{1/2} / (\rho \epsilon_r^2) \quad (3.3-16)$$

Table 3.3-2, Material characteristics for ductile spall. Corresponds to table 3 of Grady, 1988.

Material	B_0 (GPa)	Y (GPa)	P_c (exp. GPa)	P_c (thy. GPa)
Al (soft)	72.2	0.015-0.03	0.5-1.1	0.57-0.81
Copper	137	0.025	1.0-2.5	1.0
Tantalum	200	0.7	4.4-6.8	6.5
Tin	111	0.05-0.12	0.6-0.8	1.3-2.0
Titanium	105	0.8-0.9	4.1-5.0	5.0-5.3

Other Factors Influencing Spall Strength

The previous description of the spall process is an extremely simplified model of the actual process. Several assumptions need to be made in order to clearly demonstrate the underlying physics of the fracture and fragmentation of impacting particles. That being said, it is worthwhile to explore the various factors that may contribute to the variations between theoretical and experimental spall strengths.

The first complication to the spall process is the underlying assumption of constant strain-rate and its effect on other material properties. Obviously the effect of strain rate would be amplified if other material properties like fracture toughness (K_{Ic}) and yield strength (Y_{st}) were rate dependent. It has been shown that typically K_{Ic} decreases slowly while Y_{st} increases with strain rate. As an initial run-through for the problem at hand the constant properties assumption is acceptable, but a further refinement of the model would be required if more detailed results were necessary. Furthermore, Follensbee (1984) proposed the possibility of a transition region from thermally-activated to phonon-drag controlled plastic flow. He concluded that a linear dependence of the flow stress with strain rate would be adequate for the modeling of materials within the appropriate transitional region. Obviously this phenomenon would greatly influence the modelling of the impact spall process.

The temperature effects of spall strength are similar to those of strain rate in the sense that they ultimately affect other material properties. Curry and Knot (1979) demonstrated that K_c increased with temperature and Y_{st} decreased. Beyer and Ring (1972) showed that in normal liquids, viscosity decreased with temperature and Allen (1972) explained that the surface energy was relatively insensitive to temperature then decreased rapidly when a critical value was attained. Obviously the temperature dependence cannot be understated in impact processes because of the entropy production from the compressive shock wave preceding spall (Grady, 1988).

Some of the more important factors that complicate the spall process in high velocity impact situations are the pre-compression effects. As the material impacts, compressive stress waves are generated within the body. If the compression waves are strong enough, plastic deformation within the material can alter the bodies' properties prior to the development of the tensile state. Murr (1981) explained that the compression waves could alter the inherent microstructure of the material itself. Work by Powers, *et al.* (1997) discussed the potential ignition of energetic materials by the formation of adiabatic shear bands. They described the shear banding process as an increased strain rate near local discontinuities. Increased straining into the plastic range resulted in strain hardening of the material. However, the localization of that high strain rate also resulted in the plastic heating of the material. The thermal heating phenomenon could be significant because the plastic deformation occurred over a much shorter timescale than that of heat dissipation through conduction. In fact, their work predicted temperatures of over 5000K within some of the shear bands. Furthermore, the localized heating could thermally soften the material. If the local temperature effects dominated those of strain hardening, an overall decrease in material strength was observed (Wright, 2002).

Obviously pre-compression can greatly affect the overall spall strength of the material depending on the strength of the initial compression waves. Thus the process through which the material achieves the spalling tensile state is incredibly important for the selection of appropriate material property data.

The microstructure of the material is also inherently important in the prediction of spalling behaviour. However, it is left to the reader to review the most relevant work on the topic produced by Shockey, *et al.* (1973), Meyer and Aimone (1983), Christy and Pak (1986), and Brandon, *et al.* (1984). Also, a quick review of the flaw-limited spall process is discussed by Grady (1988).

3.4 Impact Tests

Impact testing in the scientific community began as early as the 1950s. With space travel at the forefront of most cutting edge research, the problems associated with high velocity impacts became important. Meteors, hurling through outer space at literally astronomical velocities, would undoubtedly impact the exterior skin of satellites and spacecraft. Therefore, a better understanding of the impacting regimes and phenomena was essential to the safe development of modern space exploration. Pioneering experiments, such as those developed by Rinehart (1950), Rinehart and White (1952), have pushed the understanding of impact mechanisms forward. Modern radiographic techniques and numerical methods have allowed the scientist of today to peer even further into the underlying physics of impact fracture and fragmentation.

Fragmentation Regions

The leading minds in the field of impact fragmentation have not been idle over the past several decades. Grady, Kipp and Swegle (1993) have performed numerous spherical impact tests in hopes of characterizing the properties of high velocity impact phenomena. Using radiographic studies, they concluded from a series of bumper plate trials that three distinct regions of fragmentation existed. The first, and most obvious of the regions was that of zero fragmentation. The impulse generated by the impact

was insufficient to cause fracture and hence no fragmentation of the spherical particles was observed. The second region was labelled cluster fragmentation. A noticeable clustering within the debris cloud could be observed. It was believed to be caused by the spall of material from the rear

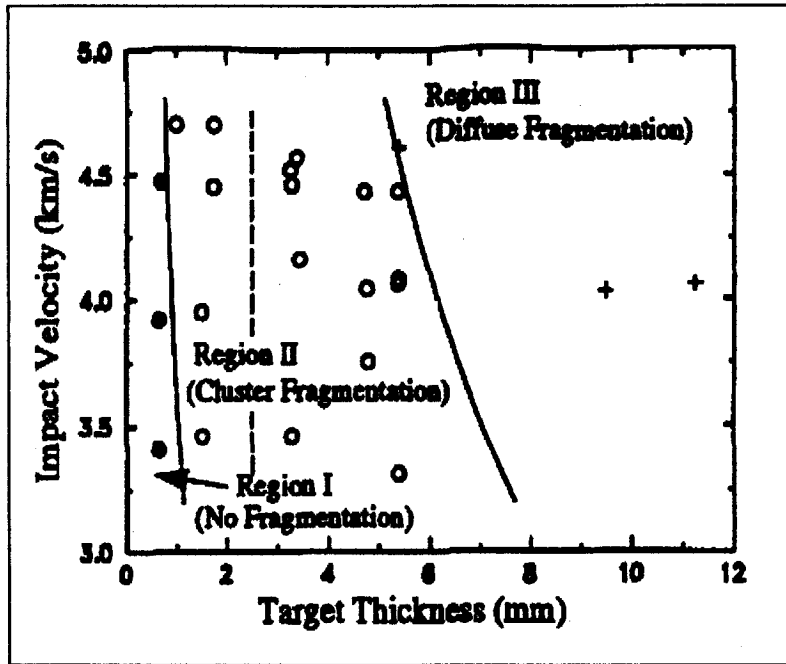


Fig. 3.4-1, Fragmentation regions for spherical impact. Corresponds to fig. 4 of Grady, Kipp and Swegle, 1993.

of the impacting sphere and was only observed when the bumper plate thickness approached that of the sphere diameter. Figure 3.4-2 below is a radiograph that clearly illustrates the cluster fragmentation regime. The final or third region was known as diffuse fragmentation. Within this region, a thinning in the density of the debris was visible as the outer perimeter was approached. Grady and Kipp (1995) coined the phrase that regime III was a transition into a behaviour in which a trailing umbrella pattern of high-radial-velocity fine fragment debris was observed. Figure

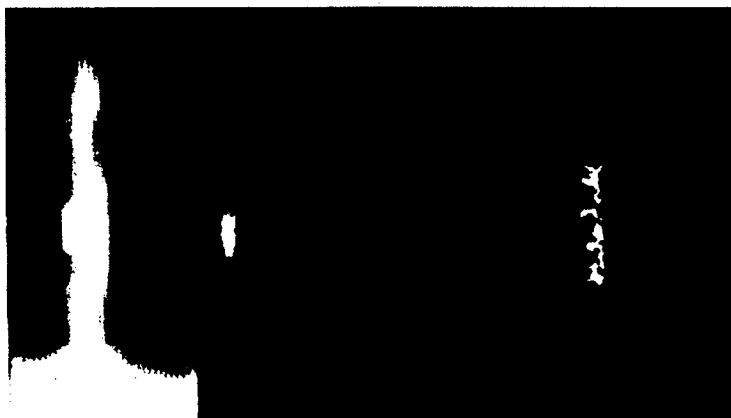


Fig. 3.4-2, Double exposure radiograph of cluster fragmentation of a steel sphere with a glass target impact plate. Corresponds to fig. 2 in Grady and Kipp, 1997.

3.4-1 clearly displays the three regimes of fragmentation for steel particle impact with polymethyl-methacrylate (PMMA) bumper plates as function of impact velocity and target thickness.

Shock Coupled Energy

As a continuation of their previous work, Grady and Kipp proposed the concept of

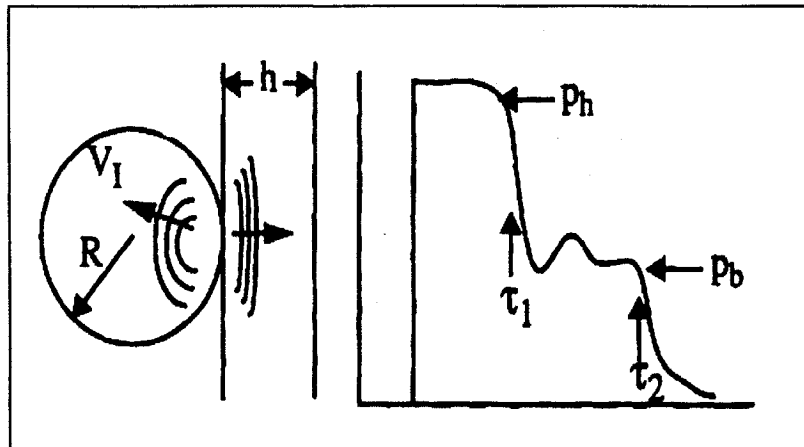


Fig. 3.4-3, Sphere-plate impact with expected pressure profile.
Corresponds to fig. 4 in Grady and Kipp, 1997.

shock coupled energy (1995, 1997). With the aid of computation work performed by Ang (1990), they developed specific expressions for the amount of energy introduced to the

sphere plate configuration by high velocity impact. Figures 3.4-3 and 3.4-4 visually explain the expressions that are to follow.

Before any deformation of the sphere begins, the initial shock pressure developed at the interface is characterized by the Hugoniot shock wave conditions for planar impact of two solids. Hence, the following expression is derived, where Z_S represents the acoustic impedance of the sphere, Z_T represents the acoustic impedance of the target plate and V_I represents the impact velocity.

$$P_h = \frac{Z_S Z_T}{Z_S + Z_T} V_I \quad (3.4-1)$$

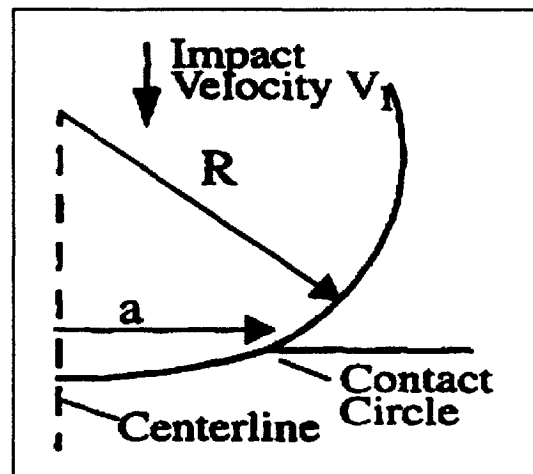


Fig. 3.4-4, Impact circle. Corresponds to fig. 5 in Grady and Kipp, 1997.

This pressure is maintained until the arrival of pressure release waves from the diverging surface of the sphere (τ_1 in Fig. 3.4-3). Further release is realized when the

pressure waves reach the back free surface of the target plate (τ_2 in Fig. 3.4-3). These times are important because the shock does work on the spherical object from the moment of impact until time τ_1 is reached. Grady and Kipp (1997) proposed that this shock coupled energy was largely responsible for fragmentation of spherical samples. Figure 3.4-4 illustrates the outward propagation of the contact circle of radius “a” for a sphere-plate geometry. At initial contact the propagation velocity is supersonic, but rapidly becomes subsonic at a critical radius (a_c) and after a critical amount of time (t_c). These values determine the maximum area of shock coupling into a sphere of given radius (R). Furthermore, the shock coupling is active from the initial growth of the contact circle until the lateral release waves propagate to the central axis. The amount of time required for this process is labelled the shock coupling time ($t_{sc}=t_c+a_c/c$). Using the derivations given by Grady and Kipp (1997), an approximation for the coupled shock energy is given below. Note that the shock coupled energy calculated at the fragmentation threshold should yield an estimate for the required energy input causing spherical particle failure.

$$a_c = V_I t_c \sqrt{\frac{2R}{V_I t_c} - 1} \quad (3.4-2)$$

$$c = V_I \frac{\left(\frac{R}{V_I t_c} - 1 \right)}{\left(\sqrt{\frac{2R}{V_I t_c} - 1} \right)} \quad (3.4-3)$$

$$E_s = \alpha \frac{P^2}{\rho c} a_c^2 t_{sc} \quad (3.4-4)$$

α is a constant taking into account the loading time variation with radius over the contact disk and can be assumed to have a value of $2\pi/3$ for elliptical shock volumes. At high impact velocities, it may be appropriate to replace the acoustic wave speed (c) with the shock velocity (U_{shock}) in order to improve the overall accuracy of the predicted values.

Note that the non-dimensional forms of the previous equations may also be of use in the analysis of impact phenomenon. Identifying the non-dimensional parameters as follows, Equations (3.4-2, 3.4-3 and 3.4-4) can be re-written.

$$U_{nd} = \frac{V_I}{c}; A_c = \frac{a_c}{R}; T_c = \frac{ct_c}{R}$$

$$A_c = \frac{U_{nd}}{\sqrt{U_{nd}^2 + 1}} \quad (3.4-5)$$

$$T_c = \frac{1}{U_{nd}} \left(1 - \frac{1}{\sqrt{U_{nd}^2 + 1}} \right) \quad (3.4-6)$$

$$T_{sc} = \frac{1}{U_{nd}} \left(1 + \frac{U_{nd}^2 - 1}{\sqrt{U_{nd}^2 + 1}} \right) \quad (3.4-7)$$

Energy Balanced Approach

Grady and Kipp (1997) also proposed a different method for the characterization of impact failure criteria. The method worked directly with the expansion velocities obtained from their radiographic analysis of the debris cloud for bumper impact experiments. Although not directly relevant to the experimental work performed for this particular report, it is still instructive to quickly review the technique.

The fundamentals of this approach were to break the problem into two distinct components. The first component was the kinetic energy associated with the sphere's motion and the second component was the energy dissipated during the impact process. The total kinetic energy of the sphere with impact velocity V_I could be simplified into a centre-of-mass, a longitudinal and a radial kinetic energy. Grady and Kipp's (1997) experimental results showed that the longitudinal kinetic energy was

insignificant with respect to the other components and was ignored. They also concluded that the bumper plate impact caused such minor changes in the overall centre-of-mass kinetic energy that it could also be ignored. The energy dissipated during impact could be simplified into plasticity, shock heating and new fracture surface energies. It was also determined that the shock heating and new fracture surface components of the total dissipated energy were minimal with respect to the total amount and were therefore omitted. A simplified version of the system can then be expressed as shown below.

$$E_s = W_p + T_{rad} \quad (3.4-8)$$

The underlying assumption that the input energy was proportional to the square of the shock pressure allowed for the re-organization of Equation (3.4-8). Grady, Kipp and Swegle (1993) expressed the relation as given here, where p_c is the shock pressure at the critical fracture velocity:

$$T_{rad} = W_p \left[\left(\frac{p}{p_c} \right)^2 - 1 \right] \quad (3.4-9)$$

The above relation can again be re-organized if the radial kinetic energy and the dissipative energy are broken into their fundamental components.

$$\frac{v_{expansion}}{v_c} = \sqrt{2} \sqrt{\left(\frac{p}{p_c} \right)^2 - 1} \quad (3.4-10)$$

The previous expression is conceptually useful in the sense that it defines two physical parameters (the critical velocity, v_c and the critical shock pressure, p_c) that completely characterize the impacting material. The critical velocity determines the amount of kinetic energy that can be dissipated during impact without inducing

fragmentation. The critical pressure links the material's shock impedance to its inherent ability of coupling the impact energy into the material itself.

Grady, Kipp and Swegle (1993) pointed out that both the shock coupled energy method and the energy balance approach yielded results that were generally in good agreement. However, they also pointed out that the energy balance approach tended to achieve higher expansion velocities at a given impact pressure. They believed that the inconsistencies in the results were an indication that the constant shock coupling time assumption may not have been appropriate. Calculations using the shock coupled energy method further point to the problems associated with the constant shock energy assumption. Hence, the shock couple energy method is considered more representative of the impact fragmentation process. Figure 3.4-5 and Table 3.4-1 that follow are summaries of the experimental data obtained during the impact trials conducted by Grady and Kipp (1997).

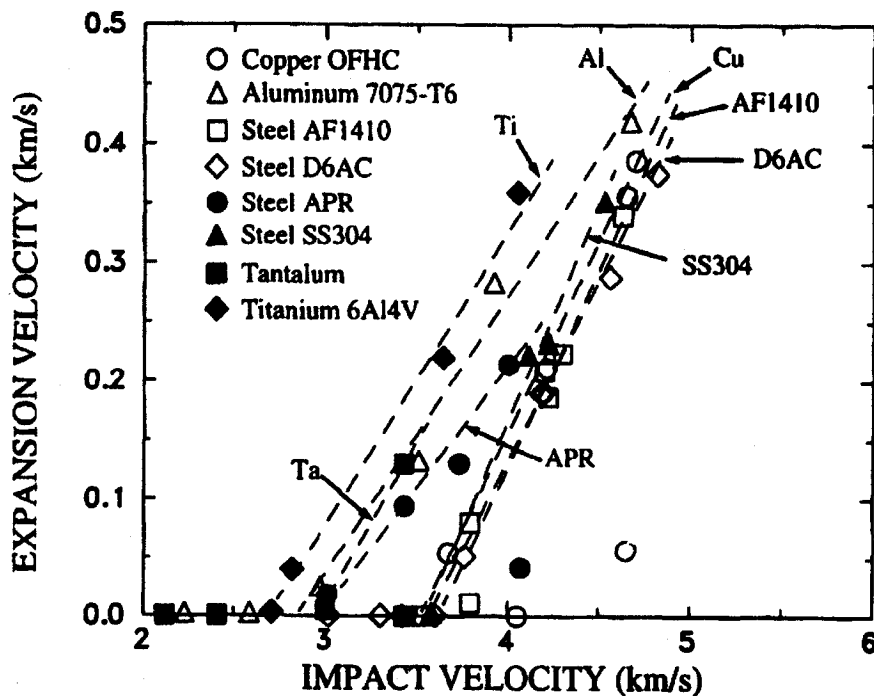


Fig. 3.4-5, Expansion velocity vs. impact velocity for bumper plate trials. Corresponds to fig. 3 in Grady and Kipp, 1997.

Table 3.4-1, Summary of bumper plate results. Corresponds to table 1 in Grady and Kipp, 1997.

Experimental Set-up				Shock Coupled Energy			Balanced Energy			
Material (Sphere)	Density (Kg/m ³)	Material (Plate)	V _{ic} (m/s)	P _c (GPa)	U _c (sphere) (m/s)	U _p (plate) (m/s)	W _p (J/g)	P _c (GPa)	v _c (m/s)	w _p
Al	2800	PMMA	2800	14	6260	5670	32-48	16	199	19.8
Cu	8930	Glass	3500	34	5060	5530	75-56	38	250	31.7
Steel	7900	PMMA	3100	21	5300	6570	23-12	23	129	8.2
Steel	7900	Glass	3650	36	5750	5690	70-66	38	208	21.6
Steel	7900	Glass	3600	35	5730	5640	66-63	38	208	21.6
Steel	7900	Glass	2900	25	5440	4840	25-38	28	124	7.7
Steel	7900	Glass	3600	35	5730	5640	66-63	36	222	24.6
Tantalum	16650	Alumina	2950	80	4640	10300	124-9	81	145	10.5
Titanium	4420	Glass	2650	19	5850	4260	25-75	21	160	12.8

3.5 Metal Particle Combustion

The combustion of metal particles is most simply broken down into two separate categories: volatile and non-volatile metals. A metal's combustion mechanism is considered volatile if its boiling point is below that of the associated metal oxide's boiling point. Furthermore, to be considered volatile the melting point of the metal needs to be low relative to the adiabatic flame temperature of the combustion process. In other words, the metal readily vaporizes and the oxidation reactions occur in the gas phase. Almost all volatile metals burn using mechanisms similar to those of a diffusion flame. For non-volatile metals the oxidation process begins as a heterogeneous surface reaction.

The pressure at which the combustion process takes place plays a key role in the proper development of practical models. The particle diameter is also a crucial parameter with regards to both kinetic and diffusion dominated mechanisms. As stated by Yetter and Drier (2001): "... a very small particle at low pressure conditions

may burn under kinetically controlled conditions, whereas in practice, a more realistic larger diameter particle burning at high pressure would burn under diffusion controlled conditions”. Obviously it is extremely important to understand the effects of both the reaction pressure and particle diameter to fully describe the combustion mechanism.

Volatile Metals

Glassman (1996) experimentally proved that for volatile combustion the heat of vaporization-dissociation of the metal oxide formed was greater than the energy available to raise the temperature of the condensed-phase oxide above its boiling point. The following equation explicitly states the same concept:

$$\Delta H_{vap-dissoc} > Q_R - (H_{T,vol}^0 - H_{298}^0) = \Delta H_{avail} \quad (3.5-1)$$

Q_R is the heat of reaction at the reference temperature, $(H_{T,vol}^0 - H_{298}^0)$ is the enthalpy required to raise the product to its volatilization temperature at the given pressure and $\Delta H_{vap-dissoc}$ is the heat of vaporization-dissociation of the metal oxide.

Von Grosse and Conway (1958) introduced the notion that the combustion temperature was limited by the boiling point of the metal oxide. By simply comparing the boiling point temperature of the metal to the temperature at which the metal oxide vaporizes-dissociates one could determine if a metal would combust in the vapour-phase. This concept has become known as the “Glassman Criterion” for vapour-phase combustion. Table 3.5-1 outlines the basic thermodynamic properties of various metals. Note that if $T_{bp} < T_{vol}$, the “Glassman Criterion” states that the metal can be considered volatile.

Table 3.5-1, Thermodynamic data for various metals. Corresponds to values obtained from Yetter and Dryer, 2001.

Metal	Boiling Point (T_{bp} , K)	Oxide	Volatilization Point (T_{vol} , K)
Al	2791	Al_2O_3	4000
B	4139	B_2O_3	2340
Be	2741	BeO	4200
Cr	2952	Cr_2O_3	3280
Fe	3133	FeO	3400
Hf	4876	HfO_2	5050
Li	1620	Li_2O	2710
Mg	1366	MgO	3430
Ti	3631	Ti_3O_5	4000
Zr	4703	ZrO_2	4280

The simplest way to visualize the importance of the boiling point relationship is to compare the equilibrium product composition and temperature for stoichiometric reactions. Figure 3.5-1 is a clear representation of the Magnesium volatile reaction as a function of input enthalpy. Note the reactants are initially at 298 K and 1 atm. One should note the rise in system temperature until saturation of metal oxide was achieved in the liquid phase. The temperature then levelled off during the zero input enthalpy range as the metal oxide vaporized. The temperature remained constant

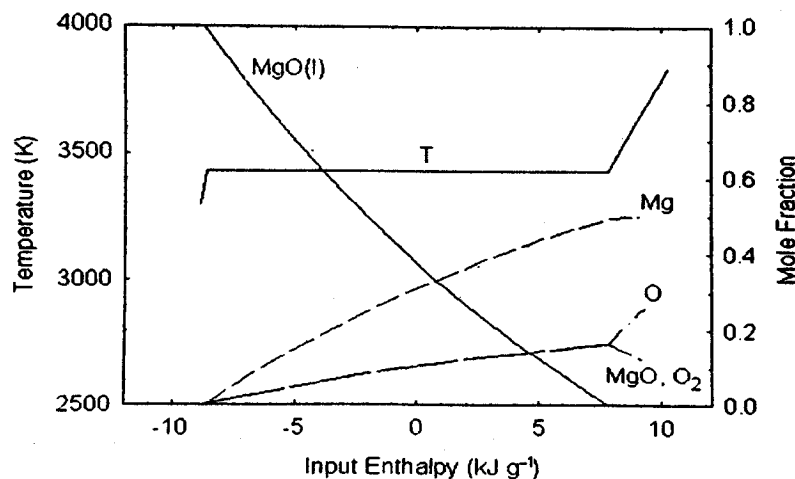


Fig. 3.5-1, Equilibrium product composition and temperature for stoichiometric Magnesium combustion. Corresponds to fig. 4 of Yetter and Dryer, 2001.

because the dissociation of MgO absorbed all changes in the total system enthalpy. The difference in input enthalpy during the level temperature plateau determined the enthalpy of volatilization for a

given metal. If the plateau encompassed the zero input enthalpy point, then the metal was deemed volatile and the oxidation process used vapour-phase combustion mechanisms (Yetter and Dryer, 2001). The system required no additional energy input because the heat of reaction was sufficient to allow the metal itself to vaporize before the respective metal oxide could dissociate. The previous statement is a concise description of volatile combustion.

Brzustowski and Glassman (1960) presented a summary paper detailing the volatile combustion mechanism for various particle sizes. For particles with high surface area to volume ratios convective heat transfer from the flow field quickly melted the metal. The melting process was extremely rapid and little oxidation occurred on the surface of the droplet that could hinder the evaporation of the metal or diffusion of the vapour away from the outer surface. The vapour pressure was normally high, allowing for a rapid gas-phase reaction. Heat from the combustion process flowed back into the liquid droplet increasing the temperature and vapour pressure of the metal until stable combustion was achieved (Wood, 1960; Brzustowski and Glassman, 1960).

Gordon (1960) discovered a slightly modified combustion process for volatile metal but with larger particle sizes. The heat transfer to the larger mass was insufficient to prevent the build up of an oxide layer. The oxide layer was still porous, so the diffusion flame process continued. The heat transfer feedback mechanism discussed earlier slowly heated up the metal under the thickening oxide layer. The metal eventually boiled, became slightly superheated and burst the outer layer. The droplet then broke into smaller particles and it burned as described for high surface area to volume particles.

Non-Volatile Metals

A second look at Table 3.5-1 would demonstrate that only Boron and Zirconium would be considered as non-volatile metals using the "Glassman criterion". However, Yetter and Dryer (2001) pointed out the fact that radiative, conductive and convective thermal losses could alter the volatile nature of Chromium, Iron, Hafnium and Titanium because each of their respective metal boiling points was within 400 K of

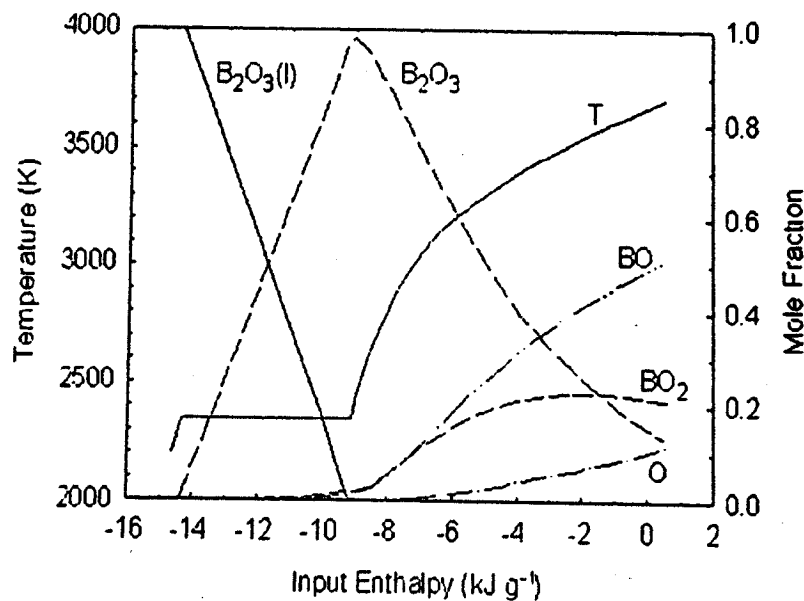


Fig. 3.5-2, Equilibrium product composition and temperature for stoichiometric Boron combustion. Corresponds to fig. 5 in Yetter and Dryer, 2001.

stoichiometrically at 298 K and 1 atm. The most important feature of the plot is a non-existent temperature plateau at the zero input enthalpy point. This is expected because Boron is predicted to have a heat of reaction that is sufficiently large to raise the temperature of the final oxide above its vaporization point. However, the energy yield is not sufficient to raise the Boron metal temperature above its respective vaporization temperature. In other words, the metal oxide vaporized before the metal itself.

Again, Brzustowski and Glassman (1960) explained the various effects of particle size on volatile combustion. For large non-volatile particles with non-soluble oxide

their metal oxide volatilization temperatures.

Figure 3.5-2 is a similar plot to that presented previously for the Magnesium volatile combustion process. In this instance, however, the metal of choice is Boron.

It is being oxidized

layers the rate of heat transfer from the flow field was normally very low. This allowed for the build up of an oxide layer, thus inhibiting any ignition of the metal itself. However, if the particle was small enough several interesting mechanisms for the metal combustion process could develop. Firstly, if the surface temperature remained below that of the metal oxide's melting point, then the oxide layer continued to thicken and quenched any ignition potential. Secondly, if the oxide layer melting point was reached, then the metal diffusion through the liquid layer became the limiting step. The surface reaction continued until only a particle of molten metal-oxide remained. Thirdly, if the flow field was hot enough and the residence time long enough, it was possible that the metal within the oxide layer reached its boiling point. It could become slightly superheated, then burst the outer shell and burn as a vapour-phase mixture discussed earlier (Fassell and Papp, 1960).

If the oxide was soluble within the metal of interest, the combustion process was altered somewhat. Again for small particles, the metal began to melt before an appreciable oxide layer could form. The burning of the molten droplet was then limited by the diffusion of oxygen and metal through the solid oxide. If the rate of heat loss from the droplet surface was such that the oxide melting point was never reached, then the slow burning process continued and was limited by the diffusion of oxygen and metal through the solid oxide layer. This mechanism could continue until all of the metal was oxidized, simply leaving a particle of solid metal-oxide. If the temperature was elevated to the melting point of the oxide, then the diffusion mechanism through the liquid oxide became the rate-limiting step. This process led to the evaporation of the oxide and complete oxidation of the metal itself. If the temperature is elevated even further, to the boiling point of the metal, the droplet fragments and burns under the vapour-phase diffusion mechanism.

It is important to note that for Titanium and Zirconium the latter mechanism does not seem possible because of the elevated temperatures required and the radiant heat losses associated with such high temperatures. However, Brzustowski and Glassman (1960) discovered a much more common fragmentation mechanism associated with the

combustion of Titanium and Zirconium. For larger particles, a substantial oxide layer was formed on the outer surface of the particle before all of the metal was melted. The oxides formed a solid solution with the metals and allowed for substantial diffusion of oxygen and metal through the solid layer. A slow surface burn was achieved and the heat developed allowed for the eventual attainment of the metal's melting point. The melting shattered the solid oxide (because there was no distinct interface between the metal and oxide) and caused severe fragmentation of the particle into small droplets (Wood, 1960; Brzustowski and Glassman, 1960). The droplets then continued to burn as small particles described previously.

Combustion of High Velocity Spheres

Higgins, *et al.* (2001) performed a series of experiments using a light gas gun that established some general criteria for the ignition of supersonic metal particles. One of the original objectives of the trial series was to determine if combustion of the high velocity particles would yield a reduction in the overall drag coefficient. It is still informative to review their summary of the ignition criteria. Figure 3.5-3 shows the stagnation temperature (T_0) and the normal shock temperature (T_{shock}) as functions of the particle Mach number. The plot assumed ideal gas behaviour and also labelled the melting points and boiling points of each of the respective metals tested.

They determined that the melting temperatures of the volatile metals were not reached until the flow exceeded Mach 3. At approximately Mach 7, the temperatures reached well above 3000°C and eventually surpassed the metal-air combustion adiabatic flame temperatures. This means that standard combustion mechanisms would not be possible at such elevated velocities where the flow enthalpy completely dominates the thermodynamic processes. They concluded that a small window of Mach numbers (ranging between 3 and 6) would allow for the combustion of the particles to take place and ultimately influence the thermodynamics of the flow field. Calculations performed in order to determine the extent of heat penetration into the particles

demonstrated that only a thin outer surface layer would be influenced by the flow conditions. Table 3.5-2 below is a brief summary of the results Higgins, *et al.* (2001) obtained. Notice that the atmospheric pressure and composition were

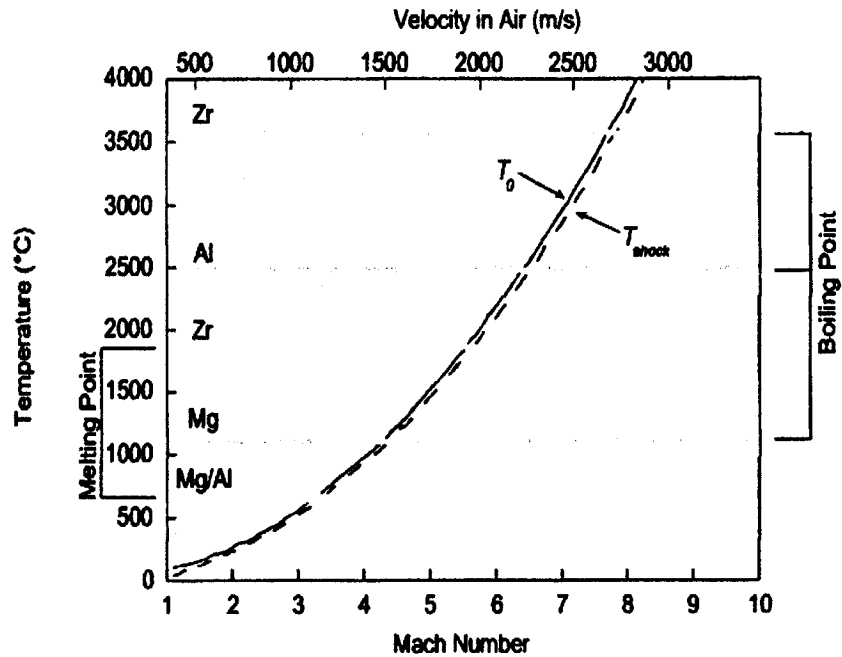


Fig. 3.5-3, Shock and stagnation temperatures vs. Mach number. Corresponds to fig. 1 in Higgins, *et al.*, 2001.

changed within the test section. “Go” and “No-Go” ignition behaviour was observed. Interestingly, Zirconium particles were the only material that continued to burn after the sphere experienced a transition from an oxygen to air atmosphere.

Table 3.5-2, Summary of ignition conditions. Corresponds to the table given in Higgins, *et al.*, 2001.

Shot	Material	Gas	Pressure (bar)	V_0 (km/s)	Ignition
BS06	Mg	O ₂	1	2.02	No
BS08	Zr	Air	1	1.93	No
BS10	Al	Air	1	2.01	No
BS12	Al	O ₂	1	1.54	No
BS13	Al	O ₂	5	1.55	No
BS16	Zr	Air	1	1.93	No
BS21	Cu	O ₂	10	1.94	No
BS07	Zr	O ₂	1	1.93	Yes
BS09	Al	O ₂	1	2.00	Yes
BS11	Mg	O ₂	5	1.42	Yes
BS19	Zr	Air	1	1.93/1.89	Yes
BS22	Zr	O ₂	10	1.90	Yes

4.0 Experimental Results

Three independent trial series were conducted in order to experimentally determine the dispersal and fragmentation properties of Zirconium metal particles. Each experimental set-up and procedure will be described in the pages that follow with a brief summary of the results. Analysis and discussion of the obtained data will be presented at length in Section 5.0. Note that the explosive dispersal trials were conducted during 4 consecutive summers in Suffield, Alberta. All of the different trial series were joint ventures of the department of Defence Research and Development Canada and a team of students and staff from McGill University. The explosive gun barrel tests were conducted in conjunction with the most recent dispersal trial series and were also carried out at the experimental test range near Suffield, Alberta. The final series of trials involving the Light-Gas Gun apparatus were performed at the University of Sherbrooke, in Sherbrooke, Quebec. Dr. Martin Brouillette of the Mechanical Engineering Department generously donated access to the laboratory and any necessary technical expertise.

4.1 Explosive Dispersal Test Apparatus

The explosive dispersal tests were an extensive series of trials attempting to characterize the overall blast behaviour of heterogeneous explosives. The work has been a progressive evolution from fundamental detonation propagation experiments (Lee, *et al.*, 1995a), to sensitization of homogeneous explosive trials (Lee, *et al.*, 1995a, 1997), to heterogeneous blast effects (Frost, *et al.*, 2001, 2002, 2003a; Lanovets, *et al.*, 1991; Zhang, *et al.*, 2001) and now to high-velocity impact fragmentation (Frost, *et al.*, 2003b). The specifications for each individual experimental set-up are clearly explained in each of the referenced articles.

The dispersal trials conducted specifically for the work at hand consisted of centrally detonated spherical glass bulbs. Many of the trials were recorded using 2000 frames/s

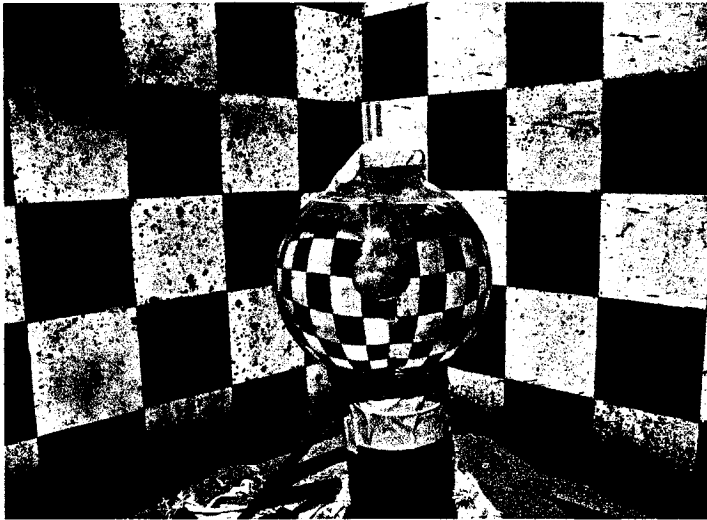


Fig. 4.1-1, Spherical charge consisting of NM+10%TEA with centrally located booster of DM-12.

high-speed video cameras. The charges were 12.3 cm in diameter in a packed-bed configuration saturated with sensitized liquid explosive. Throughout all of the trials, the liquid explosive was Nitromethane sensitized 10% by weight with Tri-ethylamine (TEA). Figure 4.1-1 obviously displays a sensitized Nitromethane

charge without any particles. One should also notice the centrally located booster (5-10 g) of DM-12 plastic explosive. The booster was located in a glass bulb with an approximate volume of 5 ml. The bulb was blown at the tip of a small glass tube with an inner diameter of 8 mm. The tube was held in place at the centre of the charge using epoxy and a small wooden slat. A Reynold's Bridgewire detonator (RP-2 or RP-83) was inserted into the glass tube to the centre of the charge.

In some cases, the charges were placed next to a rigid steel plate (1.83m square x 5.1cm) with a flush mounted tourmaline pressure bar (PCB 134A22). The face of the transducer was protected from the high-velocity particles with a thin perforated metal



Fig. 4.1-2, Pressure stands and reflective plate set-up.

screen. Calibration tests with Nitromethane charges indicated that the screen attenuated the maximum peak overpressure spike by up to 50% but affected the overall positive phase pressure impulse by less than 5% (Frost, *et al.*, 2001; Zhang, *et al.*, 2001). Six independent piezoelectric pressure transducers tracked the propagation of the blast wave and recorded the pressure history. They were flush-mounted on sharp-edged steel discs (30 cm diameters) and located from 0.6 m to 2.5 m from the centre of the charge. The transducer rise-time was estimated at 1 microsecond and the signals were recorded using a 25 MHz bandwidth data acquisition system (PC based). The charge and pressure gauges were placed 1.5 m above the ground in order to minimize the effects of ground reflected waves.

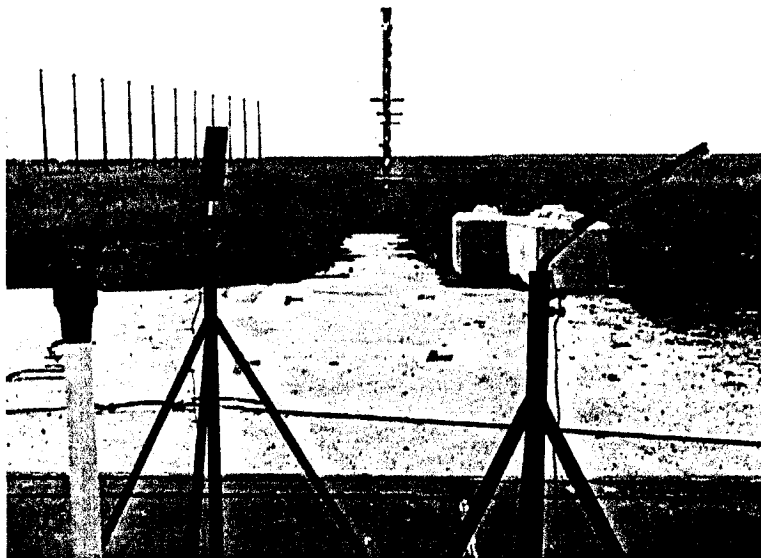


Fig. 4.1-3, Cantilever gauge set-up. Photo taken after trial, hence resultant deflection was caused by a centrally initiated charge.

Cantilever gauges were also implemented in conjunction with the disc mounted pressure transducers. The gauges consisted of 9.5 mm or 6.4 mm diameter aluminium rods. Steel plates of 5.08 cm x 20.32 cm x 4.8 mm were also mounted to the rods in order to increase the overall deflection.

Bending angles were measured and although the complete analysis of the cantilever loading and motion was extremely complex, some general comments could be made about the impact-fragmentation induced impulsive loads.

4.2 Explosive Dispersal Test Results

Although numerous trials were performed with a large variety of materials, four different charge set-ups were chosen to illustrate the effect of particle size and reactivity on the overall blast characteristics. Large Zirconium particles with diameters of $725 \pm 125 \mu\text{m}$ were purchased from Atlantic Equipment Engineering. Packed bed charges of this material were detonated in order to demonstrate the rapid acceleration and subsequent fragmentation of large inertia particles. Small aluminium particles with diameters of 100-200 ηm were obtained from Argonide Corp under the brand name of ALEXTM. These particles were centrally exploded in a packed bed configuration causing them to burn and quickly equilibrate with the local flow velocity. They were not expected to fragment upon impact. Both of these particles were compared with previous trials involving inert iron beads with diameters of $463 \pm 38 \mu\text{m}$. Sensitized Nitromethane charges without any particles were also conducted. Trials not relevant to the present work have been omitted. Note that all of the relevant raw data can be found in Appendix A at the end of this report.

Zirconium / Nitromethane	→ 2265g / 655g	→ 8 Trials
ALEX / Nitromethane	→ 300g / 900g	→ 9 Trials
Iron / Nitromethane	→ 4450g / 430g	→ 1 Trial
Nitromethane Only	→ 1000g	→ 3 Trials

Figure 4.2-1 is the graphical representation of the peak overpressures obtained for the four charge configurations as a function of distance from ground zero. The first observation that could be made with regards to the pressure profile was that the decay of the pressures with increasing distance was qualitatively similar for both the Zirconium/Nitromethane and the Iron/Nitromethane mixtures. This phenomenon was most easily explained by the fact that each of the mixtures contained relatively large particles. Therefore, these charges were expected to exhibit similar decay profiles because of the interaction between the particles and the flow field. The significant difference in overpressure magnitude was caused by the additional energy release of

the Zirconium combustion reactions within a timescale that altered the blast wave propagation.

The ALEX/Nitromethane and Sensitized Nitromethane mixtures also behaved similarly. Presumably, the small sized (100-200 μm) ALEX particles equilibrated quickly within the flow field because of the momentum relaxation timescale discussed in the literature review section for particle dispersal. The equilibration of the particles within the flow field minimized their influence on the decay of the blast wave. The overall behaviour of the ALEX/Nitromethane mixture was therefore very closely related to that of the homogeneous Sensitized Nitromethane charge. Again, the noticeable difference in overpressure magnitude was explained by the energy release of the ALEX combustion reactions within a timescale that altered the blast wave propagation.

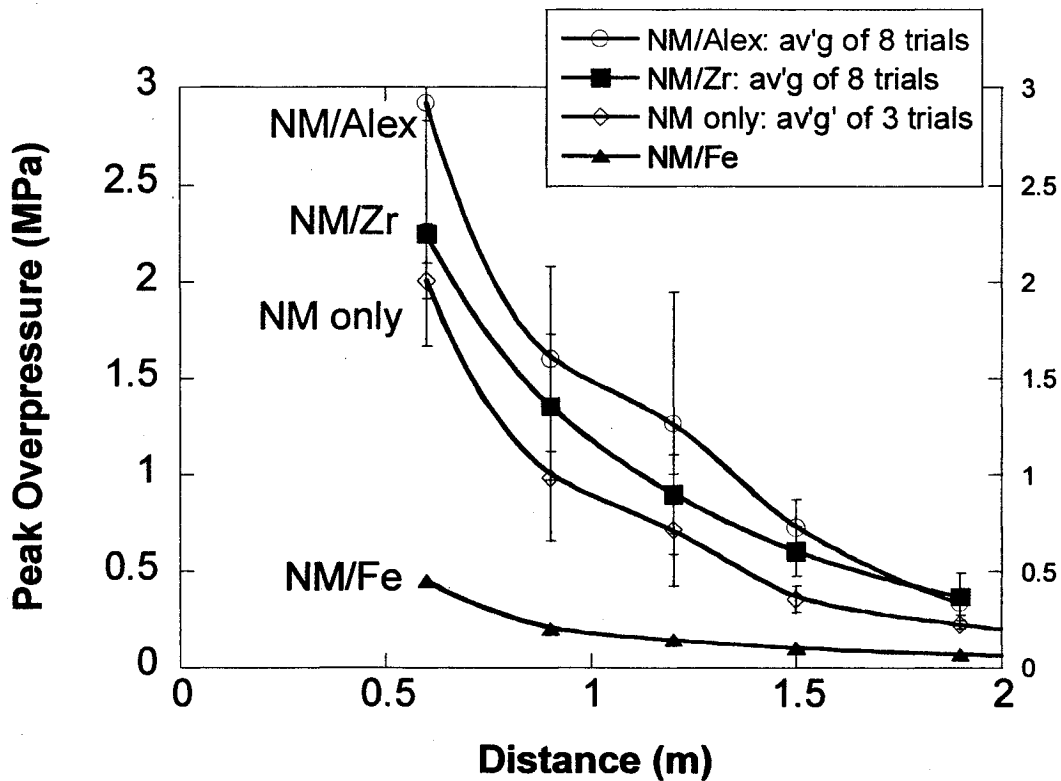


Fig. 4.2-1, Peak overpressure profiles for centrally initiated charge compositions.

Although the ALEX/Nitromethane charges produced larger magnitude peak overpressures than the Zirconium/Nitromethane mixtures, they generated significantly smaller positive phase pressure impulses. This result was even more evident when comparing the “reflected” values within the near field (distances ranging from 0.6-1.2 meters). Figure 4.2-2 is a clear representation of the previous statement. Work by Zhang, *et al.* (2001) and Frost, *et al.* (2001) explained that the near-field locations would correlate well with the expected distance for initial particle penetration of the shock front. In other words, the near-field distances where augmented reflected impulses were observed could be explained by the arrival of the particles slightly before the blast wave. If the particles fragmented upon impact, then the augmentation of the impulses could be explained by the energy release associated with the increased surface area of the combusting Zirconium particles.

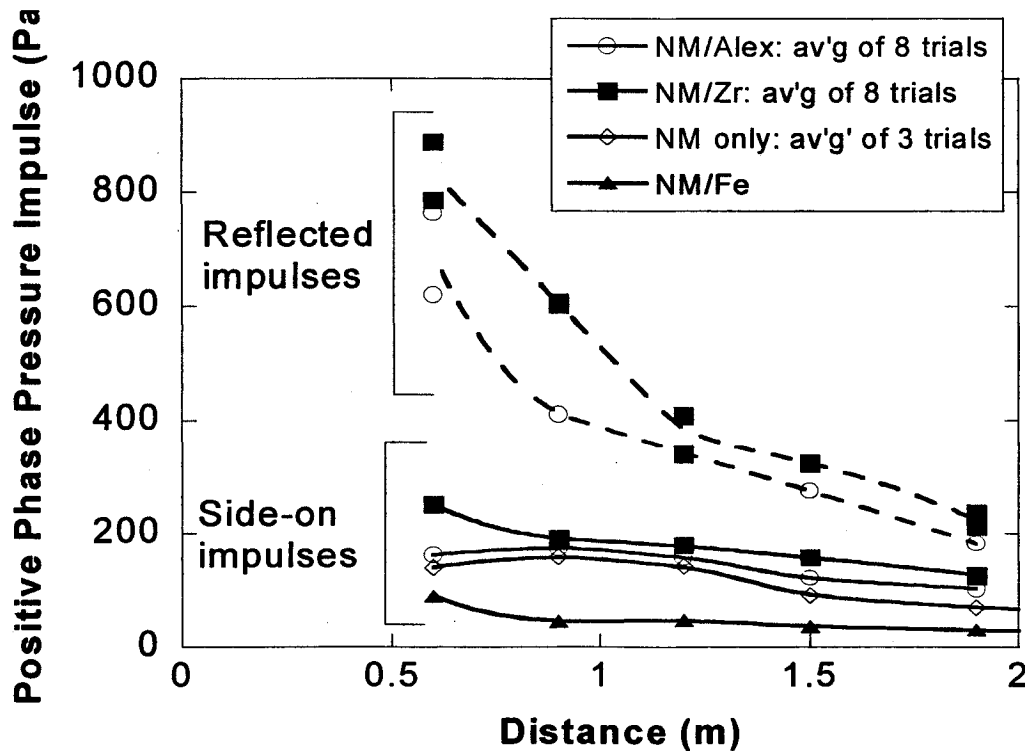


Fig. 4.2-2, Positive phase pressure impulse profiles for centrally initiated charge compositions.

The cantilever gauge was a simplistic tool that enabled the qualitative analysis of blast waves. By comparing the bending angles of the gauges for different charges, the strength of the blast and its relative impulsive loading characteristics could be calculated. Although the loading and motion of the gauges were extremely complex, some fundamental behaviour could be estimated from even the simplest models. The series of trials using these gauges yielded several indirect links to the fragmentation and subsequent increased loading for Zirconium/Nitromethane charges. Figure 4.2-3 displays the different craters developed for 1 mm diameter Steel particles and 725 μm

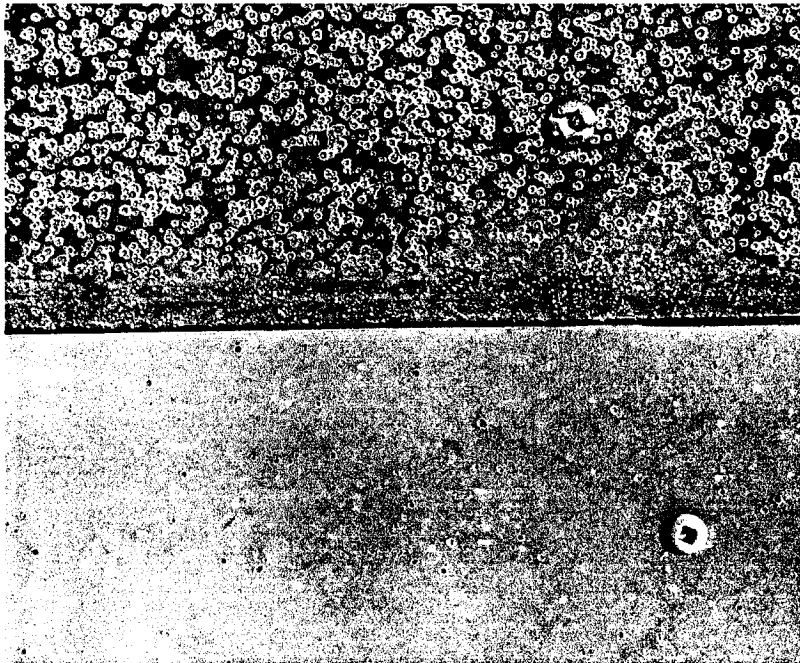


Fig. 4.2-3, Impact craters on cantilever gauges for 1 mm diameter Steel (Top) and 725 μm diameter Zirconium (Bottom) particles.

diameter Zirconium particles. The first conclusion that could be drawn was that the impact crater density for the steel particles was substantially greater. The larger number of craters was directly linked to the fact that the steel particles did not fragment upon impact with the gauges. However, the same

could not be said for the burning high velocity Zirconium beads. The partially molten Zirconium particles obviously fragmented upon impact with the steel gauge surface. The bottom picture in Figure 4.2-3 above clearly demonstrates the lack of impact craters. The craters that were present after the detonation of Zirconium/Nitromethane charges were caused by the impact of the inner solid kernels, thus leaving much smaller and fewer scars on the gauge surfaces.

After further inspection of the gauges, it was noticed that they were covered in a fine grey dust. The thin layer was relatively uniform over the entire gauge surface for the Zirconium trials, but was not observed after the detonation of Iron/Nitromethane mixtures. It was therefore concluded that the presence of this Zirconia powder added greater weight to the assumption that the particles fragmented upon impact with the gauges and that the subsequent burning of those fragments enhanced the blasts impulsive loading. Figure 4.2-4 below is a graphical representation of the cantilever bending angle data.

The key feature of the plot below was the noticeable difference in bending angles when comparing the Zirconium/Nitromethane and ALEX/Nitromethane trials. Although comparable bending angles were observed in the far-field, the Zirconium mixtures yielded substantially greater deflections in the near-field. One should remember that both ALEX and Zirconium mixtures generated similar overpressures, but substantially different positive phase pressure impulses (See Figures 4.2-1 and 4.2-2). The cantilever gauge trials confirmed the previous findings that involved only pressure gauges. The cantilever trial series re-iterated the phenomenon of an

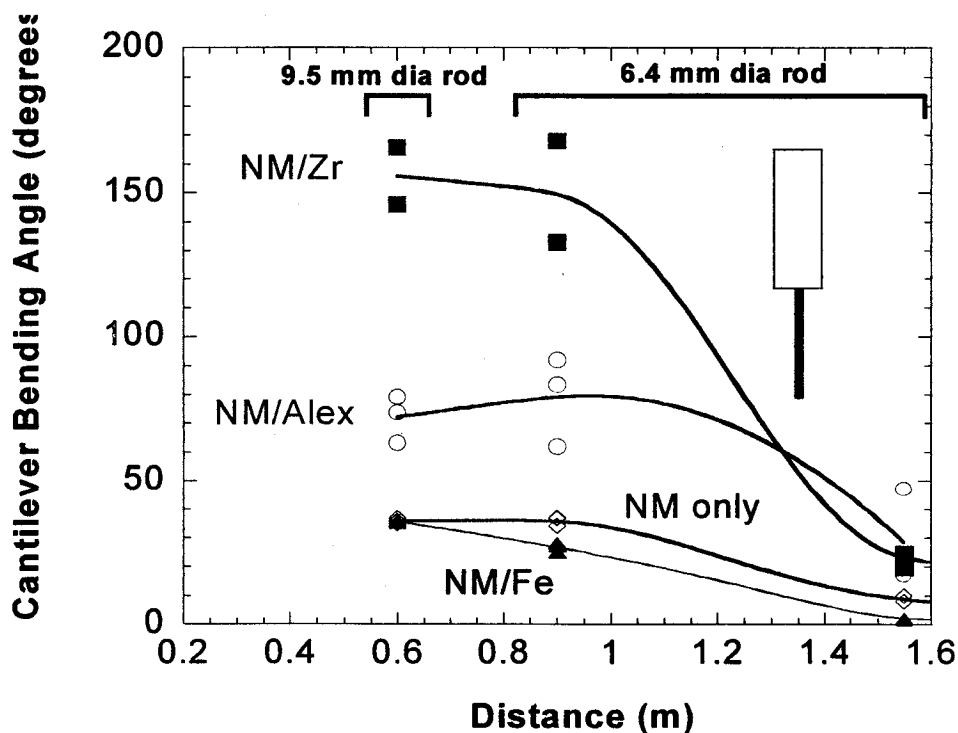


Fig. 4.2-4, Cantilever trial data for centrally initiated charge compositions.

augmentation of the positive phase pressure impulse for Zirconium/Nitromethane charges in the near-field.

The tables that follow are a summary of the data presented in the previous Figures of this section. A complete list of trials and their respective pressure and impulse data can be found in Appendix A at the end of this report.

Table 4.2-1, Average Zirconium experimental pressure and impulse data.

Gauge (cm)	Pressure (MPa)	Impulse (Pa-s)
60	2.25	252.40
90	1.29	191.70
120	0.90	178.70
150	0.60	157.88
190	0.37	126.48
60 Reflected	6.79	835.86
90 Reflected	7.01	606.02
120 Reflected	1.75	399.57
150 Reflected	3.74	325.80
190 Reflected	2.62	214.05

*The data above represents average values calculated from trials 2000-16, 2000-20, 2000-27, 2000-31, 2000-32, 2001-19, 2001-25 and 2002-16.

Table 4.2-2, Average ALEX experimental pressure and impulse data.

Gauge (cm)	Pressure (MPa)	Impulse (Pa-s)
60	2.92	163.24
90	1.77	173.92
120	1.58	168.26
150	0.73	110.50
190	0.33	104.23
60 Reflected	13.52	691.90
90 Reflected	9.82	411.30
120 Reflected	2.79	n/a
150 Reflected	3.46	275.68
190 Reflected	1.61	191.91

*The data above represents average values calculated from trials 2000-43, 2000-46, 2000-50, 2000-51, 2001-16, 2001-24, 2001-31, 2001-40 and 2001-42.

Table 4.2-3, Average Nitromethane experimental pressure and impulse data.

Gauge (cm)	Pressure (MPa)	Impulse (Pa-s)
60	2.01	140.64
90	0.99	159.16
120	0.72	142.48
150	0.23	90.34
190	0.11	69.47

*The data above represents average values calculated from trials 1999-42, 1999-51 and 1999-54.

Table 4.2-4, Average Steel experimental pressure and impulse data.

Gauge (cm)	Pressure (MPa)	Impulse (Pa-s)
60	0.44	N/A
90	0.33	57.09
120	N/A	N/A
150	0.12	42.30
190	0.07	33.47

*The data above represents average values calculated from trials 2001-21.

Table 4.2-5, Experimental cantilever data.

Gauge (cm)	Bending Angle (Degrees)			
	Zirconium	ALEX	Steel	Nitromethane
60*	166 (2001-33)	63.5 (2001-18)	35 (1998-63)	37 (1998-62)
60*	146 (1999-63)	74.0 (2001-41)	36 (1998-66)	36 (1998-67)
60*	N/A	79.4 (1999-56)	35 (1998-65)	35 (1998-70)
90	168 (2001-03)	62.0 (2001-18)	27(1998-63)	36 (1998-62)
90	133 (1999-63)	92.0 (2001-41)	28 (1998-66)	37 (1998-67)
90	N/A	83.0 (1999-56)	25 (1998-65)	34 (1998-70)
155	24.5 (2001-03)	47.0 (2001-18)	2.0 (1998-63)	8.0 (1998-62)
155	20.0 (1999-63)	20.5 (2001-41)	2.0 (1998-66)	10 (1998-67)
155	N/A	17.5 (1999-56)	1.5 (1998-65)	8.0 (1998-70)
200	N/A	N/A	1.0 (1998-63)	3.0 (1998-62)
200	N/A	N/A	1.0 (1998-66)	3.0 (1998-67)
200	N/A	N/A	1.0 (1998-65)	3.0 (1998-70)

* All Cantilever Gauges at a Distance of 60cm used 9.5 mm Diameter Aluminum Rods Whereas All Other Gauges Used 6.4 mm Diameter Aluminum Rods.

** The number in the brackets represents the individual trial numbers.

4.3 Explosive Gun-Barrel Test Apparatus

Explosive acceleration of individual Zirconium particles was investigated. Using computer-numerically-controlled machining techniques, Zirconium spheres of 6.4

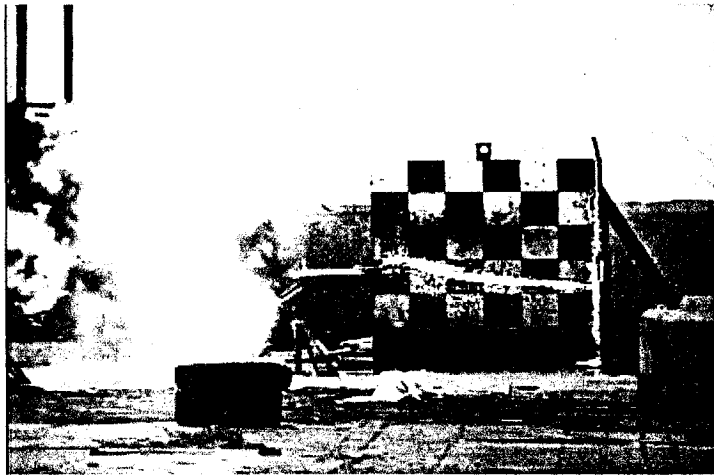


Fig. 4.3-1, Side-view for explosive acceleration of a single Zirconium particle.

mm diameters were produced from high purity stock rod. Tests were also conducted using Al, Mg, and W spheres of similar diameters. The experimental set-up is simplistically modeled as shown in Figure 4.3-2. The length of the Detaprime explosive driver section was varied from 0.4

m to 2.3 m in length. Its unit length density was measured to be 354 g/m. The launch tube section was maintained at a length of exactly 1 m. The distance from the end of the launch tube to the impact plate remained greater than 60 cm. This was done in order to guarantee that the Zirconium particle would impact ahead of the detonation products.

Aluminum and Copper foil gauges were also utilized in order to measure the impact velocity of the particle just prior to impact.

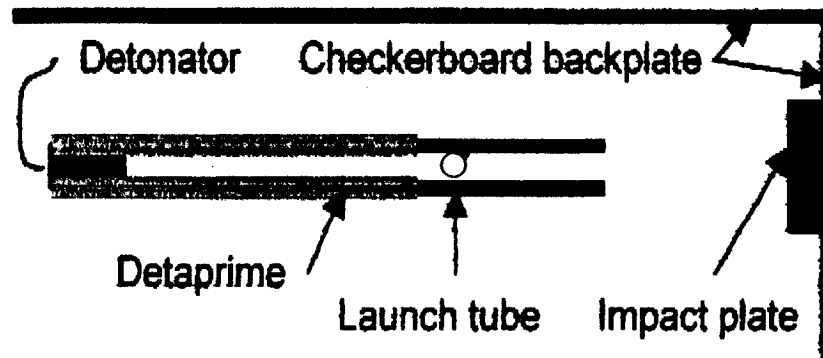


Fig. 4.3-2, Top view of experimental set-up for single particle impact tests using gun-barrel design.

Unfortunately this particular technique proved unreliable and the results were discarded. All velocities were calculated with the aid of video analysis. Digital cameras with shutter speeds of 2000 frames/s were implemented in order to visualize the impact and subsequent fragmentation processes. In all cases the checkerboard pattern in the background are 30 cm squares with a normal time of 0.5 ms between frames.

4.4 Explosive Gun-Barrel Test Results

The Zirconium particles were accelerated to velocities between 150 m/s and 2.5 km/s. In all cases, the spheres ignited prior to exiting the launch tube and partially melted during the acceleration phase. This was the first important result of the trial series in that it proved the ignition of large diameter Zirconium particles was possible. This proof was extremely important because all previous work in the dispersal trials was limited to particles with diameters of less than 1 mm. The thermal boundary layer of the particle was found to be approximately 1 mm after a time period of 1 ms (Frost, *et al.*, 2003b). This implies that the particles would have only a thin liquid layer surrounding a solid Zirconium core just prior to impact. Since the Zirconium metal

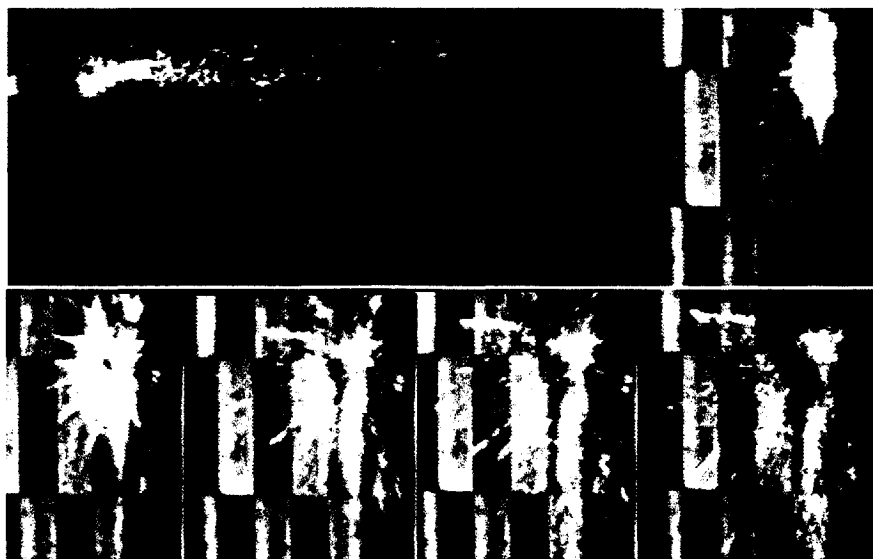


Fig. 4.4-1, Top frame: gun barrel visible on the left. Fine fragments stripped from the burning sphere at the exit of the launch tube. The impact point is clearly visible at right. Lower Frames: Initial impact of burning sphere (left frame) and subsequent fragmentation and dispersion after impact (both middle and right frames).

particles burned by a heterogeneous surface reaction and because of the low thermal conductivity of Zirconium, it was believed that the outer surface reaction could be sustained

without tremendous heat loss to the solid kernel. This in turn allowed for the system to be considered as two separate entities, the first entity being the outer liquid layer and the second entity being the inner solid kernel. Closer inspection of Figure 4.4-1 visually supports the idea of a liquid outer layer and a solid inner kernel. The top frame clearly shows the stripping-off of the outer liquid layer as the particle is accelerated towards the right. The bottom frames demonstrate the impact, fragmentation and subsequent ignition of the inner solid kernel. It was this phenomenon that encouraged the completion of a third set of trials involving the impact and fragmentation of non-ignited particles described in the following section.

It should be noted that for all velocities tested the Zirconium particle fragmented upon impact with the rigid steel plate. Again within the video stream, the fragmentation process is clearly visible. Unfortunately, the long duration of the frames makes for a streak type photo instead of crisp individual frames. The Figures that follow are summary videos of the results obtained at low, mid and high impact velocities within the range tested.

A few simple observations could be made when inspecting each of the video streams presented on the following pages. Figure 4.4-3 displays the explosive acceleration of a Zirconium particle to a velocity of approximately 160 m/s. Fragmentation of the particle and its subsequent ignition are clearly visible, and an extremely shallow ejecta angle is produced. Closer examination of the raw video files yield an estimate for the backscatter angle of $3.8 \pm 2^\circ$ Figure 4.4-4 displays very similar characteristics for an impact at 400 m/s. Again a very shallow ejecta angle is produced and ignition of the Zirconium fragments is visualized.

One of the more interesting phenomena observed was the potential secondary fragmentation of the already fractured solid kernel. With initial impact velocities of approximately 650 m/s, secondary fragmentation was observed as the ejecta from the first impact event struck another nearby solid structure. This led to the assumption that the initial solid kernel fragmented upon impact into several other similar systems

with outer liquid layers and inner solid kernels. Figure 4.4-2 demonstrates the second impact event almost 17 ms after the initial impact. From the video analysis, the secondary impact velocity was approximated at 150 m/s. Figure 4.4-5 displays selected frames of the acceleration and impact at the approximated velocity of 650 m/s and shows that the ejecta backscatter angle increased when compared with slower

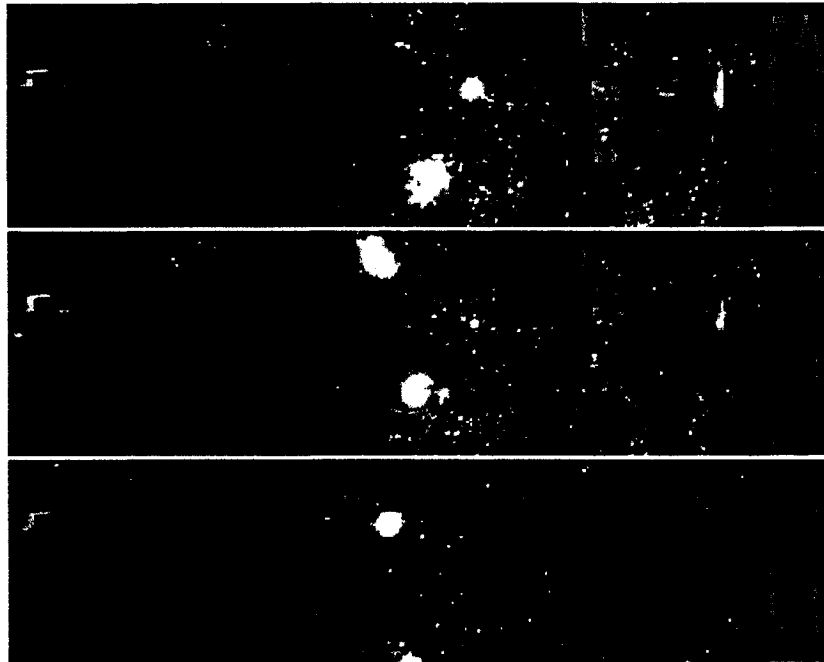


Fig. 4.4-2, Secondary impact events on perpendicular plate 17 ms (top) 19 ms (middle) and 30 ms (bottom) after initial impact event.

velocities. Again, examination of the raw video files produced an estimate of $11.3 \pm 2^\circ$ for the backscatter angle. Figure 4.4-6 also displays that as the velocity is increased to 2.5 km/s the ejecta backscatter angle increased to approximately $35 \pm$

10° . It can therefore be concluded that an increase in the impact velocity produces an increase in the ejecta's backscatter angle.

The most important aspect of this set of trials was that it linked the fragmentation process to the subsequent increase in energy release associated with a larger reactive surface area. It was concluded that the high-velocity fragmentation process resulted in a greater reactive surface area and showed that ignition of the fragments was instantaneous. Therefore the entire mechanism could affect the thermodynamics of the flow field prior to the arrival of the blast wave. Thus even greater weight was added to the hypothesis that fragmentation of the Zirconium particles within the near-field enhances the overall positive phase pressure impulse.

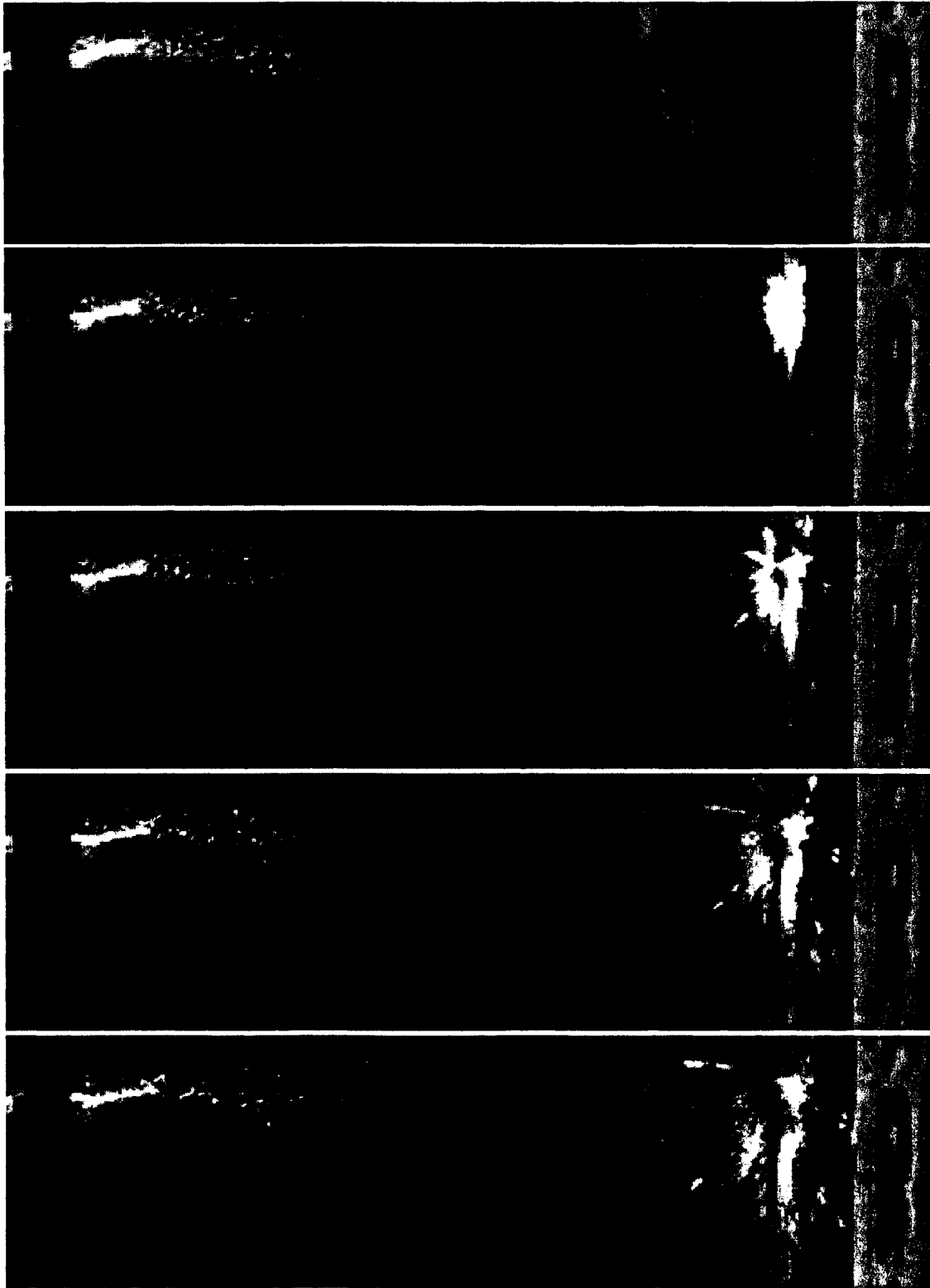


Fig. 4.4-3, Impact of Zirconium 6.4 mm diameter particle at 160 m/s. Time between frames of 0.5 ms.

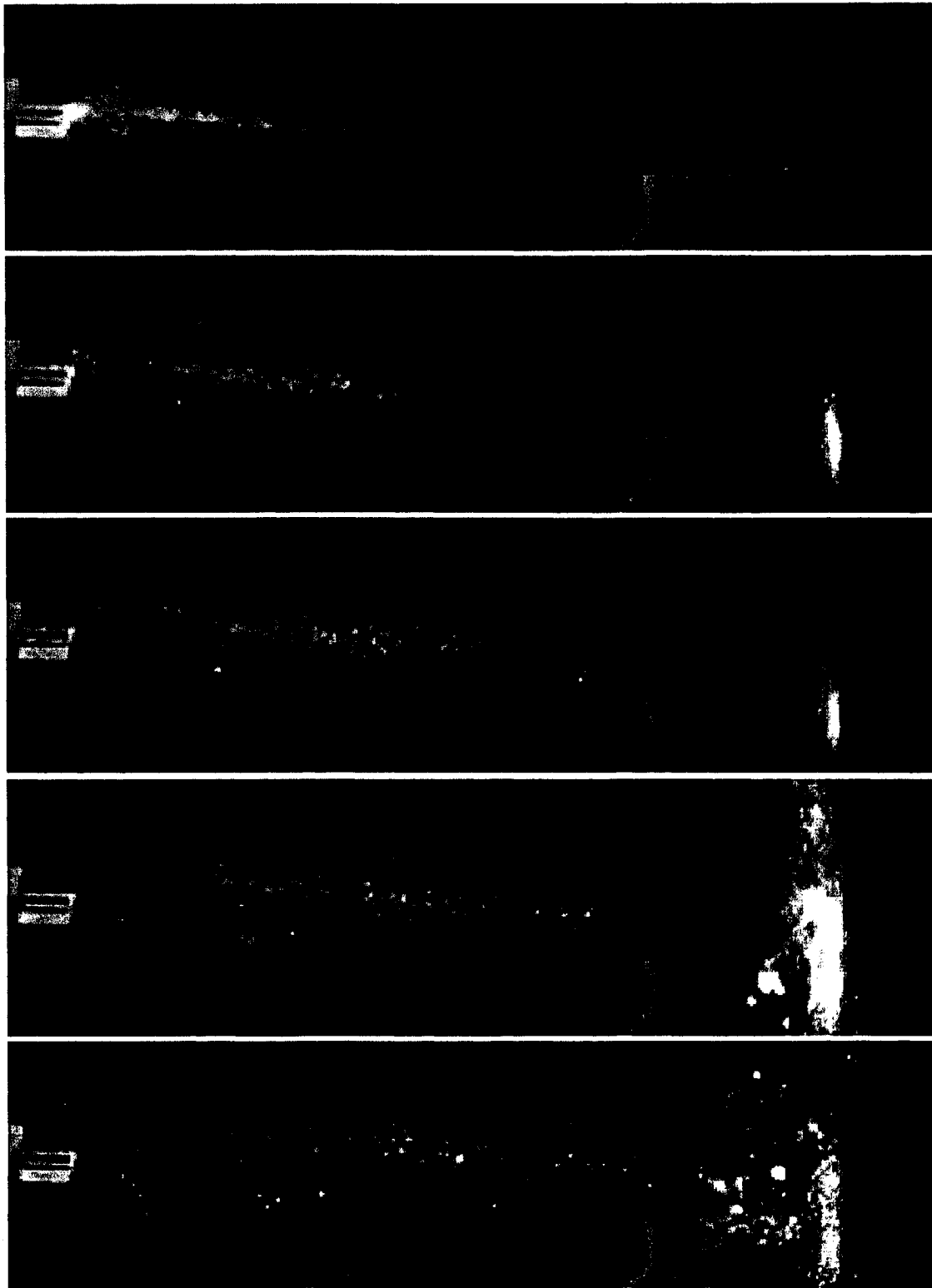


Fig. 4.4-4, Impact of Zirconium 6.4 mm diameter particle at 400 m/s. Time between frames of 1 ms.

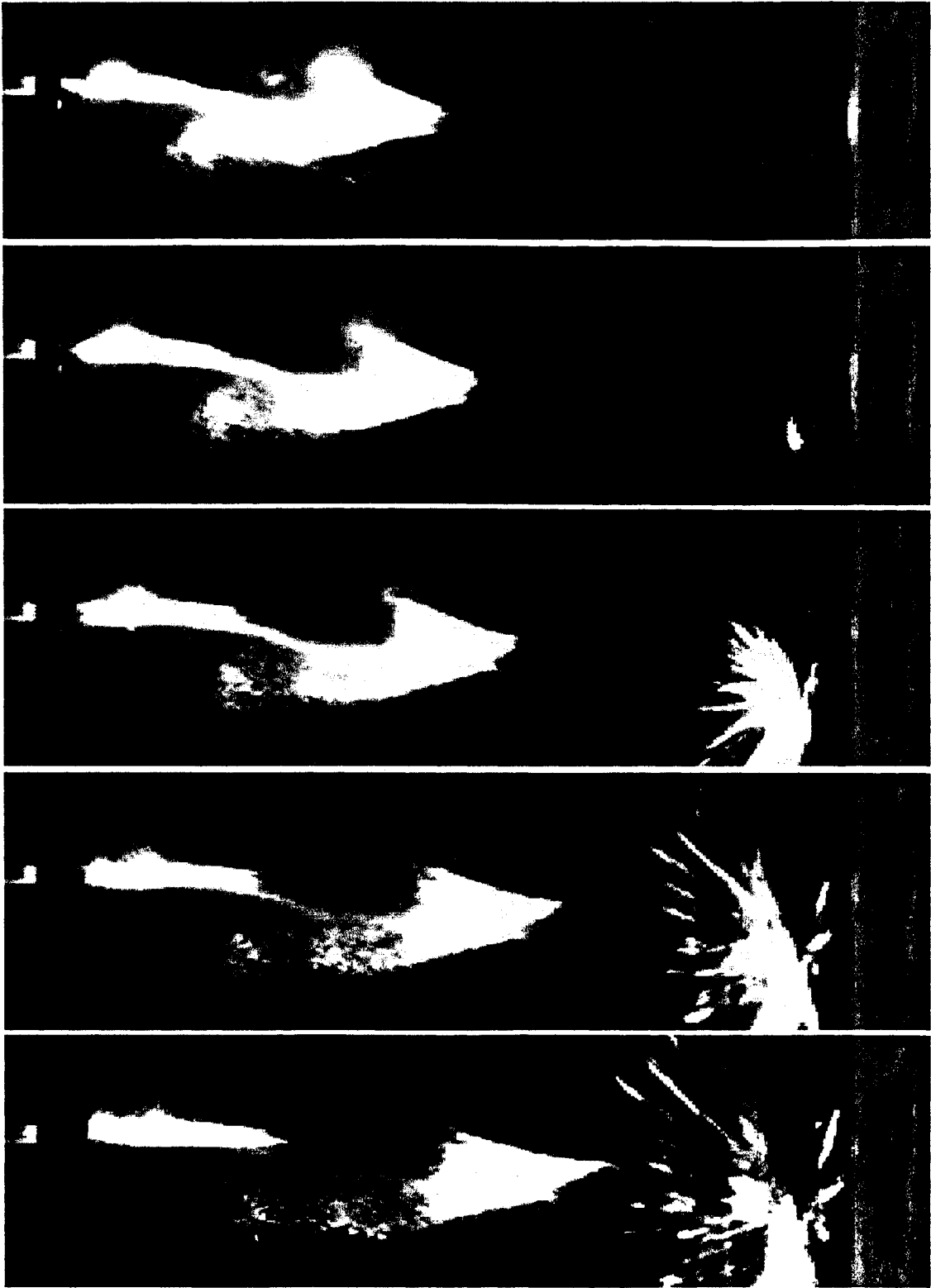


Fig. 4.4-5, Impact of Zirconium 6.4 mm diameter particle at 650 m/s. Time between frames of 0.5 ms.

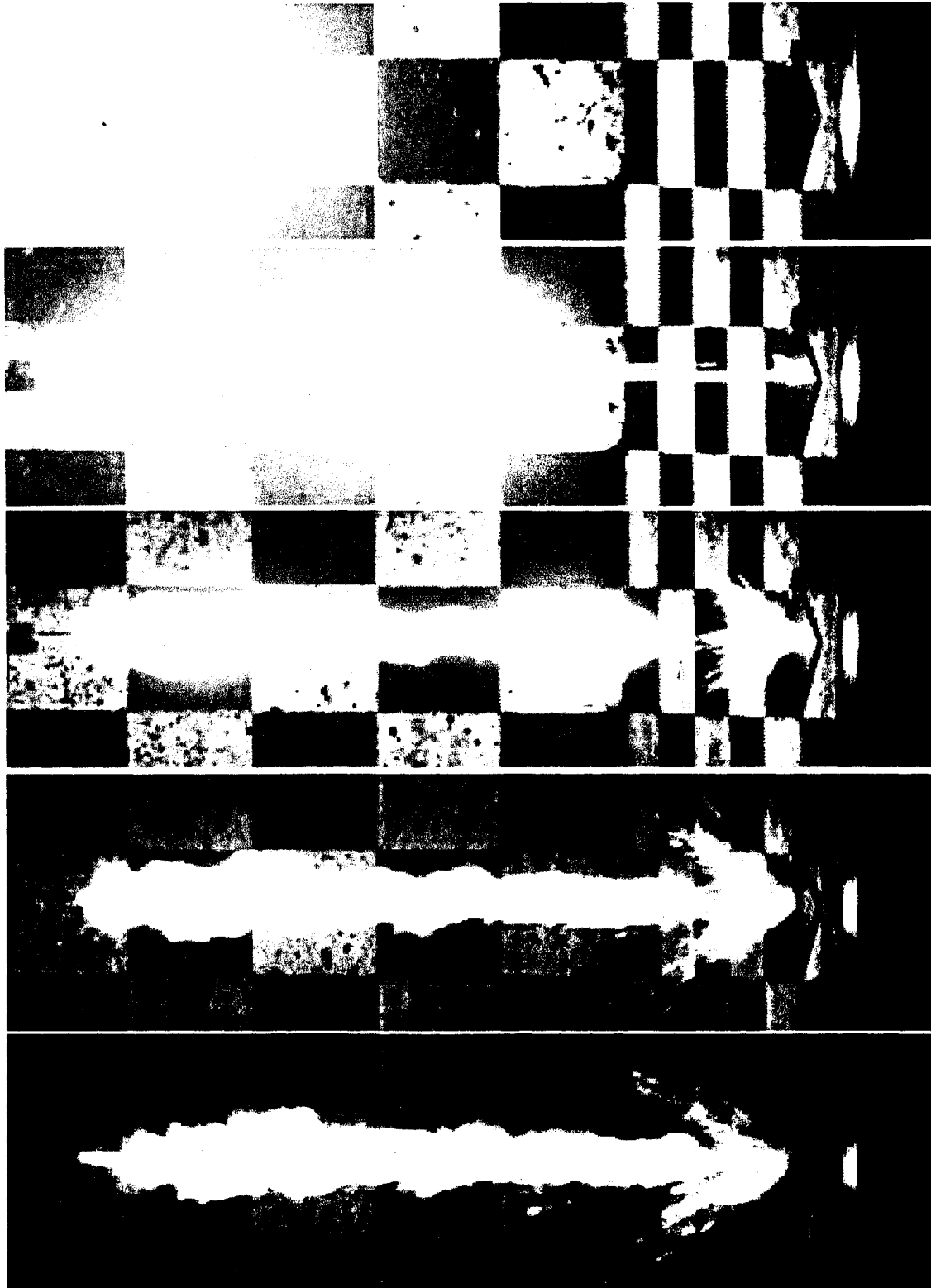


Fig. 4.4-6, Impact of Zirconium 6.4 mm diameter particle at 2500 m/s. Time between frames of 0.5 ms.

4.5 Light-gas Gun Apparatus

The third and final trial series for the completion of this report was performed at the University of Sherbrooke using their Light-gas Gun facility. Professor Martin Brouillette of that University graciously donated his time, facility and expertise in order to successfully complete the trials. The experimental set-up consisted of three independent sections: Driver Section, Driven Section, and Test Section. Figure 4.5-1 that follows is a schematic of the light-gas gun apparatus.

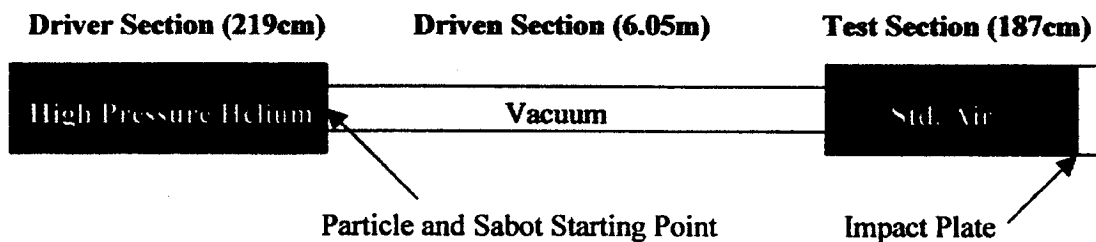


Fig. 4.5-1, Schematic of light-gas gun facility at the University of Sherbrooke.

The Driver Section was a 6.35 cm outer diameter steel tube with a 3.81 cm inner diameter. At a length of 219 cm, the tube was tested with static gauge pressures of up to 10.5 MPa. A Clippard compressed air pneumatic plunger was also installed in



Fig. 4.5-2, Driver section of light-gas gun apparatus including pneumatic plunger.

order to puncture the Aluminum diaphragm that separated the Driver and Driven Sections. A compressed air pneumatic damper was also installed but was not used for this particular set of tests. The gas used to pressurize the entire section was high purity helium.

At a length of just over 6.05 m, the Driven Section was a 2.54 cm outer diameter steel tube with an inner diameter of 1.27 cm. The inner surface of the tube was relatively smooth, in order to minimize frictional forces applied to the sabot. The sabots were 1.27 cm diameter Delrin® or Nylon® plugs with an o-ring groove to seal its outer edge within the Driven Section. A small cavity was also machined into the front surface to hold the metal particle. The sabot,



Fig. 4.5-3, Driven section exit with laser diagnostics for the light-gas gun apparatus.

along with a 6.35 mm diameter particle of varying metal composition, was inserted just after the Aluminum diaphragm into the Driven Section and was held in place by a small setscrew. A vacuum pump was also installed to remove the ambient air and drop the pressure within the Driven Section to nearly zero. Obviously, this was done in order to minimize the losses associated with the expansion of the high pressure Driver Section and to maximize the attainable velocity of the metal particle. The laser diagnostics were placed at the end of the Driven Section with two individual sensors 10.16 cm and 30.48 cm from the exit point. The sensors consisted of 660-680 nm infrared lasers with 5 mm photo-transistors. As the sabot broke the beam emitted from the laser, the output voltage of each of the transistors would change. A LeCroy oscilloscope recorded the two outputs. The impact velocities were calculated by the temporal difference in the two outputs of given physical separation.

The Test Section of the experimental set-up was a 5.72 cm outer diameter steel tube with an inner diameter of 4.45 cm and a length of 187 cm. The entrance of the Test

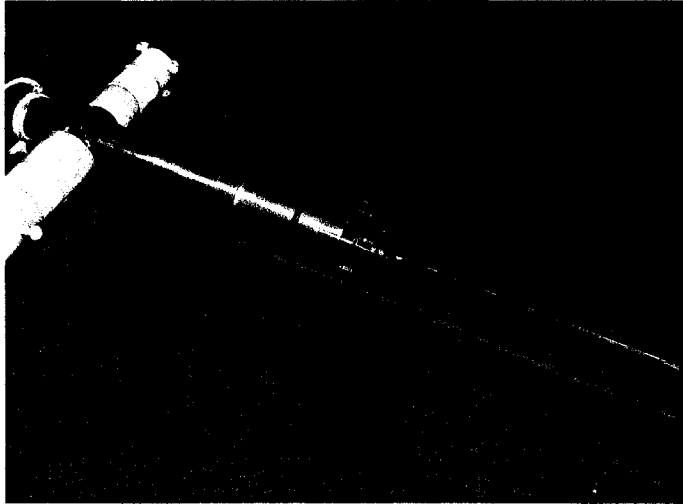


Fig. 4.5-4, Entrance to test section using Plexiglas ® tube instead of Steel.

Section was reduced to a 0.95 cm diameter in order to stop the sabot but allow the metal particle to pass unimpeded. A thin 0.08 mm Mylar ® diaphragm was also inserted to seal the Test Section from the Driven Section. A steel impact plate of 4.45 cm diameter and 5.08 cm in length was inserted at the end of the Test Section.

After each trial the impact plate was removed and replaced with an identical piece in order to investigate the crater created by the impacting particle. The insertion of the impact plate therefore reduced the effective length of the Test Section to 174 cm from Driven Section Exit to impact surface. Note also that the conditions within the Test Section were that of Standard Air at 1 atmosphere of pressure. Figures 4.5-4 and 4.5-

5 are photographs of the experimental set-up with the exception that the steel tube was replaced by a Plexiglas ® in order to visualize the internal components. The Tables that follow are a summary of the relevant trials and their appropriate experimental parameters. Figure 4.5-6 on the following page is a non-dimensional plot of the theoretical exit velocity for various mass and initial pressure conditions.

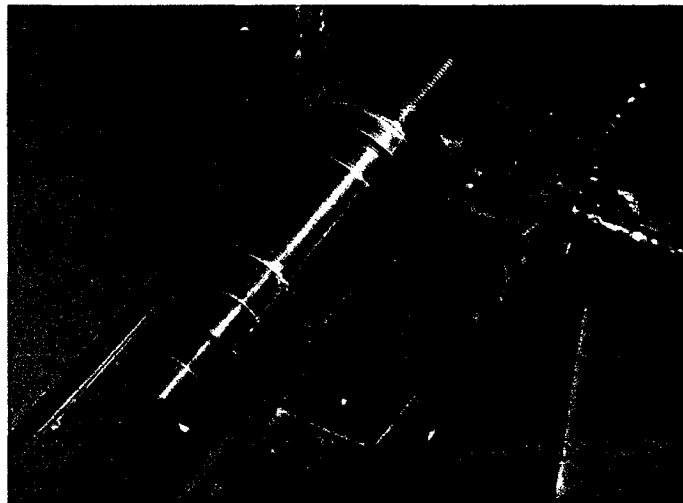


Fig. 4.5-5, Impact plate for the test section with a Plexiglas ® tube instead of Steel.

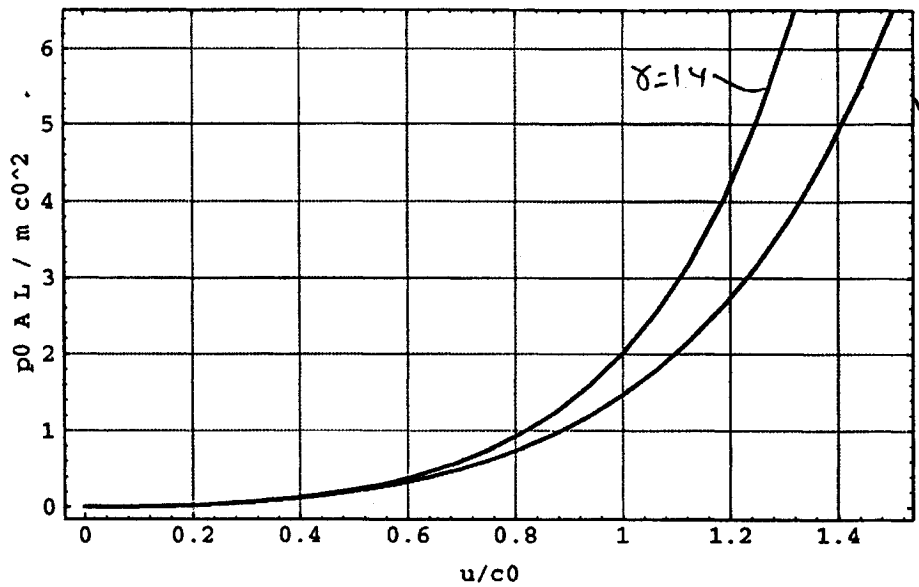


Fig. 4.5-6, Non-dimensional plot of theoretical exit velocity for various mass and initial pressure conditions.

4.6 Light-gas Gun Test Results

Four different materials were tested using the light-gas gun facility at the University of Sherbrooke: Aluminum, Steel, Titanium and Zirconium. The Aluminum particles were manufactured by ALFA AESAR as an 1100 alloy, with an Aluminum-copper mixture of 99+0.12wt.%. Small Parts Inc. produced the steel particles with part number BS-0125-C and batch number BS-2. Both the Titanium and Zirconium particles were machined using modern computer-numerical-control techniques from standard high-purity stock rod. All particles tested had a nominal diameter of 6.35mm.

Steel Particle Results

The steel particles were used in this trial series as a test material to ensure the proper functioning of the light-gas gun. During the four independent trials, the maximum

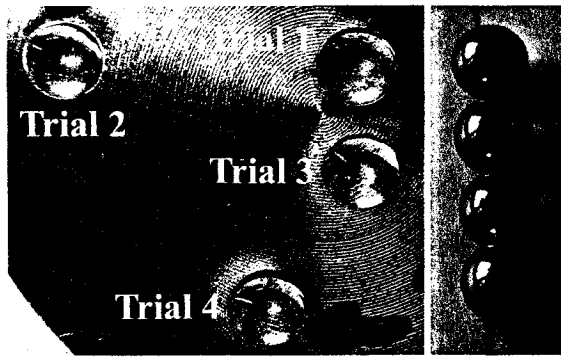


Fig. 4.6-1, Steel particles (right) and resulting craters from impact (left).

impact velocity obtained was 393 m/s. This impact velocity was well below the critical velocity for fragmentation causing only a small deformation of the particle. Closer inspection of Figure 4.6-1 at left clearly shows how imperceptible the deformation of the particles actually was. Even the crater dimensions vary only a small amount from one trial to the

next. This would lead one to believe that the impact events for which no velocity was measured (Trial 1 and 2) occurred under similar conditions to those of the successfully measured trials. Table 4.6-1 below gives a complete summary of the results obtained with the steel particles.

Table 4.6-1, Steel light-gas gun impact results.

Impact Velocity (m/s)	Crater Diameter (mm)	Crater Depth (mm)	Fragmentation	Trial Number
N/A	4.70	0.82	No	UdeS-01
N/A	4.90	0.82	No	UdeS-02
184	4.71	0.81	No	UdeS-03
393	5.11	1.02	No	UdeS-04

Aluminum Particle Results

Five independent trials were performed using Aluminum particles. The most noteworthy result obtained from the Aluminum trials was the determination of the critical velocity for particle fragmentation at approximately 700 ± 100 m/s. The exact number was difficult to determine because of significant noise within the digital signal. The obtained critical velocity (700 ± 100 m/s) was substantially below that of Grady, Kipp and Swegle (1993). Recall, however, that their experiments used thin

PMMA bumper plates, whereas the trial series at hand implemented semi-infinite steel impact plates. It was this difference in impact geometry that accounted for the deviation from their results.

Upon impact with the steel plate, the Aluminum particle yielded a pancake-like shape even at the lowest impact velocities. The Figures that follow clearly demonstrate the flattening of the particle at velocities as low as 391 m/s. The highest impact velocity obtained was 926 m/s and resulted in the particle fragmenting and fusing inside of the impact crater. It should also be noted that even at the highest velocities, the impact crater was almost imperceptible.

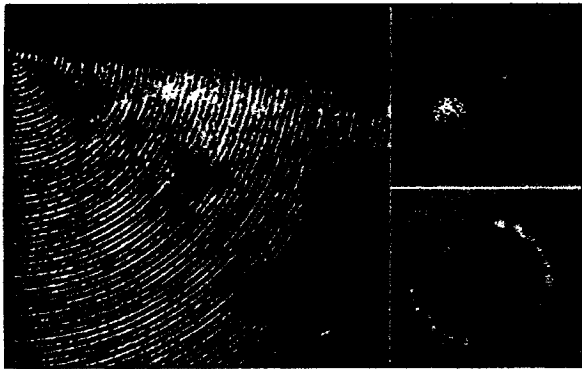


Fig. 4.6-2, Aluminum particle's back surface (top, right), impacting surface (bottom right) and impact crater (left) at a velocity of 391 m/s.

Fig. 4.6-3, Aluminum particle's back surface (top, right), impacting surface (bottom right) and impact crater (left) at a velocity of 455 m/s.

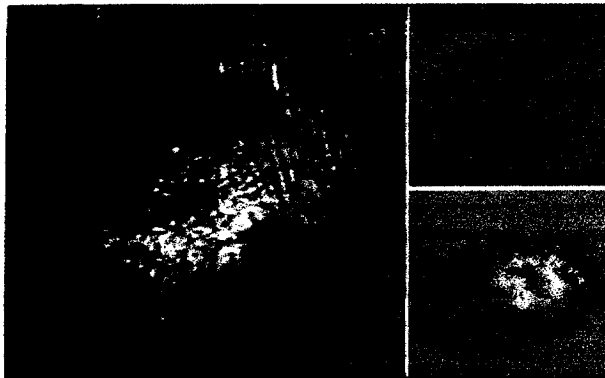


Fig. 4.6-4, Aluminum particle's back surface (top, right), impacting surface (bottom right) and impact crater (left) at a velocity of 588 m/s.

Fig. 4.6-5, Aluminum particle fused to its impact crater at a velocity of 800 m/s.

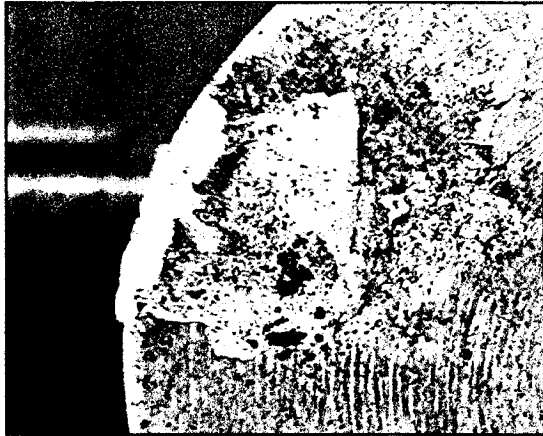


Fig. 4.6-6, Aluminum particle fused to its impact crater at a velocity of 926 m/s.

Table 4.6-2, Aluminum impact experimental data.

Impact Velocity (m/s)	Crater Diameter (mm)	Crater Depth (mm)	Fragmentation	Trial Number
391	7.72	0.00	No	UdeS-28
450*	8.24	0.00	No	UdeS-29
588	8.48	0.10	No	UdeS-30
800*	N/A	N/A	Yes, Fused to Impact Plate	UdeS-31
926	N/A	N/A	Yes, Fused to Impact Plate and White Powder Present	UdeS-27

*Estimated Velocity because of inaccuracies in the obtained digital signals.

Titanium Particle Results

Four trials using Titanium particles were performed. The critical velocity for fragmentation of the particle was determined to be 685 ± 86 m/s. Interestingly, Titanium also fused to the impact crater at the given critical velocity. Only two or three individual pieces were fragmented from the original particle with the largest piece still fused within the impact crater. Again these values differ significantly from those obtained by Grady, Kipp and Swegle (1993) for the same reasons mentioned previously. The Figures that follow clearly illustrate the difference in crater formation below and at the critical velocity for fragmentation.

One should also notice an inherent difference in the deformation path when comparing the sub-critical velocity impacts of Aluminum and Titanium. Recall that for even at the lowest impact velocities, the Aluminum particles deformed severely into pancake-like discs. The same behaviour is absent when the Titanium particles are inspected. Only very minor deformation of the impacting surface is observed, with almost no sign of material yield. However, Figure 4.6-9 on the following page displays a very important phenomenon known as adiabatic shear banding. For the Titanium particles, this phenomenon was only present at velocities slightly below that of critical for fragmentation. The shear bands, clearly visible as rings of material around the impacting surface, were the result of the localization of shear stresses within the material. They were generated by areas of extreme deformation, where locally elevated temperatures and pressures were achieved.



Fig. 4.6-7, Titanium particle deformation (right) and resultant impact crater (left) at a velocity of 360 m/s.

Fig. 4.6-8, Titanium particle deformation (right) and resultant impact crater (left) at a velocity of 434 m/s.

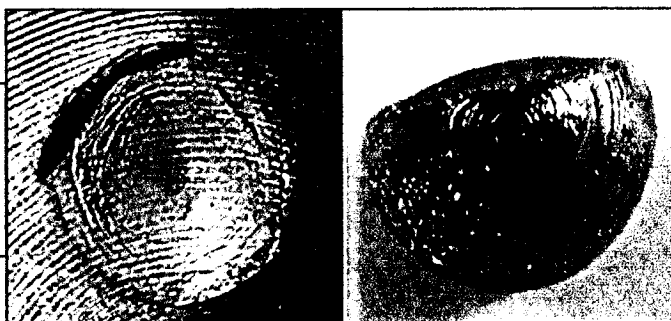


Fig. 4.6-9, Titanium particle deformation through adiabatic shear banding (right) and resultant impact crater (left) at a velocity of 599 m/s.

Fig. 4.6-10, Titanium particle fragmentation (right) and resultant impact crater with fragments fused within the crater itself (left) at a velocity of 772 m/s.

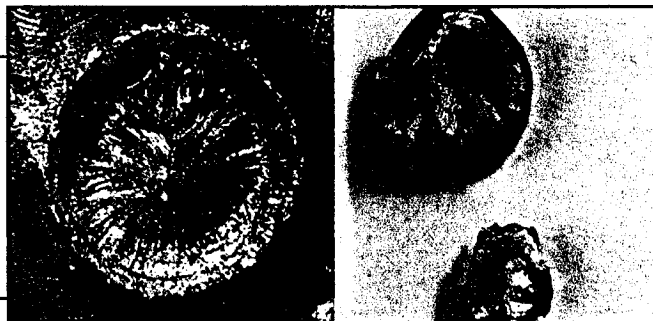


Table 4.6-3, Titanium impact experimental data.

Impact Velocity (m/s)	Crater Diameter (mm)	Crater Depth (mm)	Fragmentation	Trial Number
360	5.00	0.16	No	UdeS-26
434	6.50	0.54	No	UdeS-23
599	8.20	1.00	No	UdeS-22
772	9.66	N/A	2-3 Pieces, 1 Fused to Impact Plate	UdeS-24

Zirconium Particle Results

The final material testing at the University of Sherbrooke light-gas gun facility was Zirconium metal. Twenty independent trials were conducted with seventeen of them yielding usable results. Impact velocities ranging from 55 m/s to over 900 m/s were obtained. Limitations of the facility prevented greater velocities from being tested and a second phase of trials involving video analysis would be ideal. Again, the most important result was the determination of the critical velocity for fragmentation, which for this particular experimental set-up was 561 ± 10 m/s.



Fig. 4.6-11, Cluster fragmentation at impact velocity of 683 m/s (Top) and Diffuse fragmentation at impact velocity of 881 m/s (Bottom) of 6.35 mm diameter Zirconium particles.

Some other very interesting results were obtained from the Zirconium particle impact trial series. Firstly, the three regimes of fragmentation discussed by Grady, Kipp and Swegle (1993) were observed. No fragmentation was present at velocities below 571 m/s. Cluster fragmentation was believed to dominate at velocities between 571 m/s and 862 m/s. Recall that cluster fragmentation is defined as the spalling of material off the rear of the impacting sphere (Grady, Kipp and Swegle, 1993). Analysis of the obtained fragments showed 2-3 fragments were present after the impact event; one piece that impacted the steel plate (top left of Figure 4.6-11) and 1-2 other pieces that spalled off the rear of the sphere (top right of Figure 4.6-11). From the geometry of a

spherical impact, it was relatively straightforward to identify the fragment that was spalled off the rear of the particle and the fragment that impacted with the surface of the steel plate.

Diffuse fragmentation was apparent at velocities greater than 862 m/s. The diffuse fragmentation region was attained when the number of fragments increased and their respective sizes were approximately equal. No individual fragment could be identified as the spalled piece from the rear of the particle. It is believed that at such elevated velocities, the compression waves from the initial impact are severe enough to cause material failure and hence the spalling mechanism is not applicable.

Another interesting feature of the Zirconium trials was the presence of shear bands on the impacting surface. At impact velocities as low as 413 m/s the shear bands became visible as thin yellow-brown circles on the impacting surface of the particle. As the velocity was increased, the discoloration of the impacting surface became more severe. Eventually a blue circle appeared on the outer edge of the particle at an impact velocity of 571 m/s. Note that this velocity was also the extremely close to that of the critical velocity for fragmentation. The same bands were visible on the Titanium particles, except upon fragmentation the discolouration was more flat grey than blue. No shear bands and no discolouration were identified on the Aluminum particles.

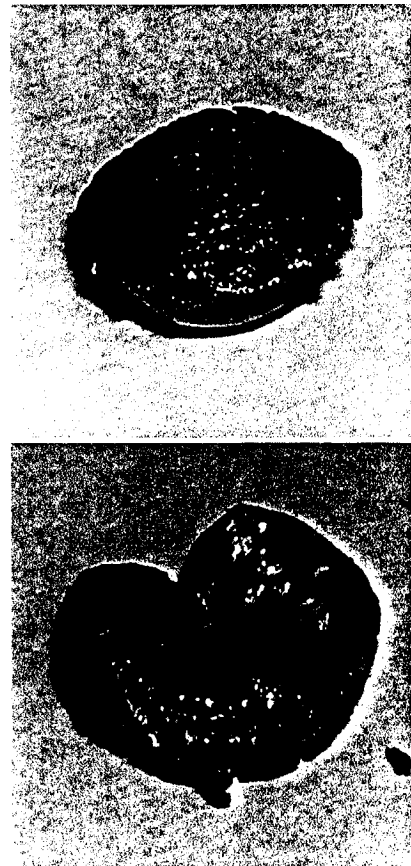


Fig. 4.6-12, Shear banding discoloration at 502 m/s (Top) and 571 m/s (bottom).

Recall that Powers, et al. (1997) described the shear banding process as an increased strain rate near local discontinuities. Localization of that high strain rate resulted in the plastic heating of the material. The thermal heating

phenomenon could be significant because the plastic deformation occurred over a much shorter timescale than that of heat dissipation through conduction, especially for metals like Zirconium with low thermal conductivities. A simple order of magnitude calculation for the deformation timescale and the diffusion timescale can prove the previous statement. Figure 4.6-13 below is a clear illustration of how a

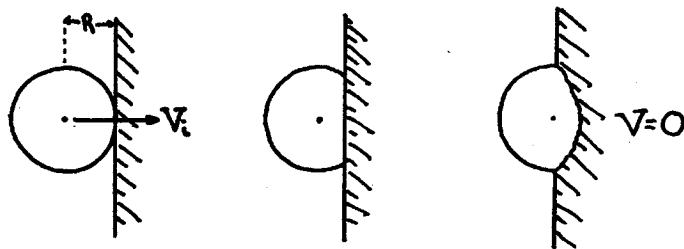


Fig. 4.6-13, Deformation timescale calculation based on initial impact (left), and final deformation distance, R (right).

simplified calculation of the deformation timescale can be conducted. Assuming a total deformation distance equal to the radius of the particle (inspection of the particles after impact trials showed this to be an accurate estimate for

order of magnitude calculations) and knowing the initial impact velocity, one can easily calculate the approximate deformation time as follows (calculations are for Zr at its critical impact velocity):

$$t \approx \frac{R}{V_i/2} \approx \frac{3.18 \times 10^{-3}}{561/2} \approx 11.5 \mu s \quad (4.6-1)$$

A similar order of magnitude calculation was performed for the heat diffusion timescale. Again using the properties of Zr, the timescale was calculated as follows:

$$d_{diffusion} \approx \sqrt{Kt} \quad (4.6-2)$$

$$K = \frac{k}{\rho C_p} \quad (4.6-3)$$

Combining equations (4.6-2 and 4.6-3) yields the following term for the heat diffusion timescale for reactive Zirconium particles with diameters of 6.35mm.

$$t \approx \frac{d_{diffusion}^2}{k / \rho C_p} \approx \frac{(3.18 \times 10^{-3})^2}{22.7 / (6500 \times 270)} \approx 0.78 s \quad (4.6-4)$$

A comparison of the timescales calculated in Equations (4.6-1 and 4.6-4) clearly illustrates on an order of magnitude basis that the heat diffusion timescale is substantially greater than that of the deformation timescale. This result is seconded by the work performed by Powers, *et al.* (1997) that predicted temperatures of over 5000 K within some of the shear bands caused by the huge discrepancies in the deformation and diffusion timescales.

The figures and table that follow are a complete detailing of the results obtained for all of the Zirconium metal impact tests. In all Figures, the photo on the left is the impact crater produced in the steel impact plate and the photo on the right is the resultant deformation and/or fragmentation of the particle after impact. It is important to note that the photos are not to scale. Therefore any dimensional comparisons between the particle and impact crater should be made directly from the photograph.

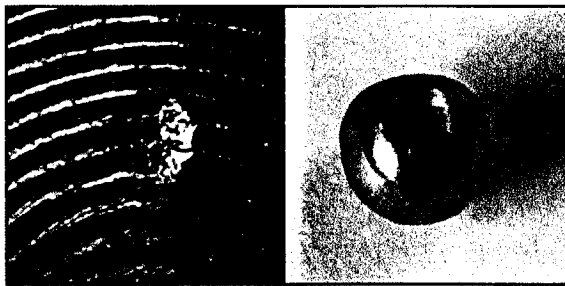


Fig. 4.6-14, Impact crater (left) and particle deformation (right) for Zr particle impact at 55 m/s.

Fig. 4.6-15, Impact crater (left) and particle deformation (right) for Zr particle impact at 300 m/s.

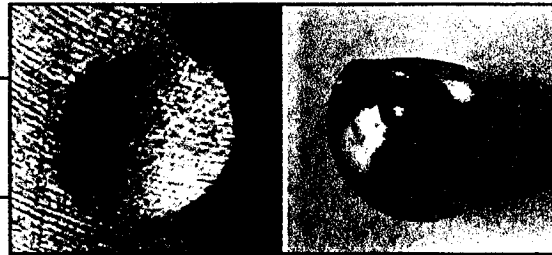


Fig. 4.6-16, Impact crater (left) and particle deformation (right) for Zr particle impact at 325 m/s.

Fig. 4.6-17, Impact crater (left) and particle deformation (right) for Zr particle impact at 413 m/s.

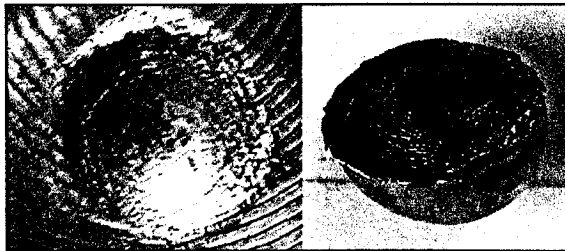
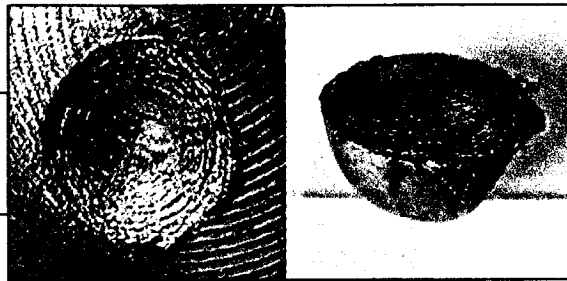


Fig. 4.6-18, Impact crater (left) and particle deformation (right) for Zr particle impact at 418 m/s.

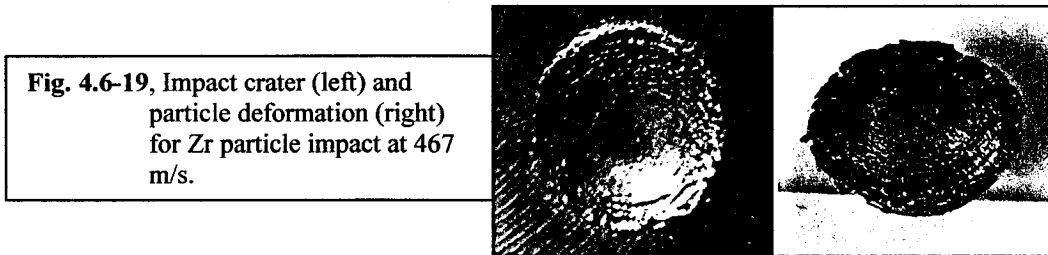


Fig. 4.6-19, Impact crater (left) and particle deformation (right) for Zr particle impact at 467 m/s.

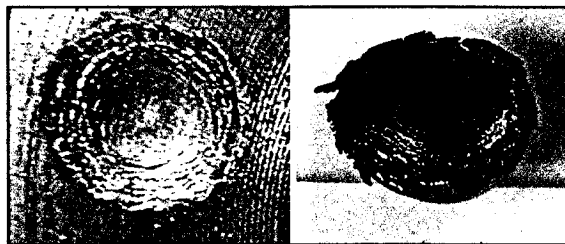


Fig. 4.6-20, Impact crater (left) and particle deformation (right) for Zr particle impact at 472 m/s.

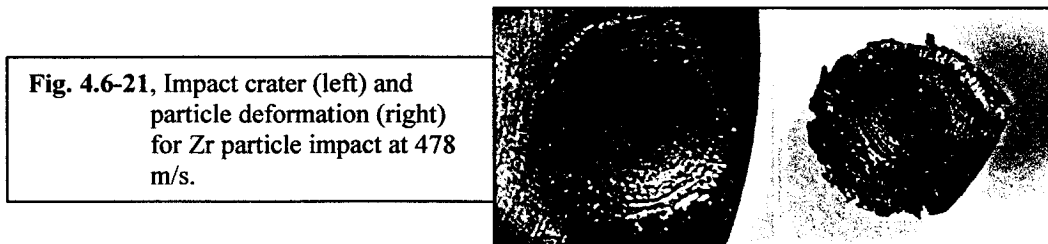


Fig. 4.6-21, Impact crater (left) and particle deformation (right) for Zr particle impact at 478 m/s.



Fig. 4.6-22, Impact crater (left) and particle deformation (right) for Zr particle impact at 502 m/s.

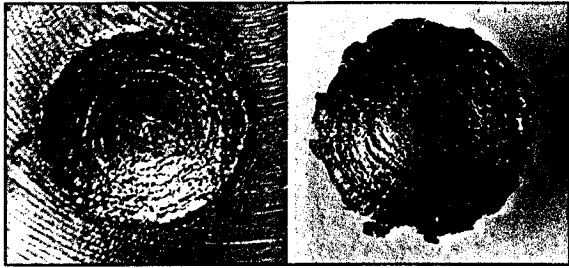


Fig. 4.6-23, Impact crater (left) and particle deformation (right) for Zr particle impact at 545 m/s.

Fig. 4.6-24, Impact crater (left) and particle deformation (right) for Zr particle impact at 551 m/s.

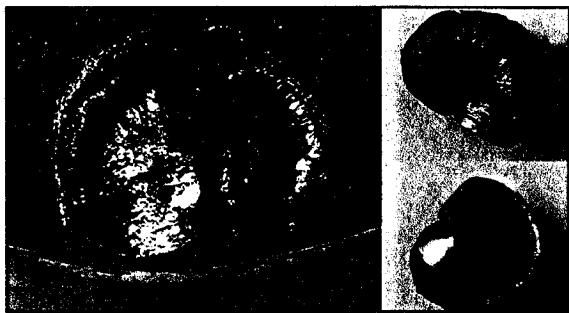
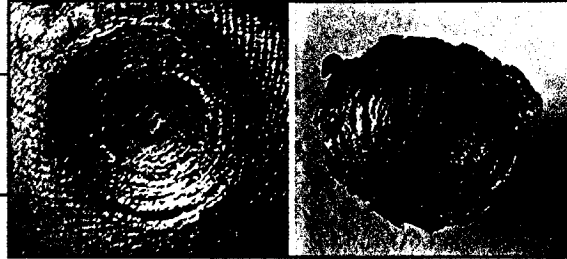


Fig. 4.6-25, Impact crater (left), inside surface of fragmented particle (top, right) and back surface of particle (bottom, right) for Zr particle impact at 571 m/s.

Fig. 4.6-26, Impact crater (left) and particle fragmentation (right) for Zr particle impact at 683 m/s.

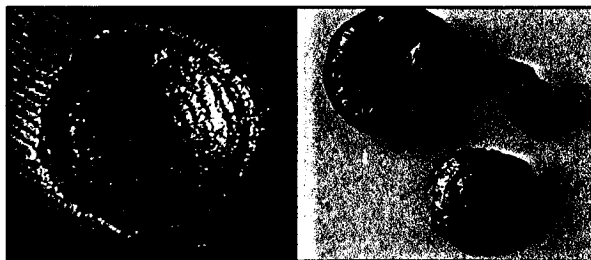
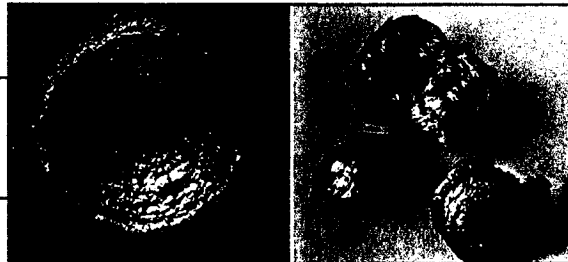


Fig. 4.6-27, Impact crater (left) and particle fragmentation (right) for Zr particle impact at 755 m/s.

Fig. 4.6-28, Impact crater (left) and particle fragmentation (right) for Zr particle impact at 833 m/s.





Fig. 4.6-29, Impact crater (left) and particle fragmentation (right) for Zr particle impact at 862 m/s.

Fig. 4.6-30, Impact crater (left) and particle fragmentation (right) for Zr particle impact at 881 m/s.

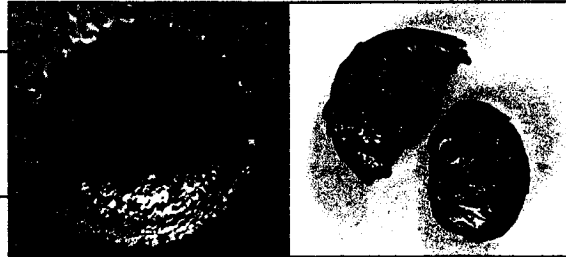


Fig. 4.6-31, Impact crater (left) and particle fragmentation (right) for Zr particle impact at approximately 900 m/s.



Fig. 4.6-32, Impact crater (left) and particle fragmentation (right) for Zr particle impact of greater than 900 m/s.



Table 4.6-4, Zirconium impact experimental data.

Impact Velocity (m/s)	Crater Diameter (mm)	Crater Depth (mm)	Fragmentation	Trial Number
55	2.32	0.00	No	UdeS-08
300*	5.60	0.30	No	UdeS-06
325	5.80	0.42	No	UdeS-16
413	7.46	0.88	No	UdeS-09
418	7.70	0.76	No	UdeS-20
467	7.74	1.00	No	UdeS-13
472	7.00	0.82	No	UdeS-05
478	7.46	1.08	No	UdeS-11
502	8.00	1.32	No	UdeS-12
545	8.90	1.56	No	UdeS-14
551	8.88	1.52	No	UdeS-21
571	9.00	N/A	2-3 Pieces, 1 Fused to Impact Plate	UdeS-10
683	10.54	2.30	2-3 Pieces	UdeS-18
755	10.68	2.40	2-3 Pieces	UdeS-15
833	11.88	3.58	2-3 Pieces	UdeS-19
862	12.22	3.32	5-6 Pieces	UdeS-07
881	12.00	3.44	5-6 Pieces, Soot Coating on Impact Plate	UdeS-17
900*	12.00	3.30	5-6 Pieces, Soot Coating on Impact Plate	UdeS-33
>900*	12.90	4.40	5-6 Pieces, Soot Coating on Impact Plate	UdeS-34

*Estimated velocity because of inaccuracies in the obtained digital signals.

5.0 Discussion

Before discussing the obtained results it is important to review the primary objectives of this report. Recalling the experimental and theoretical work performed by Zhang, et al. (2001) and Frost, et al. (2001), it was hypothesized that the explosive dispersal of reactive particles with relatively large diameters could fragment upon impact. The partially molten projectiles could see a dramatic increase in surface area upon fragmentation of the outer liquid layer and/ or solid kernel. A larger reactive surface area would yield a substantially greater energy release and hence demonstrate an increased loading on nearby structures. Again, the entire hypothesis is based on the assumptions that particle fragmentation occurs upon impact and that the entire energy release process occurs rapidly enough to influence the local thermodynamic conditions.

The simplest way to begin the analysis of the above hypothesis was to examine the peak overpressures and positive phase impulses generated by the blast. Work discussed previously in this report with regards to the characterization of blast propagation should remind one of the important roles played by these two parameters. Not only do they accurately describe the history of an explosive reaction but they are also experimentally simple to obtain. The lollipop gauges recorded the pressure signals at specific distances and the impulses were obtained by the integration of the positive phase of that same signal. When plotted as functions of the distance, a blast history was provided and the complete characterization of the explosive event was achieved. The above technique yielded substantial indirect evidence that was the first major experimental data to lend weight to the hypothesis presented in the introductory section of this report.

The first piece of indirect evidence was the general profile of the pressure decay when comparing Zirconium and ALEX trials (See Figure 4.2-1). The overall nature of the ALEX pressure decay was qualitatively similar to a homogeneous explosive. This

implies that the small ALEX particles equilibrate quickly within the flow field and never penetrate the shock front. The Zirconium pressure decay clearly mimicked that of the heterogeneous steel packed bed charges. Thus a strong interaction between the particles and detonation products can be assumed with the particles penetrating the shock front within the near field. This differentiation between the particle and shock front interaction for ALEX and Zirconium charges is important in that it qualitatively explains the particle dispersion mechanism for each charge set-up.

The differences in impulsive loading, and more specifically the reflected impulsive loading for ALEX and Zirconium charges was the next piece of indirect evidence that supports the notion of an alteration of the thermodynamic conditions upon particle fragmentation (See Figure 4.2-2). Even though the ALEX trials developed substantially higher peak overpressures, the Zirconium trials yielded greater positive phase pressure impulses. The reflected impulses exaggerated the difference because of particle fragmentation upon impact with the reflective plate. Coupled with the profile of the pressure decay described previously, the impulse data adds greater weight to the given hypothesis.

The cantilever trials were also instrumental in that they produced even more indirect evidence that supports the notion of an increased impulsive loading caused by the fragmentation of reactive Zirconium particles. The lack of impact craters on the gauge surfaces and the presence of a Zirconia powder both helped link the fragmentation of the particles to the increased loading phenomenon (See Figures 4.2-3 and 4.2-4).

Previous work by Frost, *et al.* (2001), explained that the total impulse applied to the gauges could be divided into three distinct categories: particle impact, aerodynamic drag and reflected blast wave impulses. At a particular location in the mid-field an estimated seventy percent of the total impulse was the result of particle impact, with the rest of the loading being caused by the reflected blast wave and the aerodynamic drag. However, a fourth category of impulse loading phenomenon was present during

the impact of the larger mass Zirconium particles. The fourth category was believed to be the fragmentation of the particles and the subsequent increase in energy release caused by the dramatic rise in reactive surface area.

The explosive gun-barrel tests were also an essential component of the performed research work. The most important piece of information that was deduced from the trial series was that the ignition of millimetre sized Zirconium particles was in fact possible. Furthermore, high-speed video of the impact event showed an almost instantaneous ignition of the inner solid kernel upon impact with the steel plate.

The light-gas gun trial series was the most fundamental in nature of the three experiments performed for the completion of this report. The objective of the work was to describe the underlying mechanism of fragmentation for non-combusting metal particles as an obvious stepping-stone towards characterizing the fracture and fragmentation mechanism for burning particles.

Qualitatively, the results obtained for Aluminum and Titanium particle impacts with a semi-infinite steel plate correlated reasonably well with those obtained by Grady, Kipp and Swegle (1993) for bumper plate impacts. Recall that the quantitative differences in the values obtained for the critical velocity inducing fragmentation were easily explained by the varying impact geometry. Table 5.0-1 that follows is a summary of the relevant data obtained during the University of Sherbrooke trial series.

Some very fundamental behaviour can be inferred with a closer examination of the results when combined with some of the theory presented in the literature review section of this report. The second line of Table 5.0-1 calculates the theoretical spall strength of the three relevant materials using the Lawn and Wilshaw (1975) model involving the bulk modulus of the respective metal (See Equation 3.3-1). Although simplistic in nature, the model qualitatively compares the spall strengths of Aluminum, Titanium and Zirconium.

The before last line of Table 5.0-1 clearly displays the Hugoniot pressure values developed during the impact process. Using Equation (3.4-1), the appropriate pressure values were obtained by use of the respective shock impedances (material density multiplied by the sound speed) and the critical impact velocity inducing particle fragmentation. Note that the density of steel was given as 7870 kg/m³ and the sound speed approximated at 4512 m/s. Interestingly, the Hugoniot pressures developed at each of the respective critical conditions were quantitatively very similar.

Table 5.0-1, Summary of impact test calculations.

	Aluminum	Titanium	Zirconium
B_0 (GPa)	72.2 ⁽²⁾	105 ⁽²⁾	89 ⁽³⁾
P_{th} (GPa) ⁽⁴⁾	22.98	33.42	28.33
C_0 (m/s) ⁽³⁾	6420	4140	3800
ρ (kg/m ³) ⁽³⁾	2700	4850	6500
C_p (J/Kg K) ⁽⁶⁾	900	590	270
Z_s (kg/m ² s)	1.73x10 ⁷	2.01x10 ⁷	2.47x10 ⁷
Z_I (kg/m ² s)	3.55x10 ⁷	3.55x10 ⁷	3.55x10 ⁷
V_I ⁽¹⁾	700±100	685±86	561±10
P_h (GPa) ⁽⁵⁾	8.14	8.79	8.17
κ (W/mK) ⁽³⁾	237	21.9	22.7
K (m ² /s) ⁽⁶⁾	9.75x10 ⁻⁵	7.65x10 ⁻⁶	1.29x10 ⁻⁵

(1) Refers to data obtained at the University of Sherbrooke Facility

(2) Refers to data obtained from Grady and Kipp, 1997.

(3) Refers to data obtained from Goodfellow Industrial Products.

(4) Refers to values obtained using Equation 3.3-1

(5) Refers to values obtained using Equation 3.4-1

(6) Refers to values obtained for Equation 4.6-4

When a comparison of the theoretical spall strengths and Hugoniot pressures developed during the impact event was performed, some interesting observations were made. Firstly, Aluminum was found to have the lowest theoretical spall

strength. Couple that fact with the quantitatively similar Hugoniot impact pressure to Titanium and Zirconium, and one would expect the Aluminum particles would have the lowest critical velocity inducing fragmentation. Experimentation by both Grady and Kipp (1997) and the author of this report yielded dramatically different results. In both cases the opposite was found to be true with Aluminum fragmenting at the greatest critical velocity. When a comparison of Titanium and Zirconium results was performed, the quantitatively similar Hugoniot pressures would lead one to expect the material with the lower theoretical spall strength fragmenting at a lower impact velocity. This expectation was proven to be true experimentally within the scope of the University of Sherbrooke trial series.

The above discrepancies with regards to theoretical spall strength and critical impact velocity inducing fragmentation can most easily be explained by differences in the deformation paths causing the fracture of the particle. A closer look at the thermal conductivity of each of the tested materials would clearly show an order of magnitude difference in the values when comparing Aluminum to both Titanium and Zirconium. Only a relatively small difference (less than 4%) is noted between the thermal conductivities of Titanium and Zirconium. As explained previously in the literature review, work by Power, *et al.* (1997) related the importance of thermal conductivity of a material to the formation of adiabatic shear bands. The trial series at hand clearly demonstrated the different deformation paths for low conductivity metals (deformation through shear banding) and for high conductivity metals (deformation through spall only). Figure 5.0-1 illustrates the shear bands at impact velocities



Fig. 5.0-1, Shear banding for Titanium at 599m/s (left) and Zirconium at 551 m/s (middle). Lack of such bands for Aluminum at 588 m/s (right).

slightly below critical for Titanium and Zirconium, and the obvious lack of such banding for Aluminum particle impacts.

Evidence from the previous photographs coupled with the results from Table 5.0-1 lead one to believe that the shear banding, and more specifically the thermal heating phenomenon associated with the banding process, is the root cause of fragmentation for low thermal conductivity metals. The discolouration of the metal particles upon impact is caused by the thermal stressing of the material during plastic deformation. The thermal softening of the material may also explain the significantly lower values for critical velocity obtained with semi-infinite impact plates when compared with bumper plate critical conditions. This implies that the thermal conductivity of a metal, as well as the yield strength and fracture toughness, is an extremely important material property when studying the dynamic fragmentation mechanism.

6.0 Conclusions

The three different trial series performed for the completion of this report have yielded some extremely important conclusions. The different series, although independent in nature, can all be linked together in order to explain the overall phenomenon of blast wave augmentation in the near-field by the dispersal, impact and subsequent fragmentation of reactive Zirconium particles with small scale structures.

The Light-gas gun trial series established the critical velocity for fragmentation of non-burning Zirconium, Titanium and Aluminum particles. Their respective critical velocities were 561 ± 10 m/s, 685 ± 86 m/s and 700 ± 100 m/s. The experiments also displayed the importance of thermal stresses associated with shear banding and linked the thermal conductivity of the impacting material with its overall resistance to fragmentation. Obviously, a continuation of this work would be necessary in order to completely characterize the shear banding phenomena and its overall effect on other material properties.

The explosive acceleration trials proved that the ignition of millimetre-sized Zirconium particles was in fact possible. The trial series also established that the reactive burning particles were comprised of a thin liquid outer layer and an inner solid kernel. The critical velocity for the fragmentation of the burning Zirconium particle was also established in that all impacts at velocities greater than 150 m/s led to the fragmentation of the particle. Furthermore, video footage showed that the burning of the fragmented pieces ignited and burned instantaneously and could affect the overall thermodynamic conditions of the flow field. It also showed that the secondary fragmentation during subsequent impact events could yield even greater reactive surface area.

The most extensive series of trials involving the explosive dispersal of reactive particles yielded the most exciting results. Combined with the conclusions drawn from the explosive acceleration trials, the cantilever gauge data proved that the Zirconium particles did in fact fragment upon impact with small-scale structures. The lack of impact craters, the Zirconia powder on the gauge surface and a critical velocity for fragmentation below the calculated velocity of the particles at the given gauge distances all go towards proving that the Zirconium particles do fragment upon impact with the gauges. Theoretical calculations also showed that a fourth category of impulse was present during the loading of the gauges. The inertial characteristics, along with the reflected blast and aerodynamic drag, could not account entirely for the discrepancies in impulse data obtained by both the cantilever and pressure gauges. Therefore, it was concluded that the augmentation of the blast wave was caused by the fragmentation of the Zirconium particles. The fragmentation resulted in an increased reactive surface area, which in turn allowed for a greater energy release during the combustion process. Video obtained during the explosive acceleration trials visually displayed the entire process. This entire mechanism resulted in an alteration of the flow field's thermodynamic state and augmented the blast wave within the near-field. Therefore, it was concluded that the impact and fragmentation of reactive Zirconium particles on small-scale structures does augment the blast wave within the near-field.

7.0 References

- Allen, B.C. (1972). *Liquid Metals*. New York: Marcel Dekker, p.161-212.
- Ang, J.A. (1990). *Int. Jour. Impact Engng.* (10):23-33.
- Bach, G.G. and Lee, J.H.S. (1970). *An Analytical Solution for Blast Waves*. AAIA Journal: 8(2), pp271-275.
- Baker, W.E. (1973). *Explosions in Air*. University Texas Press: p.158-160.
- Beyer, R.T., and Ring, E.M. (1972). *Liquid Metals*. New York: Marcel Dekker, p.431-460.
- Brandon, D.G., et al. (1984). *Mechanical Properties at High Rates of Strain*. The Institute of Physics, Bristol and London, p.261-268.
- Brown, G.I. (1998). *The Big Bang: A history of explosives*. Thrupp: Sutton Publishing.
- Brown, L.M., and Embury, J.D. (1973). *Proc. 3rd Int. Conf. Of Strength of Metals and Alloys*. P.164.
- Brzustowski, T.A. and Glassman, I. (1960). *Heterogeneous Combustion*. Princeton: Princeton University. P.41-74.
- Christy, S. and Pak, H. (1986). *Metallurgical Applications of Shock Wave and High Strain Rate Phenomena*. New York: Marcel Dekker, p.835-863.
- Curran, D.R., et al. (1977). *Phys. Today* (30):46.
- Curran, D.R. (1982). *Impact Dynamics*. P 333-366. New York: Wiley-InterScience.
- Curry, D.A., and Knott, J.F. (1979). *Metall. Sci.* (13):341.
- Davison, L. Graham, R.A. (1979). *Phys. Rept.* (55):257.
- Englman, R., et al. (1987). *Phil. Mag. B.* (56):751.
- Fassell, W.M. and Papp, C.A. (1960). *ARS Progress in Astronautics and Rocketry: Solid Propellant Rocket Research*. (I):259-270.
- Filler, W.S. (1976). *The Influence of Reactive Cases on Air-blast: an Experimental Study*. Proc. 6th Detonation Symposium. P.777-785.

- Filler, W.S. (1985). *The Influence of Reactive Cases on Air-blast from High Explosives*. Proc. 8th Detonation Symposium. P.207-210.
- Follansb ee, P.S., et al. (1984). *Mechanical Properties at High Rate of Strain*. The Institute of Physics, Bristol and London, p.71-80.
- Frost, D.L., et. al. (2001). *Near-Field Impulse Effects from Detonation of Heterogeneous Explosive*. Shock Compression of Condensed Matter.
- Frost, D.L., et al. (2002). *Critical Conditions for the Ignition of Metal Particles in a Condensed Explosive*. Proc. 12th Detonation Symposium.
- Frost, D.L., and Zhang, F. (2003a). *Effect of Scale on the Blast Wave Generated by a Metallized Heterogeneous Explosive*. 34th Proceedings of the International Conference of ICT on Energetic Materials.
- Frost, D.L., et al. (2003b). *Fragmentation of Reactive Metallic Particles During Impact with a Plate*. APS Topical Conference on Shock Compression of Condensed Matter.
- Glassman, I (1996). *Combustion, 3rd Edition*. Orlando: Academic Press (9).
- Glenn, L.A., Chudnovsky, A. (1986). *Jour. Appl. Phys.* (59):1379-1380.
- Goodfellow Industrial Products. www.goodfellow.com. Feb 2nd, 2004.
- Goods, S.H. and Brown, L.M. (1979). *Acta. Metall.* (27):1.
- Gordon, D.A. (1960). *ARS Progress in Astronautics and Rocketry: Solid Propellant Rocket Research*. (I):271-278.
- Grady, D.E. (1982). *Jour. Appl. Phys.* (53):322.
- Grady, D.E., Kipp, M.E. (1985). *Mech. Mat.* (4):311.
- Grady, D.E. (1988). *The Spall Strength of Condensed Matter*. *Jour. Mech. Phys. Solids* (36):3, pp353-384.
- Grady, D.E., Kipp, M.E., and Swegle, J.W. (1993). *Jour. Imp. Engng.* (14):427-438.
- Grady, D.E., and Kipp, M.E. (1995). *Int. Jour. Solids & Structures*.(32):2779-2791.
- Grady, D.E., and Kipp, M.E. (1997). *Int. Jour. Impact Engng.* (20):293-308.
- Gurson, A.L. (1977). *Jour. Engng. Mater Tech.* (99):2.
- Higgins, A.J., et al. (2001). *Combustion of Supersonic Metallic Spheres*. *Proc. of the 18th International Colloquium on the Dynamics of Explosive and Reactive Systems*. July 29-Aug 1, 2001. ISBN#0-9711740-0-08.

- Kurbangalina, R.K.H. (1969). *Critical Diameter of Liquid Explosives as a Function of Powder Content*. Zhurnal Prikladnoi Mekhaniki I Tekhnicheskoi Fiziki. 10(4): 133-136.
- Lanovets, V.S., et al. (1991). *Dispersion of the Detonation Products of a Condensed Explosive with Solid Inclusions*. Fizika Goreniya I Vzryva. 29:88-02.
- Lawn, B.R., Wilshaw, T.R. (1975). *Fracture of Brittle Solids*. Cambridge: Cambridge University Press.
- Lee, J.J., et al. (1995a). *Propagation of Nitromethane Detonation in Porous Media*. Shock Waves. 5:115-119.
- Lee, J.J., et al. (1995b). *Effect of DETA Sensitization on Detonation of Nitromethane in Porous Media*. Combustion and Flame. 100:292.
- Lee, J.J. (1997). *Detonation Mechanisms in a Condensed-Phase Porous Explosive*. PhD Thesis, McGill University: Montreal.
- Meyer, M.A., Aimone, C.T. (1983). *Prog. Mat. Sci.* (28):1.
- Murr, L.E. (1981). *Shock Waves and High Strain Rate Phenomena in Metals*. New York: Plenum Press, p.607-673.
- Orowan, E. (1949). *Rep. Prog. Phys.* (12):185.
- Orowan, E. (1970). *Proc. Roy. Soc. Lond. A* (316):473.
- Powers, J.M., et al. (1997). *Investigation of Reactive Shear Localization in Energetic Solids*. Combustion Science and Technology. April 1998.
- Rinehart, J.S. (1950). *Popular Astronomy*. (58):458.
- Rinehart, J.S., and White, W.C. (1952). *Am. J. Phys.* (20):14.
- Rose, J.H., et al. (1984). *Phys. Rev. B*. (29):2963.
- Shockey, D.A., et al. (1973). *Metallurgical Effects at High Strain Rates*. P 473-499. New York: Plenum Press.
- Thucydides (1954). *History of the Peloponnesian War*. Transcript from Rex Warner. New York: Penguin Books. P.172
- Tvergaard, V. and Needleman, A. (1984). *Acta. Metall.* (32):157.
- Von Grosse, A.V. and Conway, J.B. (1958). *Combustion of Metals in Oxygen*. *Ind. Engng. Chem.* 50:663-672.

- Wood, W.A. (1960). *ARS Progress in Astronautics and Rocketry: Solid Propellant Rocket Research*. (I):281-291.
- Wright, T.M. (2002). *The Physics and Mathematics of Adiabatic Shear Bands*. Cambridge University Press.
- Yetter, R.A. and Dryer, F.L. (2001). *Microgravity Combustion: Fire in Free Fall*. New York: Academic Press (6):419-478.
- Zhang, F., Frost, D.L., *et al.* (2001). *Explosive Dispersal of Solid Particles*. *Shock Waves* (10): 431-443.

Appendix A

Section I: Complete Dispersal Experimental Data

A.I Complete Data Tables for Dispersal Experiments

Table A.I-1, Complete Zirconium experimental pressure and impulse data

Trial Number	Gauge (cm)	Pressure (MPa)	Impulse (Pa-s)
2000-16	60	1.65	225.75
	90	1.06	177.45
	120	1.11	161.79
	150	0.65	126.53
	190	0.30	117.63
Reflective	120	2.40	456.69
2000-20	60	2.35	N/a
	90	1.24	180.17
	120	0.89	304.06
	150	0.41	138.84
	190	0.30	112.18
Reflective	90	5.75	604.77
2000-27	60	3.35	416.42
	90	1.93	176.41
	120	0.77	128.78
	150	0.52	151.52
	190	0.23	113.74
Reflective	90	8.27	607.26
2000-31	60	1.60	205.95
	90	0.82	208.26
	120	0.65	145.06
	150	0.64	212.69
	190	0.40	192.03
Reflective	60	6.86	784.70
2000-32	60	2.48	248.05
	90	1.59	180.73
	120	0.67	139.48
	150	0.50	129.24
	190	0.43	110.79
Reflective	60	6.71	887.03
2001-19	60	2.73	254.66
	90	1.07	291.51
	120	0.97	N/a
	150	0.56	184.75
	190	0.35	122.74
Reflective	190	2.62	214.05

Table A.I-1, Continued

Trial Number	Gauge (cm)	Pressure (MPa)	Impulse (Pa-s)
2001-25	60	2.27	203.73
	90	1.76	153.63
	120	1.29	200.15
	150	0.75	161.65
	190	0.28	118.32
Reflective	150	3.74	325.80
2002-16	60	1.59	212.22
	90	0.85	165.45
	120	0.87	171.56
	150	0.82	157.81
	190	0.65	124.40
Reflective	120	1.09	342.46

Table A.I-2, Complete ALEX experimental pressure and impulse data

Trial Number	Gauge (cm)	Pressure (MPa)	Impulse (P.A-s)
2000-43	60	2.90	199.19
	90	1.69	171.64
	120	1.44	179.34
	150	0.69	142.01
	190	0.27	117.34
Reflective	120	1.15	N/a
2000-46	60	3.70	174.98
	90	0.99	138.90
	120	0.70	N/a
	150	0.95	34.37
	190	N/A	N/a
Reflective	90	N/A	N/a
2000-50	60	2.36	163.08
	90	1.06	159.14
	120	0.51	142.03
	150	0.56	114.25
	190	0.46	n/a
Reflective	60	13.96	763.23
2000-51	60	2.39	186.71
	90	1.62	213.29
	120	0.59	183.41
	150	0.84	136.81
	190	0.36	103.46
Reflective	90	11.36	411.30

Table A.I-2, Continued

Trial Number	Gauge (cm)	Pressure (MPa)	Impulse (Pa-s)
2001-16	60	3.58	136.17
	90	1.83	160.39
	120	N/A	n/a
	150	0.81	107.49
	190	0.31	103.78
	190	1.61	191.91
Reflective			
2001-24	60	2.99	168.85
	90	1.00	160.39
	120	1.86	n/a
	150	0.47	113.82
	190	0.32	98.79
	150	3.46	275.68
Reflective			
2001-31	60	3.82	141.62
	90	2.53	197.81
	120	1.19	n/a
	150	0.69	123.93
	190	0.29	97.79
	120	4.43	n/a
Reflective			
2001-40	60	2.56	147.07
	90	2.45	189.79
	120	3.29	n/a
	150	0.70	111.29
	190	0.32	95.80
	90	8.27	n/a
Reflective			
2001-42	60	1.97	163.41
	90	2.72	152.37
	120	3.08	129.56
	150	0.84	117.61
	190	0.32	n/a
	60	13.08	620.58
Reflective			

Table A.I-3, Complete Steel experimental pressure and impulse data

Trial Number	Gauge (cm)	Pressure (MPa)	Impulse (Pa-s)
2001-21	60	0.44	n/a
	90	0.33	57.09
	120	N/a	n/a
	150	0.12	42.30
	190	0.07	33.47
	190	0.25	50.68
Reflective			

Table A.I-4, Complete Nitromethane experimental pressure and impulse data

Trial Number	Gauge (cm)	Pressure (MPa)	Impulse (Pa-s)
1999-42	60	1.90	120.42
	90	1.19	171.83
	120	0.83	112.07
	150	0.23	94.65
	190	0.11	58.81
	250	0.28	61.16
1999-51	60	2.05	151.38
	90	1.16	145.96
	120	0.93	181.29
	150	0.25	77.26
	190	0.11	74.37
	250	0.39	33.54
1999-54	60	2.07	150.13
	90	0.61	159.70
	120	0.38	134.09
	150	0.21	99.10
	190	0.11	75.24
	250	0.41	65.67

APPENDIX B

Section I: Light-gas Gun Gas Delivery System Specifications

Section II: Light-gas Gun Diagnostics Specifications

B.I Light-gas Gun Design Specifications

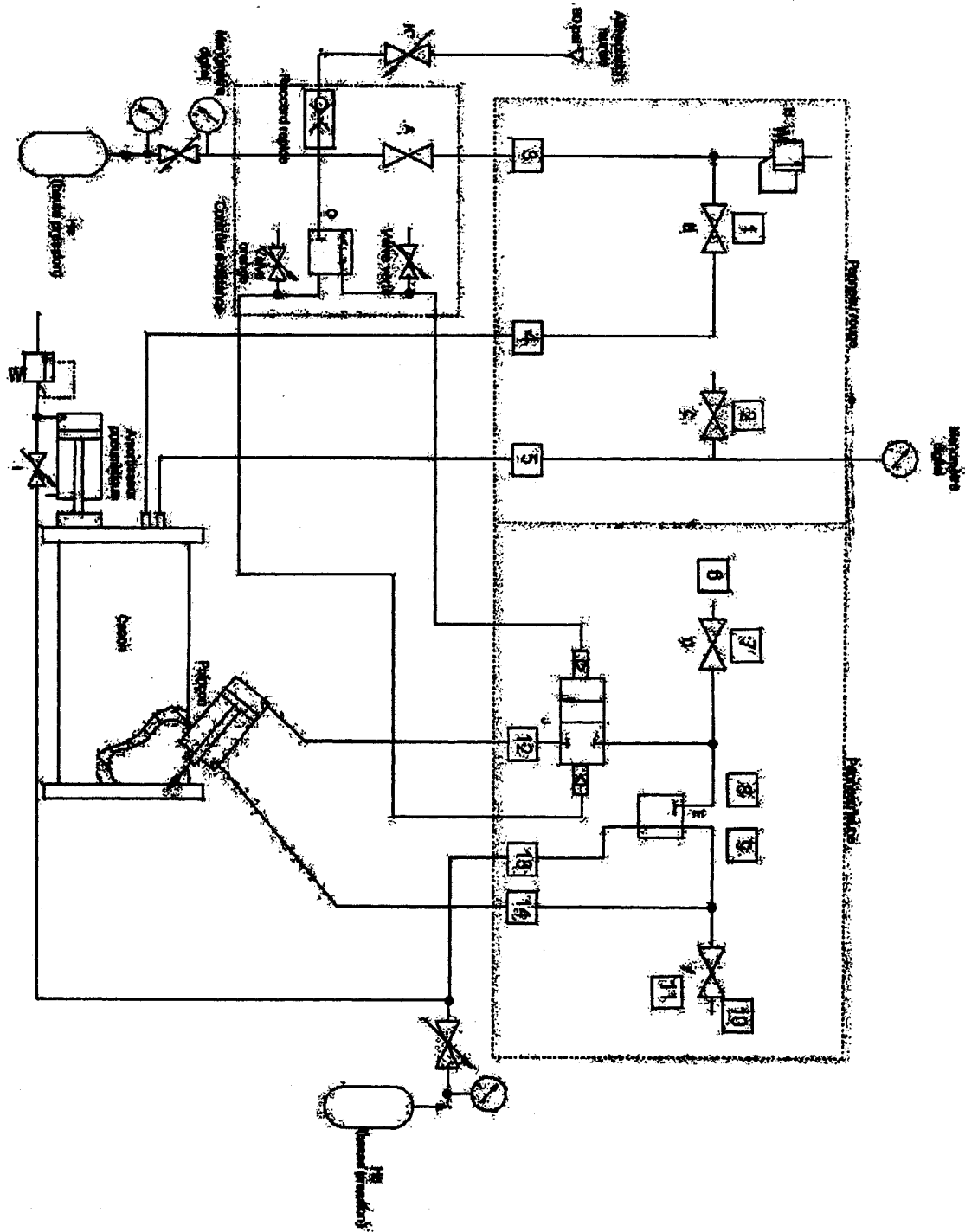
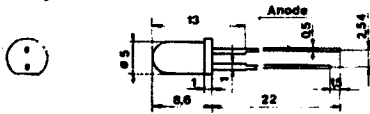


Fig. B.I-1, Schematic of pneumatic system powering driver section and plunger for light-gas gun launch mechanism.

B.II Light-gas Gun Diagnostics Specifications

5 mm PHOTO TRANSISTOR (SILICON)



Part No. KID 7404

ABSOLUTE MAXIMUM RATINGS (25°C unless otherwise noted)

- * Collector Current I_C 25mA
- * Collector-to-Emitter Breakdown Voltage 30V
- * Emitter-to-Collector Breakdown Voltage 5V
- * Operating Temperature Range -50°C to +100°C
- * Storage Temperature Range -50°C to +100°C
- * Lead Soldering Temperature (1.6 mm from body for 5 sec) 240°C
- * Relative Humidity at 85°C 85%
- * Power Dissipation at (or below) 25°C Free Air Temperature 100 mW

ELECTRICAL AND RADIANT CHARACTERISTICS ($T_A = 25^\circ\text{C}$)

Symbol	Parameter	Min	Typ	Max	Unit	Test Condition
V_{CE0}	Collector-Emitter Breakdown Voltage	30			V	$I_C = 10\mu\text{A}$ $E = 0$
V_{VE0}	Emitter-Collector Breakdown Voltage	5			V	$I_C = 10\mu\text{A}$ $E = 0$
$V_{CE(SAT)}$	Collector-Emitter Saturation Voltage		0.4		V	$I_C = 0.5\text{mA}$ $E = 20\text{mW/cm}^2$
I_D	Dark Current			100	nA	$V_{CE} = 15\text{V}$ $E = 0$
I_L	Photo Current Tungsten Source at Colour Temperature of 2854°K	1.0	20		mA	$V_{CE} = 5\text{V}$ $E = 20\text{mW/cm}^2$
t_r	Rise Time (10% to 80%)		5		μs	$V_{CE} = 30\text{V}$ $I_L = 800\mu\text{A}$
t_f	Fall Time (80% to 10%)		5		μs	$R_L = 1\text{Kohm}$

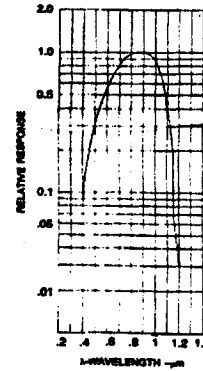


Fig. B.II-1, Reference information for photo transistors used in time of arrival velocity gauges.

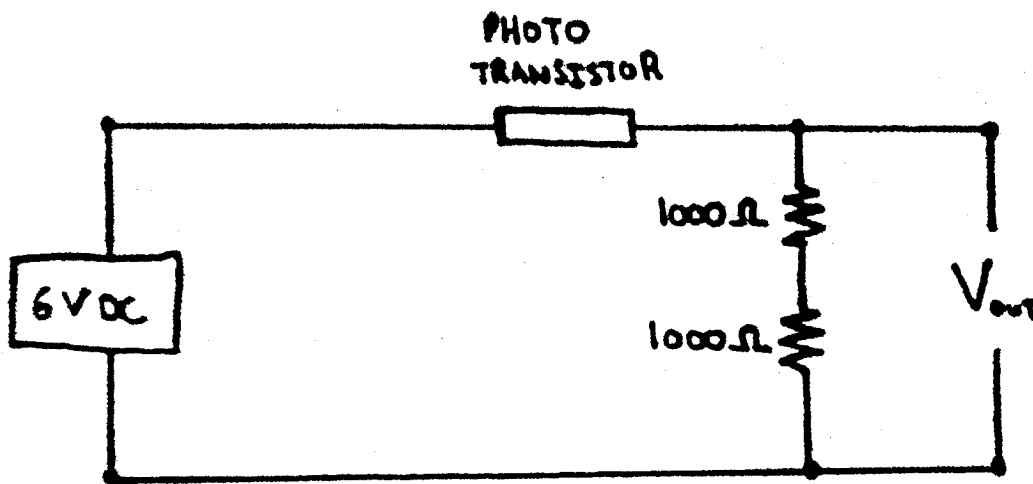


Fig. B.II-2, Simplified electronics diagram implemented for time of arrival velocity gauges.